# EVEN-PARITY $S_N$ ADJOINT METHOD INCLUDING $SP_N$ MODEL ERROR AND ITERATIVE EFFICIENCY

A Dissertation

by

YUNHUANG ZHANG

Submitted to the Office of Graduate and Professional Studies of
Texas A&M University
in partial fulfillment of the requirements for the degree of

DOCTOR OF PHILOSOPHY

| | |
|---|---|
| Chair of Committee, | Jim E. Morel |
| Co-Chair of Committee, | Jean C. Ragusa |
| Committee Members, | Ryan G. McClarren |
| | Wolfgang Bangerth |
| Head of Department, | Yassin A. Hassan |

August 2014

Major Subject: Nuclear Engineering

# ABSTRACT

In this Dissertation, we analyze an adjoint-based approach for assessing the model error of $SP_N$ equations (low fidelity model) by comparing it against $S_N$ equations (high fidelity model). Three model error estimation methods, namely, *direct* , *residual* , and *adjoint* methods are proposed. In order to compare the $SP_N$ solution against $S_N$, we also proposed angular intensity reconstruction schemes for reconstructing $S_N$ angular intensity from $SP_N$ solutions. The methodology is then applied to a vehicle atmosphere re-entry problem and the convergence behavior of the $SP_N$ and Even-parity $S_N$ are compared with that of the Least-squares $S_N$ method. The results show that all the three model error estimation methods are equivalent up to a readily computable compensation and the Least-squares $S_N$ method is far superior than the Even-parity $S_N$ and $SP_N$ methods when applied to such a near-void problem. Various forms of $SP_N$ equations, together with their appropriate iterative solution schemes and acceleration techniques are evaluated in terms of iterative efficiency. The Fourier analyses and numerical test results indicate the Canonical form solved with DSA or AnMG preconditioned source iteration offering the best iterative performance.

To my family.

# ACKNOWLEDGEMENTS

I would like to express my sincere gratitude to my advisor and committee chair, Dr. Jim E. Morel, for his guidance and generous support throughout my dissertation research. I could not have overcome all those difficulties without his help. His genuine expertise and patience is greatly appreciated. I also would like to offer my special thanks to my committee co-chair, Dr. Jean C. Ragusa, who served as my advisor since I started my graduate study here at Texas A&M University, led me into the graduate research, and provided technical support in all aspect besides the research advice. I am also grateful to my other committee members, Dr. Wolfgang Bangerth for providing invaluable support in deal.II as well as suggestions to solidify this dissertation and Dr. Ryan G. McClarren for bringing out questions which stimulated me to broaden my mind and knowledge.

My special thanks are extended to our partners at University of Texas at Austin, especially Dr. Paul T. Bauman, with whom we had numerous discussions and who provided data vital to my research. I also would like to thank former graduate students from our research group, Dr. Bruno Turksin, Dr. Matt R. Sternat, Dr. Zeyun Wu, and Dr. Valentin N. Zingan, whom I learnt a lot from and also had fun with.

Last but not least, I am deeply grateful to my family, my parents and my wife, for her understanding and support through my academic endeavor.

# NOMENCLATURE

Abbreviations

| | |
|---|---|
| AnMG | Angular Multi-grid |
| DSA | Diffusion Synthetic Acceleration |
| FEM | Finite Element method |
| F.P. | Fokker-Planck scattering |
| I.B.P | integration by parts |
| ISO | isotropic scattering |
| $P_1$SA | $P_1$ Synthetic Acceleration |

Symbols

| | |
|---|---|
| $a$ | radiation constant |
| $b$ | Finite Element basis function |
| $B$ | Planck function |
| $c$ | scattering ratio |
| $c_0$ | speed of light |
| $C_v$ | heat capacity |
| $D^{\pm}$ | discrete-to-moment matrix |
| $E$ | radiation enenrgy |
| $\vec{\mathcal{F}}, \vec{J}$ | radiation flux |
| $g$ | boundary condition function |
| $k$ | thermal conductivity |
| $\vec{k}$ | reference direction for angular intensity reconstruction |
| $K$ | number of vertices |
| $\mathbf{L}$ | transport operator |

| | |
|---|---|
| $m$ | direction index |
| $M_{dir}$ | total number of quadrature directions |
| $M^{\pm}$ | moment-to-discrete matrix |
| $\vec{n}$ | boundary normal vector |
| $P$ | phase space |
| $Q$ | total effective source |
| $QoI$ | quantity of interest |
| $r$ | response function |
| $\mathcal{R}$ | residual |
| $S$ | inhomogeneous source |
| $t$ | time |
| $T$ | material temperature |
| $\mathcal{T}_0$ | diffusion operator |
| $\underline{\boldsymbol{x}}$ | spatial position |
| $v$ | particle speed |
| $V$ | volume |
| $\Gamma$ | boundary correction term |
| $\delta QoI$ | error in $QoI$ |
| $\delta\delta QoI$ | difference in $\delta QoI$'s computed by different methods |
| $\epsilon$ | asymptotic scaling factor |
| $\zeta$ | renormalization factor |
| $\digamma$ | composite intensity |
| $\eta$ | iterative efficiency |
| $\lambda$ | Fourier frequency |
| $\mu$ | polar angle cosine |
| $\xi$ | azimuthal angle |

| | |
|---|---|
| $\rho$ | spectral radius |
| $\sigma_a$ | absoprtion cross-section |
| $\sigma_s$ | scattering cross-section |
| $\sigma_t$ | total cross-section |
| $\phi$ | angle-integrated intensity |
| $\psi$ | particle angular intensity |
| $w_m$ | $m$-th quadrature weight |
| $\Omega$ | particle traveling angle |
| $\partial V$ | boundary |
| $< \cdot, \cdot >$ | inner product |
| Superscripts | |
| $\ell$ | iteration index |
| $^+$ | denotes even-parity operators or quantities |
| $^*$ | denotes adjoint operators or quantities |
| $^\dagger$ | compensated error estimation |
| $\tilde{}$ | denotes Finite Element approximation quantities |
| Subscripts | |
| $SP_N \rightarrow S_{N'}$ | indicates $S'_n$ quantities reconstructed from $SP_n$ solution |

TABLE OF CONTENTS

LIST OF FIGURES

FIGURE Page

# LIST OF TABLES

TABLE Page

# 1. INTRODUCTION

The Simplified $P_N$ ($SP_N$) approximation is commonly used to model radiation transport problems. Although the discretization error of the $SP_N$ equations has been well studied, the model error associated with this set of equations has received less attention. In this Dissertation, we develop a framework to quantify the model error associated with the $SP_N$ equations by comparing it with the $S_N$ equations, the latter being a high-fidelity transport model that converges to the true transport solution as $N$ increases.

## 1.1 Model Error and Predictive Science

Predictive science is the application of verified and validated computational simulations to predict the behavior of complex systems where routine experiments are not feasible. In order to make precise statements about the degree of confidence in the simulation-based predictions, the error and uncertainty associated with a simulation need to be quantified. Part of the simulation error is the model error, which is due to the incompleteness of the mathematical model in capturing the physics that it tries to describe. Unlike the discretization error, which can be reduced as one refines the mesh, the model error is inherent to the modeling equations.

## 1.2 Transport Equation and Approximation Models: $S_N$ vs. $SP_N$

Radiation transport for neutral particles is characterized by the time-dependent, energy-dependent, angle-dependent, and space-dependent Boltzmann transport equa-

tion:

$$\frac{1}{v}\frac{\partial\psi}{\partial t}+\vec{\Omega}\cdot\vec{\nabla}\psi+\sigma_t\psi=\int_0^\infty\int_{4\pi}\sigma_s\left(\underline{\boldsymbol{x}},\vec{\Omega}'\to\vec{\Omega},E'\to E\right)\psi(\underline{\boldsymbol{x}},\vec{\Omega}',E',t)d\Omega' dE'+S, \tag{1.1}$$

where

$$\begin{aligned}
v &= \text{particle speed, } [cm/s]\\
\underline{\boldsymbol{x}},\vec{\Omega},E,t &= \text{spatial position, angle}[steradian], \text{ energy}[keV], \text{ time}[s]\\
\psi(\underline{\boldsymbol{x}},\vec{\Omega},E,t) &= \text{particle angular flux, } [particles/cm^2-steradian-keV-s]\\
\sigma_t &= \text{total macroscopic cross-section, } [1/cm]\\
\sigma_s &= \text{scattering macroscopic cross-section, } [1/cm-steradian-keV]\\
S &= \text{inhomogeneous source, } [particles/cm^3-steradian-keV-s]
\end{aligned}$$

The radiation transport equations is a particle balance equation built upon a six dimensional phase space, 3 for spatial position, 2 for angle, and 1 for energy. Solving the radiation transport equation is still challenging even with today's peta-scale computers, due to its high phase space dimensions. Back in the 1960s, when trying to solve the transport equation with limited computational resources, Ely Gelbard[4, 5, 6] developed the Simplified $P_N$ ($SP_N$) method as an inexpensive alternative to the $P_N$(spherical-harmonic) and $S_N$ (discrete ordinates) methods. $P_N$ and $S_N$ methods are well established methods that converge to the transport solution as the order $N$ increases. However, as $N$ increases, the number of unknowns increases at a rate of $O(N^2)$. On the other hand, this number for the $SP_N$ equations only increases as $(N+1)/2$, which is very attractive in terms of both computational cost and memory cost. Despite the relatively heuristic original derivation by Gelbard, and significant

reduction of the number of unknowns, the $SP_N$ equations are shown and proven to be a surprisingly good approximation when the problem is very diffusive and scattering dominant[10], or when the solution is locally 1-D[17]. Furthermore, in 1-D slab geometry the $SP_N$ equations are always equivalent to the $S_{N+1}$ equations (with Gauss quadrature) and the $P_N$ equations. In this research, the canonical form [10, 16] of the $SP_N$ equations are used as the low-fidelity model for the radiation transport problem. By comparing it to the high-fidelity model, the even-parity form of the $S_N$ equations, we will quantify the model error associated with the $SP_N$ method. The reason for choosing those specific forms of the two methods will be discussed later.

## 1.3 The PECOS Project

The Predictive Engineering and Computational Sciences Center (PECOS) at the University of Texas is one of the five Centers of Excellence sponsored under PSAAP. The goal of the PECOS Center is to develop the next generation of advanced computational methods for predictive simulation of multiscale, multiphysics phenomena, and to apply these methods to the analysis of space reentry problems. Texas A&M University is collaborating with the PECOS center to quantify one component of the uncertainty in the numerical simulation associated with the ablation process of the heat-shield on a space vehicle during its reentry into the earth atmosphere. One of the physical processes associated with the ablation process corresponds to a radiative transfer problem in which stagnation of the airflow as it strikes the ablator leads to the formation of a shock. The shock emits black-body radiation that deposits photon energy in the ablator. This is a strongly non-linear problem, with material properties depending on the temperature. Figure. 1.1 gives an overview of this problem.

This process can be modeled as a coupled radiation transport and material energy problem. For simplicity, the hydrodynamic equations are not presented, since the

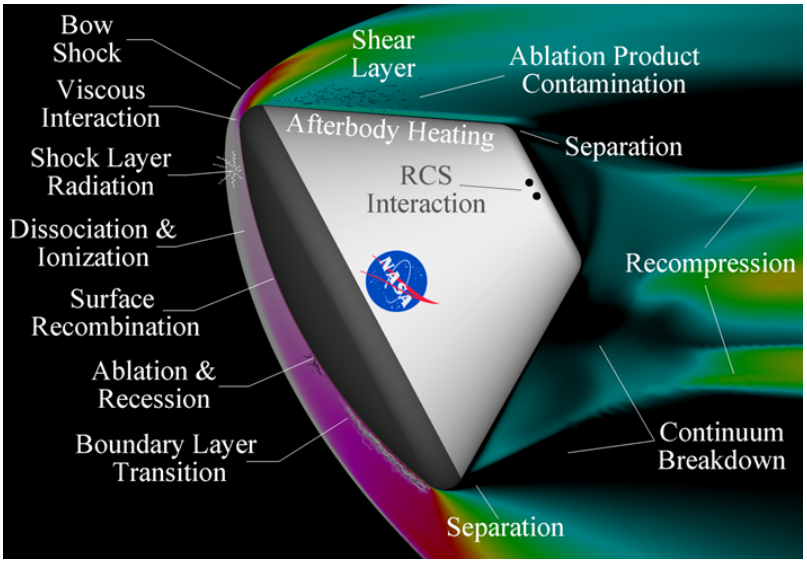


Figure 1.1: PECOS space vehicle reentry problem (Simmons, ICES Forum [18])

focus of our work deals with radiation modeling. The equations governing the physics are given below:

Radiation transport equation:

$$\frac{\partial \psi}{c_0 \partial t} + \vec{\Omega} \cdot \vec{\nabla} \psi + \sigma_t(T)\psi = \int_{4\pi} \sigma_s(\underline{\boldsymbol{x}}, T, \vec{\Omega}' \cdot \vec{\Omega}, E)\psi(\vec{\Omega}', E)d\Omega' + \sigma_a B(T, E). \quad (1.2)$$

Material energy balance equation:

$$C_{\mathrm{v}}(T)\frac{\partial T}{\partial t} - \vec{\nabla} \cdot k(T)\vec{\nabla} T = \int_0^\infty \sigma_a(T) \left[ \int_{4\pi} \psi(\vec{\Omega}', E)d\Omega' - 4\pi B(T, E) \right] dE. \quad (1.3)$$

where

$$
\begin{aligned}
c_0 &= \text{speed of light, } [cm/s] \\
\psi(\underline{\boldsymbol{x}}, \vec{\Omega}, E, t) &= \text{angular energy intensity, } [keV/cm^2 - steradian - keV - s] \\
\sigma_t, \sigma_a, \sigma_s &= \text{total and absorption cross-section, } [1/cm] \\
\sigma_s &= \text{scattering cross-section, } [1/cm - steradian - keV] \\
T(\underline{\boldsymbol{x}}, t) &= \text{material temperature [degrees } K] \\
E &= \text{radiation energy, } [keV] \\
B &= \text{Planck function, } [keV/cm^2 - steradian - s] \\
C_{\mathrm{v}} &= \text{heat capacity } [keV/K - cm^3] \\
k &= \text{thermal conductivity } [keV/cm - K - s]
\end{aligned}
$$

Note that for Eq. (1.2) we used the radiative transfer form of the Boltzmann equation, in which we replace $v$ with $c_0$, redefine $\psi$ as radiative angular intensity, add temperature dependence for all the cross sections, drop the energy dependence of the scattering cross-section because of the monochromatic scattering, and finally replace the general inhomogeneous source term with a black-body radiation source characterized by the Planck function.

This Dissertation is only focused on the radiation transport equation (Eq. (1.2)). Solving it can be seen as one iteration in a multi-physics solution process. In any given iteration, the transport equation is linearized by assuming a known temperature distribution obtained with a fully coupled fluid flow and gray diffusion calculation. Considering that the speed of light is of such a large magnitude than the transient of the radiation equation is much faster than the transient of the material energy equation, we also reduce the problem to a steady state one. Furthermore, since

there is no inter-group coupling, the energy dependent multi-group equations can be treated as a set of independent single-group equations. For the PECOS problem, we consider the steady-state single-group (grey) radiation transport equation with isotropic scattering:

$$\vec{\Omega} \cdot \vec{\nabla}\psi + \sigma_t(\underline{\boldsymbol{x}}, T)\psi = \frac{\sigma_s(\underline{\boldsymbol{x}}, T)}{4\pi}\phi + \sigma_a(\underline{\boldsymbol{x}}, T)\frac{ac_0T^4}{4\pi}, \tag{1.4}$$

where $a$ is radiative constant $[keV/K^4 - cm^3]$, $T$ is assumed given, and $\phi(x) = \int_{4\pi} \psi(\underline{\boldsymbol{x}}, \vec{\Omega})$.

However, we consider more general forms of the Boltzmann equation when discussing other topics in this dissertation.

## 2. HIGHER-RESOLUTION RADIATION TRANSPORT MODEL: $S_N$

In this section, we consider a general form of the Boltzmann transport equation with anisotropic scattering and anisotropic source:

$$\vec{\Omega} \cdot \vec{\nabla}\psi(\vec{\Omega}) + \sigma_t \psi(\vec{\Omega}) = \mathcal{K}\psi + S(\vec{\Omega}) \equiv Q(\vec{\Omega}), \tag{2.1}$$

where

$$\mathcal{K}\psi = \sum_{l=0}^{\infty} \sum_{q=-l}^{l} \frac{2l+1}{4\pi} \sigma_{s,l} \phi_l^q Y_l^q(\vec{\Omega}). \tag{2.2}$$

Notice that we expanded the scattering term in spherical harmonics ($Y_l^q$'s). The Legendre moments of the scattering cross section ($\sigma_{s,l}$'s) are defined as follows:

$$\sigma_{s,l} = 2\pi \int_{-1}^{1} \sigma_s(\xi_s) P_l(\xi_s) d\xi_s, \qquad l = 1, \cdots, \infty, \tag{2.3}$$

where

$$\xi_s = \vec{\Omega}' \cdot \vec{\Omega}, \tag{2.4}$$

$$P_l = \text{Legendre moment of } l\text{-th order.} \tag{2.5}$$

The angular flux moments ($\phi_l^q$'s) are defined as follows:

$$\phi_l^m = \int_{4\pi} \psi(\vec{\Omega}) Y_l^q(\vec{\Omega}) d\Omega, \tag{2.6}$$

with the zero-th moment, commonly denoted by $\phi$, being the angular integrated intensity and the first moment, commonly denoted by $\vec{\mathcal{F}}$, being the radiation flux.

The $S_N$ method, also known as the *Discrete Ordinate* method, discretizes the

angular dependency of the transport equation over a set of discrete directions. The directions ($\Omega_m$) together with their associated weights ($w_m$) are usually given by an angular quadrature set, $(\Omega_m, w_m)$, where $m$ is the quadrature (direction) index. The $N$ subscript in the quadrature name indicates the order of the quadrature sets that are being used, hence reflects the angular resolution.

In this Dissertation, we used the triangular Chebyshev-Legendre (G-L) angular quadratures set. As illustrated in Fig. 2.1 (showing $S_6$), we used Gauss-Legendre quadratures ($\mu$'s) to define the $z$-levels and Gauss-Chebyshev quadratures ($\xi$'s) to define the point locations on each $z$-level. $N$ defines the number of $z$-levels and the total number of quadrature points is equal to $M_{dir} = N(N+2)$. For detail about the G-L quadrature set we refer the readers to [21]. The $S_N$ method is a well established method for radiation transport calculation, and it is proven to converge to the true transport solution as $N$ increases. Therefore, we choose the $S_N$ equations as our higher-resolution model.

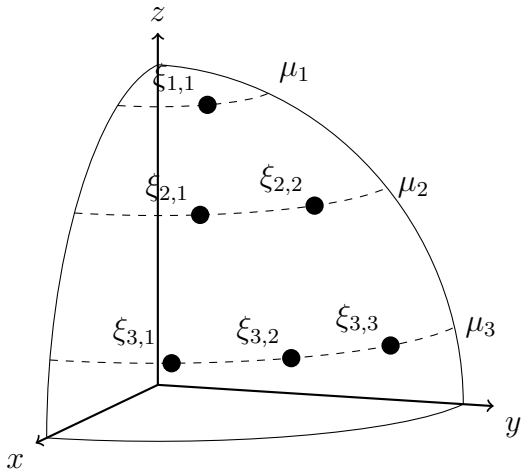


Figure 2.1: Gauss-Chebyshev quadrature set for a single octant (showing $S_6$). [The quadrature sets are invariant under 90°rotations.]

Equation (2.1) gives the first order form of the transport equations. In this Dissertation, however, we focus on second order forms of the transport equation, namely, the *Even-parity* $S_N$ equation and the Least-squares $S_N$ equation. We will discuss them in detail in the rest of this section.

## 2.1 Even-parity $S_N$

### *2.1.1 Even-parity Transport Formalism*

The first step towards the derivation of even-parity form is to define the even- and odd-parity angular intensities:

$$\psi^+(\vec{\Omega}) = \frac{\psi(\vec{\Omega}) + \psi(-\vec{\Omega})}{2}, \tag{2.7}$$

$$\psi^-(\vec{\Omega}) = \frac{\psi(\vec{\Omega}) - \psi(-\vec{\Omega})}{2}, \tag{2.8}$$

and similarly for the total source terms:

$$Q^+(\vec{\Omega}) = \frac{Q(\vec{\Omega}) + Q(-\vec{\Omega})}{2} = \mathcal{K}^+\psi^+ + S^+, \tag{2.9}$$

$$Q^-(\vec{\Omega}) = \frac{Q(\vec{\Omega}) - Q(-\vec{\Omega})}{2} = \mathcal{K}^-\psi^- + S^-. \tag{2.10}$$

Replacing the $\vec{\Omega}$ with $-\vec{\Omega}$ in Eq. (2.1), we obtain:

$$-\vec{\Omega}\cdot\vec{\nabla}\psi(-\vec{\Omega}) + \sigma_t\psi(-\vec{\Omega}) = Q(-\vec{\Omega}); \tag{2.11}$$

Adding Eq. (2.1) and Eq. (2.11), we obtain:

$$\vec{\Omega}\cdot\vec{\nabla}\psi^- + \sigma_t\psi^+ = Q^+; \tag{2.12}$$

Subtracting Eq. (2.11) from Eq. (2.1), we obtain:

$$\vec{\Omega} \cdot \vec{\nabla}\psi^+ + \sigma_t \psi^- = Q^-; \tag{2.13}$$

In the Full-Elimination version of the even-parity equations, the scattering terms are moved to the left hand side and then the $\psi^-$ is solved for in terms of $\psi^+$ and $S^-$ using Eq. (2.13):

$$\psi^- = -(\sigma_t - \mathcal{K}^-)^{-1}\vec{\Omega} \cdot \vec{\nabla}\psi^+ + (\sigma_t - \mathcal{K}^-)^{-1}S^-, \tag{2.14}$$

Eliminating $\psi^-$ from Eq. (2.12), the Full-Elimination form is obtained as follows:

$$-\vec{\Omega} \cdot \vec{\nabla}(\sigma_t - \mathcal{K}^-)^{-1}\vec{\Omega} \cdot \vec{\nabla}\psi^+ + (\sigma_t - \mathcal{K}^+)\psi^+ = S^+ - \vec{\Omega} \cdot \vec{\nabla}(\sigma_t - \mathcal{K}^-)^{-1}S^-. \tag{2.15}$$

Another traditionally used form that is compatible with source iteration is obtained by leaving the scattering terms in the right hand side. We first solve Eq. (2.13) for $\psi^-$ :

$$\psi^- = -\frac{\vec{\Omega}}{\sigma_t} \cdot \vec{\nabla}\psi^+ + \frac{Q^-}{\sigma_t}, \tag{2.16}$$

and then eliminate $\psi^-$ from Eq. (2.12) as follows:

$$-\vec{\Omega} \cdot \vec{\nabla}\frac{1}{\sigma_t}\vec{\Omega} \cdot \vec{\nabla}\psi^+ + \sigma_t\psi^+ = Q^+ - \vec{\Omega} \cdot \vec{\nabla}\frac{Q^-}{\sigma_t}. \tag{2.17}$$

Equation (2.16) and Eq. (2.17) need to be solved iteratively because the right hand sides contains $\psi^-$ through $Q^-$. However, upon convergence, they produce the same result as given by the Full-Elimination form. We choose the Eq. (2.16) and Eq. (2.17) as the basis for our $S_N$ method because they are easier to solve.

For both the traditional and Full-Elimination even-parity equations, we used

Mark type boundary conditions for source/vacuum conditions. The reflective boundary condition is complex to implement for Even-parity $S_N$ but is theoretically feasible, the reader is referred to [14] for further details. The Mark boundary conditions specify the intensity ($g$) along the incoming direction:

$$\psi(\vec{\Omega}) = \psi^+ + \psi^- = g(\vec{\Omega}) = g, \qquad \text{for } \vec{\Omega} \cdot \vec{n} < 0, \tag{2.18}$$

where $\vec{n}$ is the normal direction on the boundary surface. Alternatively, in terms of out-going direction, we replace $\vec{\Omega}$ with $-\vec{\Omega}$ and the boundary condition becomes:

$$\psi(-\vec{\Omega}) = \psi^+ - \psi^- = g(-\vec{\Omega}) = g, \qquad \text{for } \vec{\Omega} \cdot \vec{n} > 0. \tag{2.19}$$

### *2.1.2 Even-parity $S_N$ Discretization*

The $S_N$ form of Eq. (2.17) and Eq. (2.16) can be written as follows:

$$-\vec{\Omega}_m \cdot \vec{\nabla} \frac{1}{\sigma_t} \vec{\Omega}_m \cdot \vec{\nabla} \psi_m^+ + \sigma_t \psi_m^+ = Q_m^+ - \vec{\Omega}_m \cdot \vec{\nabla} \frac{Q_m^-}{\sigma_t}, \quad m = 1, \cdots, \frac{N(N+2)}{2}, \tag{2.20}$$

$$\psi_m^- = -\frac{\vec{\Omega}_m}{\sigma_t} \cdot \vec{\nabla} \psi_m^+ + \frac{1}{\sigma_t} Q_m^-, \quad m = 1, \cdots, \frac{N(N+2)}{2}. \tag{2.21}$$

where $\psi_m^\pm \equiv \psi^\pm(\vec{\Omega}_m)$, $S_m^\pm \equiv S^\pm(\vec{\Omega}_m)$, and $Q_m^\pm \equiv Q^\pm(\vec{\Omega}_m)$. Note that because the Gauss-Chebyshev quadrature is symmetric with respect to the origin and $\psi^+(\vec{\Omega}_m) = \psi^+(-\vec{\Omega}_m)$, we are able to reduce our direction set by half.

The $S_N$ discretized boundary condition needs a special treatment to insure the incoming flux is preserved. This is because the numerical integration over the half-range is not necessarily exact. To account for this error, we use a renormalized $g'_m$ defined as follows:

$$g'_m = g_m \frac{\int_{\vec{\Omega} \cdot \vec{n} < 0} g(\vec{\Omega}) |\vec{\Omega} \cdot \vec{n}| d\Omega}{\sum_{m | \vec{\Omega}_m \cdot \vec{n} < 0} g_m |\vec{\Omega}_m \cdot \vec{n}| w_m}, \tag{2.22}$$

where $g_m = g(\vec{\Omega}_m)$ and the numerator is the half-range flux computed analytically. Finally the $S_N$ boundary condition can be written as follows:

$$\psi(\vec{\Omega}_m) = \psi_m^+ + \psi_m^- = g'_m, \qquad \text{for } \vec{\Omega}_m \cdot \vec{n} < 0, \tag{2.23}$$

$$\psi(-\vec{\Omega}_m) = \psi_m^+ - \psi_m^- = g'_m, \qquad \text{for } \vec{\Omega}_m \cdot \vec{n} > 0. \tag{2.24}$$

Some properties of such a $S_N$ form include:

1. The left-hand-side (LHS) of the second-order Eq. (2.20) has structure similar to a diffusion equation, thus can be solved using similar spatial disretization techniques.

2. The odd-parity component can be obtained from Eq. (2.21) as a post-processing step after $\psi_m^+$ has been solved for from Eq. (2.20). Therefore, we regard $\psi_m^+$ as the primary unknown, while $\psi_m^-$ is an auxiliary unknown.

3. The number of primary unknowns has been reduced by half compared to the first-order $S_N$ equations, by taking advantage of the symmetry of the even-parity flux and Gauss-Chebyshev quadrature set.

4. Because of the diffusion-like second order Laplacian operators in the streaming terms, the numerical solution at a given point can be affected by both its up-wind and down-wind neighbours. This is not consistent with the particle transport physics that information can only propagate along the direction that a particle travels. We will discuss this later when this inconsistency causes issues.

5. Because of the presence of an inverse of the opacity ($\sigma_t$) in the Laplacian terms, the system matrix becomes ill-conditioned when in near-void. We will

talk about a remedy later on.

### *2.1.3 Adjoint Even-parity $S_N$ Formalism*

The goal of this dissertation is to develop an adjoint approach to estimate the model error, particularly, the error in some quantity of interests ($QoI$). In the forward method, the $QoI$ is computed as:

$$QoI = \langle \psi, r \rangle \,, \tag{2.25}$$

where $r$ is the response function characterizing the $QoI$, and $\langle \cdot, \cdot \rangle$ is an inner product defined over phase space $(\underline{\boldsymbol{x}}, \underline{\Omega})$. For instance, the inner product between two arbitrary function $p$ and $q$ is:

$$\langle p, q \rangle = \int_{4\pi} \int_{V} p \; q \; dV d\Omega. \tag{2.26}$$

In the adjoint approach, we first solve the corresponding adjoint transport equation with $r$ as the source. After obtaining the adjoint solution, $\psi^*$, the $QoI$ can be computed by taking the inner product between $\psi^*$ and the forward distributed source $S$ as follows:

$$QoI = \langle \psi^*, S \rangle \tag{2.27}$$

The advantage of the adjoint approach is that once the $\psi^*$ has been solved for, it can be used to compute the $QoI$ in various source conditions and no more transport solve is needed. However, if the adjoint transport equation is not a perfect adjoint to the forward equation, which is the case for our application, a concomitant ($\Gamma \equiv \langle \psi, r \rangle - \langle \psi^*, S \rangle$) needs to be computed for.

For PECOS application, we are only concerned with even-parity responses. It

can be shown that under the inner product defined in Eq. (2.26), the adjoint Full-Elimination even-parity equation is:

$$-\vec{\Omega}\cdot\vec{\nabla}(\sigma_t-\mathcal{K}^-)^{-1}\vec{\Omega}\cdot\vec{\nabla}\psi^{+,*}+(\sigma_t-\mathcal{K}^+)\psi^{+,*}=r^+ \tag{2.28}$$

The adjoint traditional even-parity equations are:

$$-\vec{\Omega}\cdot\vec{\nabla}\frac{1}{\sigma_t}\vec{\Omega}\cdot\vec{\nabla}\psi^{+,*}+\sigma_t\psi^{+,*}=\mathcal{K}^+\psi^{+,*}+r^+-\vec{\Omega}\cdot\vec{\nabla}\frac{\mathcal{K}^-\psi^{-,*}}{\sigma_t}, \tag{2.29}$$

$$\psi^{-,*}=-\frac{\vec{\Omega}}{\sigma_t}\cdot\vec{\nabla}\psi^{+,*}+\frac{\mathcal{K}^-\psi^{-,*}}{\sigma_t}. \tag{2.30}$$

The adjoint boundary condition is defined for out-going directions, in a manner similar to its forward counterpart. We use vacuum boundary conditions for where the forward problem has source boundary conditions, in order to simplify the adjoint analyses. As stated before, we are not considering the reflective boundary conditions here. Therefore, the adjoint boundary conditions are:

$$\psi^*(\vec{\Omega}_m)=\psi_m^{+,*}+\psi_m^{-,*}=g_m^*=0, \qquad \text{for } \vec{\Omega}_m\cdot\vec{n}>0, \tag{2.31}$$

$$\psi^*(-\vec{\Omega}_m)=\psi_m^{+,*}-\psi_m^{-,*}=g_m^*=0, \qquad \text{for } \vec{\Omega}_m\cdot\vec{n}<0. \tag{2.32}$$

We know that the removal and scattering operators are self-adjoint, the concomitant $\Gamma$ can be obtained by comparing the streaming terms. For simplicity, we use

the Full-Elimination form to derive the expression for $\Gamma$ as follows:

$$
\begin{aligned}
\Gamma &= \left\langle \psi^{+}, r^{+} \right\rangle - \left\langle \psi^{+,*}, \underbrace{S^{+} - \vec{\Omega}\cdot\vec{\nabla}(\sigma_t - \mathcal{K}^{-})^{-1} S^{-}}_{\text{R.H.S of Eq. (2.15)}} \right\rangle \\
&= \left\langle \psi^{+}, -\vec{\Omega}\cdot\vec{\nabla}(\sigma_t - \mathcal{K}^{-})^{-1}\vec{\Omega}\cdot\vec{\nabla}\psi^{+,*} \right\rangle - \left\langle \psi^{+,*}, -\vec{\Omega}\cdot\vec{\nabla}(\sigma_t - \mathcal{K}^{-})^{-1}\vec{\Omega}\cdot\vec{\nabla}\psi^{+} \right\rangle \\
&= -\int_{4\pi}\oint \psi^{+}(\sigma_t - \mathcal{K}^{-})^{-1}\vec{\Omega}\cdot\vec{\nabla}\psi^{+,*}\vec{\Omega}\cdot\vec{n}dAd\Omega \\
&\quad + \int_{4\pi}\oint \psi^{+,*}(\sigma_t - \mathcal{K}^{-})^{-1}\vec{\Omega}\cdot\vec{\nabla}\psi^{+}\vec{\Omega}\cdot\vec{n}dAd\Omega \\
&= -\int_{4\pi}\oint \psi^{+}\psi^{-,*}\vec{\Omega}\cdot\vec{n}dAd\Omega - \int_{4\pi}\oint \psi^{+,*}\psi^{-}\vec{\Omega}\cdot\vec{n}dAd\Omega \\
&\quad + \int_{4\pi}\oint \psi^{+,*}(\sigma_t - \mathcal{K}^{-})^{-1}S^{-}\vec{\Omega}\cdot\vec{n}dAd\Omega \\
&= -\int_{\vec{\Omega}\cdot\vec{n}<0}\oint \psi^{+}\psi^{-,*}\vec{\Omega}\cdot\vec{n}dAd\Omega - \int_{\vec{\Omega}\cdot\vec{n}<0}\oint \psi^{+,*}\psi^{-}\vec{\Omega}\cdot\vec{n}dAd\Omega \\
&\quad - \int_{\vec{\Omega}\cdot\vec{n}>0}\oint \psi^{+}\psi^{-,*}\vec{\Omega}\cdot\vec{n}dAd\Omega - \int_{\vec{\Omega}\cdot\vec{n}>0}\oint \psi^{+,*}\psi^{-}\vec{\Omega}\cdot\vec{n}dAd\Omega \\
&\quad + \int_{4\pi}\oint \psi^{+,*}(\sigma_t - \mathcal{K}^{-})^{-1}S^{-}\vec{\Omega}\cdot\vec{n}dAd\Omega \\
&= -\int_{\vec{\Omega}\cdot\vec{n}<0}\oint \psi^{+}\psi^{+,*}\vec{\Omega}\cdot\vec{n}dAd\Omega - \int_{\vec{\Omega}\cdot\vec{n}<0}\oint \psi^{+,*}[g(\vec{\Omega}) - \psi^{+}]\vec{\Omega}\cdot\vec{n}dAd\Omega \\
&\quad - \int_{\vec{\Omega}\cdot\vec{n}>0}\oint \psi^{+}(-\psi^{+,*})\vec{\Omega}\cdot\vec{n}dAd\Omega - \int_{\vec{\Omega}\cdot\vec{n}>0}\oint \psi^{+,*}[\psi^{+} - g(-\vec{\Omega})]\vec{\Omega}\cdot\vec{n}dAd\Omega \\
&\quad + \int_{4\pi}\oint \psi^{+,*}(\sigma_t - \mathcal{K}^{-})^{-1}S^{-}\vec{\Omega}\cdot\vec{n}dAd\Omega \\
&= -\int_{\vec{\Omega}\cdot\vec{n}<0}\oint 2\psi^{+,*}g(\vec{\Omega})\vec{\Omega}\cdot\vec{n}dAd\Omega + \int_{4\pi}\oint \psi^{+,*}(\sigma_t - \mathcal{K}^{-})^{-1}S^{-}\vec{\Omega}\cdot\vec{n}dAd\Omega
\end{aligned}
\tag{2.33}
$$

For the PECOS problem, the source is isotropic and scattering is unimportant. In the absence of anisotropic source and scattering, Eq. (2.33) reduces to:

$$
\Gamma = -\int_{\vec{\Omega}\cdot\vec{n}<0}\oint 2\psi^{+,*}g(\vec{\Omega})\vec{\Omega}\cdot\vec{n}dAd\Omega \tag{2.34}
$$

which can also be obtained by applying the analogous analyses to the traditional form of the even-parity equations, with the same assumption. In practice, we work with the $S_N$ form of the latter, because it is compatible with source iteration and much easier to solve than the Full-Elimination form. Another point to make is that although the more general expression with no assumption on source or scattering condition, Eq. (2.33), is obtained through the analyses of the Full-Elimination form, it also applies to the traditional form upon convergence, because these two forms are mathematically equivalent.

## 2.2 Self-adjoint Least-squares $S_N$

Another second-order self-adjoint form of $S_N$ equations that we investigated is the Least-squares $S_N$ equations proposed by Hansen and Morel [8]. This form differs from the standard least-squares transport equations in that it is compatible with source iteration, thus all the acceleration techniques, such as Diffusion-Synthetic-Acceleration (DSA) that applies to standard source iteration, can be applied to the Least-squares $S_N$ equations with the same effect.

### *2.2.1 Least-squares Transport Formalism*

We begin the derivation of the Least-squares $S_N$ equations by first re-expressing the first-order $S_N$ equations using removal and scattering operator $\mathbf{L}$ as follows:

$$\mathbf{L}\psi = Q, \tag{2.35}$$

where

$$\mathbf{L} := \vec{\Omega} \cdot \vec{\nabla} + \sigma_t. \tag{2.36}$$

Under the standard inner product, the adjoint of the removal and scattering operator, $\mathbf{L}^*$, is:

$$\mathbf{L}^* := -\vec{\Omega} \cdot \vec{\nabla} + \sigma_t. \tag{2.37}$$

Applying $\mathbf{L}_m^*$ to Eq. (2.35), we obtain a least-squares or "normal" form of the transport equation that we seek:

$$\mathbf{L}^*\mathbf{L}\psi = \mathbf{L}^*Q, \tag{2.38}$$

or more specifically, in 3-D after we expand every term,

$$-\vec{\Omega} \cdot \vec{\nabla}\vec{\Omega} \cdot \vec{\nabla}\psi + \left[\sigma_t \vec{\Omega} \cdot \vec{\nabla}\psi - \vec{\Omega} \cdot \vec{\nabla}(\sigma_t\psi)\right] + \sigma_t^2\psi = -\vec{\Omega} \cdot \vec{\nabla}Q + \sigma_t Q. \tag{2.39}$$

Combining the terms in the square bracket, we get the final expression for the Least-squares $S_N$ equations:

$$-\vec{\Omega} \cdot \vec{\nabla}\vec{\Omega} \cdot \vec{\nabla}\psi - \vec{\Omega}\psi \cdot \vec{\nabla}\sigma_t + \sigma_t^2\psi = -\vec{\Omega} \cdot \vec{\nabla}Q + \sigma_t Q. \tag{2.40}$$

The boundary is treated differently for incoming and outgoing directions. For the incoming direction, the Dirichlet boundary conditions is used:

$$\psi = g, \qquad \vec{\Omega} \cdot \vec{n} \leq 0, \tag{2.41}$$

where $g$ is the incoming angular intensity. For the outgoing directions, the first order transport equation is used to close the system:

$$\vec{\Omega} \cdot \vec{\nabla}\psi = Q - \sigma_t\psi, \qquad \vec{\Omega} \cdot \vec{n} > 0. \tag{2.42}$$

This closure is important when forming the weak form of the Least-squares $S_N$ equation.

### *2.2.2 Least-squares $S_N$ Discretization*

The $S_N$ form of the Least-squares is given as follows:

$$-\vec{\Omega}_m \cdot \vec{\nabla}\vec{\Omega}_m \cdot \vec{\nabla}\psi_m - \vec{\Omega}_m\psi_m \cdot \vec{\nabla}\sigma_t + \sigma_t^2\psi_m = -\vec{\Omega}_m \cdot \vec{\nabla}Q_m + \sigma_t Q_m, \quad m = 1, \ldots, N(N+2). \tag{2.43}$$

with the discretized boundary conditions as follows:

$$\psi_m = g_m, \qquad \vec{\Omega}_m \cdot \vec{n} \leq 0, \tag{2.44}$$

$$\vec{\Omega}_m \cdot \vec{\nabla}\psi_m = Q_m - \sigma_t\psi_m, \qquad \vec{\Omega}_m \cdot \vec{n} > 0. \tag{2.45}$$

Note that for this particular form, the $S_N$ equations need to be solved over the full $4\pi$ directions.

### *2.2.3 Forced Energy Balance*

The Least-squares $S_N$ formulation is a non-conservative form, because when integrated over the spatial domain it does not yield a balance equation, therefore an exact energy balance can not be expected for such a method. However, one can always force an exact balance by scaling the solution in the problem interior and on the boundaries for the incoming directions, that is entire solution vector except where it is dictated by the Dirichlet boundary condition. We call it the non-Dirichlet solution vector. The scaling (also called renormalization) factor is chosen such that the total sink is equal to the total source. To illustrate the process of renormalization, we first

decompose the total sink as follows:

$$Sink_{tot} = Leakage_{Diri} + Leakage_{non-Diri} + Absorption_{Diri} + Absorption_{non-Diri}, \tag{2.46}$$

where $Diri$ indicates components that are determined by the Dirichlet boundary condition, and $non - Diri$ indicates components determined by the non-Dirichlet solution. The renormalization factor is then computed as:

$$\zeta = \frac{Source_{tot} - Leakage_{Diri} - Absorption_{Diri}}{Sink_{tot} - Leakage_{Diri} - Absorption_{Diri}}. \tag{2.47}$$

The key point here is to remove the impact of the Dirichlet boundary condition from the total sink to make the reduced sink solely dependent on the non-Dirichlet solution.

After $\zeta$ has been determined, we scale the non-Dirichlet solution by $\zeta$, thus effectively scale the $Leakage_{non-Diri}$ and $Absorption_{non-Diri}$ by a factor of $\zeta$. This will leave us an exact balance statement:

$$Leakage_{Diri} + Absorption_{Diri} + \zeta(Leakage_{non-Diri} + Absorption_{non-Diri}) = Source_{tot}, \tag{2.48}$$

which is equivalent to Eq. (2.47). In excess of achieving round-off balance, such a renormalization scheme will also help reduce the error in the solution if the original solution exhibits a correct shape while its magnitude is off. As shown in the Appendix A, it is the case for the Least-squares $S_N$ equations applied to our benchmark problems.

## 2.3 $S_N$ Solution Techniques

To solve the $S_N$ transport equation, we also need discretization in space. The $S_N$ equations are already discretized in angle, and we solve them direction by direction by using a standard Source Iteration (SI) method. For the Even-parity $S_N$ equations, the plan is to first solve the second-order equations (Eq. (2.20)) for the primary unknowns, the $\psi^+$'s. And then locally evaluate the first-order equations (Eq. (2.21)) for the secondary unknowns, as a post-process. In the sense of spatial structure, the LHS of the second-order equations are just a set of tensor diffusion equations, therefore we can use continuous Finite Element method (FEM) that is well suited for solving diffusion equations. The first-order equations can be collocated at a set of volumetric quadrature points, and simple algebraic evaluation is all we need to calculate the value of $\psi^-$ at those points. Since we are only considering isotropic scattering in this dissertation, the $\psi^-$ is not of concern. We will skip the discussion on solution of first-order equations and refer the reader to [14]. Similarly, for the Least-squares $S_N$ equations, we also use continuous FEM as the spatial discretization technique, due to its diffusion-like structure.

### *2.3.1 Spatial Discretization*

The Finite Element method (FEM) has been widely used for solving the elliptic systems, such as diffusion equations. The FEM spatially divides the physical domain into a set of cells or *elements*. Each cell is associated with a set of local basis functions, $\left\{b_j^{\text{cell}}(\underline{\boldsymbol{x}})\right\}$, which are also used to represent the spatial dependency of the solution. The basis functions are zero at support points outside its cell and take on the value of unity at at its uniquely associated support point (indexed $j$) within the cell. Local basis functions from different cells sharing the same support point (indexed $i$) are 'glued' together to form the global basis functions, $\{b_i(\underline{\boldsymbol{x}})\}$, with $i = 1 \cdots K$. Their

linear combinations span the space where the finite element solution lives. In this dissertation, we used both first-order and second-order continuous Galerkin finite elements. For example, in 3D cases, the first-order finite element basis functions are tri-linear and continuous across the problem domain. The support points coincide with cell vertices, thus $K$ = number of vertices, which is special to the first-order finite element. The finite element approximation to the general solution function $f$ can be written as:

$$\tilde{f}(\underline{\boldsymbol{x}}) = \sum_{i=1}^{K} \tilde{f}_i b_i(\underline{\boldsymbol{x}}), \tag{2.49}$$

where

$$\tilde{f}_i = \tilde{f}(\underline{\boldsymbol{x}}_i). \tag{2.50}$$

The goal of the FEM approach is to solve for the coefficients $\tilde{f}_{m,i}$'s. In the Galerkin method, a linear system for the coefficient vector is obtained by testing the residual against the test basis functions. In this process, a so-called "weak form" is formulated.

#### *2.3.1.1 FEM Applied to Even-parity $S_N$ Equations*

The finite element approximation to the solution $\psi_m^+$ can be written as:

$$\tilde{\psi}_m^+(\underline{\boldsymbol{x}}) = \sum_{i=0}^{K} \tilde{\psi}_{m,i}^+ b_i(\underline{\boldsymbol{x}}), \tag{2.51}$$

where

$$\tilde{\psi}_{m,i}^+ = \tilde{\psi}_m^+(\underline{\boldsymbol{x}}_i). \tag{2.52}$$

The weak form of the Eq. (2.20) is obtained by multiplying the residual of Eq. (2.12) with the basis function and integrating over the whole spatial domain and setting it

to zero:

$$\int_V b_i \left[\vec{\Omega}_m \cdot \vec{\nabla}\tilde{\psi}_m^- + \sigma_t \tilde{\psi}_m^+ - Q_m^+\right] dV = 0, \quad \text{for } i = 1 \cdots K. \tag{2.53}$$

Next we apply Green's Theorem and integrate the gradient term by part:

$$\oint_{\partial V} b_i \tilde{\psi}_m^- \vec{\Omega}_m \cdot \vec{n} dA - \int_V [\tilde{\psi}_m^- \vec{\Omega}_m \cdot \vec{\nabla} b_i] dV + \int_V b_i [\sigma_t \tilde{\psi}_m^+ - Q_m^+] \, dV = 0. \tag{2.54}$$

According to boundary conditions Eq. (2.18) and Eq. (2.19), we can infer that:

$$\tilde{\psi}_m^- = -\left(\tilde{\psi}_m^+ - g_m\right), \qquad \text{for } \vec{\Omega}_m \cdot \vec{n} < 0, \tag{2.55}$$

$$\tilde{\psi}_m^- = \tilde{\psi}_m^+ - g_m, \qquad \text{for } \vec{\Omega}_m \cdot \vec{n} > 0. \tag{2.56}$$

Therefore:

$$\tilde{\psi}_m^- \vec{\Omega}_m \cdot \vec{n} = \left(\tilde{\psi}_m^+ - g_m\right) |\vec{\Omega}_m \cdot \vec{n}|, \qquad \text{for all } \vec{\Omega}_m. \tag{2.57}$$

Substituting from Eq. (2.57) into Eq. (2.54) to eliminate $\tilde{\psi}_m^-$ on the surface and from Eq. (2.21) into Eq. (2.54) to eliminate $\tilde{\psi}_m^-$ in the interior, we get:

$$\begin{aligned}\oint_{\partial V} b_i \tilde{\psi}_m^+ |\vec{\Omega}_m \cdot \vec{n}| dA - \oint_{\partial V} b_i g_m |\vec{\Omega}_m \cdot \vec{n}| dA + \int_V \left[\frac{\vec{\Omega}_m}{\sigma_t} \cdot \vec{\nabla}\tilde{\psi}_m^+ \vec{\Omega}_m \cdot \vec{\nabla} b_i\right] dV \\ - \int_V \left[\frac{Q_m^-}{\sigma_t} \vec{\Omega}_m \cdot \vec{\nabla} b_i\right] dV + \int_V b_i [\sigma_t \tilde{\psi}_m^+ - Q_m^+] \, dV = 0.\end{aligned} \tag{2.58}$$

Eq. (2.58) is the final expression for the weak form. Substituting from Eq. (2.51) into Eq. (2.58) gives us a $K \times K$ sparse SPD matrix that we can invert to find the solution vector $\left\{\psi_{m,i}^+\right\}$.

#### *2.3.1.2 FEM Applied to Least-squares $S_N$ Equations*

The finite element approximation to the solution $\psi_m$ can be written as:

$$\tilde{\psi}_m(\underline{\boldsymbol{x}}) = \sum_{i=1}^{K} \tilde{\psi}_{m,i} b_i(\underline{\boldsymbol{x}}), \tag{2.59}$$

where

$$\tilde{\psi}_{m,i} = \tilde{\psi}_m(\underline{\boldsymbol{x}}_i). \tag{2.60}$$

If we break the Eq. (2.40) into parts as follows:

$$\underbrace{-\vec{\Omega}_m \cdot \vec{\nabla}\vec{\Omega}_m \cdot \vec{\nabla}\psi_m}_{①} - \underbrace{\vec{\Omega}_m \psi_m \cdot \vec{\nabla}\sigma_t}_{②} + \underbrace{\sigma_t^2 \psi_m}_{③} = \underbrace{-\vec{\Omega}_m \cdot \vec{\nabla} Q_m}_{④} + \underbrace{\sigma_t Q_m}_{⑤},$$
$$m = 1, \ldots, N(N+2) \tag{2.61}$$

then the weak form can be obtained term by term:

LHS (left-hand-side):

$$\boxed{\int_V ① b_i dV}$$
$$= \int_V -b_i \vec{\Omega}_m \cdot \vec{\nabla}\vec{\Omega}_m \cdot \vec{\nabla}_m \psi_m dV \tag{2.62}$$
$$= -\oint_{\partial V} (\vec{\Omega}_m \cdot \vec{\nabla}\psi_m)\, b_i\, \vec{\Omega}_m \cdot \vec{n} dA + \int_V (\vec{\Omega}_m \cdot \vec{\nabla}\psi_m)(\vec{\Omega}_m \cdot \vec{\nabla} b_i) dV \tag{2.63}$$

$$\boxed{\int_V ②b_i dV}$$

$$= \int_V (-\vec{\Omega}_m \psi_m \cdot \vec{\nabla}\sigma_t)\ b_i\ dV = \int_V (-\vec{\Omega}_m \psi_m b_i \cdot \vec{\nabla}\sigma_t) dV \tag{2.64}$$

$$= -\oint_{\partial V} \sigma_t\ \psi_m b_i\ \vec{\Omega}_m \cdot \vec{n} dA + \int_V \sigma_t \vec{\nabla} \cdot (\vec{\Omega}_m \psi_m b_i) dV \tag{2.65}$$

$$= -\oint_{\partial V} \sigma_t\ \psi_m b_i\ \vec{\Omega}_m \cdot \vec{n} dA + \int_V \sigma_t b_i \vec{\Omega}_m \cdot \vec{\nabla}\psi_m dV + \int_V \sigma_t \psi_m \vec{\Omega}_m \cdot \vec{\nabla} b_i dV \tag{2.66}$$

$$\boxed{\int_V ③b_i dV}$$

$$= \int_V \sigma_t^2 \psi_m b_i dV \tag{2.67}$$

RHS (right-hand-side):

$$\boxed{\int_V ④b_i dV}$$

$$= \int_V (-\vec{\Omega}_m \cdot \vec{\nabla} Q_m) b_i dV \tag{2.68}$$

$$= -\oint_{\partial V} b_i Q_m \vec{\Omega}_m \cdot \vec{n} dA + \int_V Q_m \vec{\Omega}_m \cdot \vec{\nabla} b_i dV \tag{2.69}$$

$$\boxed{\int_V ⑤b_i dV}$$

$$= \int_V \sigma_t\ Q_m\ b_i\ dV \tag{2.70}$$

Applying boundary condition Eq. (2.42) for $\vec{\Omega}_m \cdot \vec{n} > 0$ and re-assembling the

weak form, we obtain:

$$\begin{aligned}
\text{LHS} := &- \cancel{\oint_{\partial V} Q_m\, b_i\, \vec{\Omega}_m \cdot \vec{n} dA}^{\text{II}} + \cancel{\oint_{\partial_V} \sigma_t \psi_m b_i \vec{\Omega}_m \cdot \vec{n} dA}^{\text{I}} \\
&+ \int_V (\vec{\Omega}_m \cdot \vec{\nabla}\psi_m)(\vec{\Omega}_m \cdot \vec{\nabla} b_i) dV \\
&- \cancel{\oint_{\partial V} \sigma_t\, \psi_m b_i\, \vec{\Omega}_m \cdot \vec{n} dA}^{\text{I}} + \int_V \sigma_t b_i \vec{\Omega}_m \cdot \vec{\nabla}\psi_m dV + \int_V \sigma_t \psi_m \vec{\Omega}_m \cdot \vec{\nabla} b_i dV \\
&+ \int_V \sigma_t^2 \psi_m b_i dV \qquad (2.71) \\
\text{RHS} := &- \cancel{\oint_{\partial V} b_i Q_m \vec{\Omega}_m \cdot \vec{n} dA}^{\text{II}} + \int_V Q_m \vec{\Omega}_m \cdot \vec{\nabla} b_i dV \\
&+ \int_V \sigma_t\, Q_m\, b_i\, dV \qquad (2.72)
\end{aligned}$$

for $\vec{\Omega}_m \cdot \vec{n} > 0$

We can see that the "I" terms cancels each other out, and the same for the "II" terms. After the cancellation, the weak form for $\vec{\Omega}_m \cdot \vec{n} > 0$ becomes:

$$\begin{aligned}
\text{LHS} := &\int_V (\vec{\Omega}_m \cdot \vec{\nabla}\psi_m)(\vec{\Omega}_m \cdot \vec{\nabla} b_i) dV \\
&+ \int_V \sigma_t b_i \vec{\Omega}_m \cdot \vec{\nabla}\psi_m dV + \int_V \sigma_t \psi_m \vec{\Omega}_m \cdot \vec{\nabla} b_i dV \\
&+ \int_V \sigma_t^2 \psi_m b_i dV \qquad (2.73) \\
\text{RHS} := &\int_V Q_m \vec{\Omega}_m \cdot \vec{\nabla} b_i dV \\
&+ \int_V \sigma_t\, Q_m\, b_i\, dV \qquad (2.74)
\end{aligned}$$

for $\vec{\Omega}_m \cdot \vec{n} > 0$

For $\vec{\Omega}_m \cdot \vec{n} \leq 0$, applying the Dirichlet boundary condition to the support points on

the boundary will overwrite the weak form for those DoF's, and those surface integral will only appear in the weak form for the degree of freedoms (DoF) associated with the boundary support points. Without introducing any error, we can simply drop those surface integrals and write down the weak form for the interior as:

$$\begin{aligned}\text{LHS} := &\int_V (\vec{\Omega}_m \cdot \vec{\nabla}\psi_m)(\vec{\Omega}_m \cdot \vec{\nabla} b_i) dV \\ &+ \int_V \sigma_t b_i \vec{\Omega}_m \cdot \vec{\nabla}\psi_m dV + \int_V \sigma_t \psi_m \vec{\Omega}_m \cdot \vec{\nabla} b_i dV \\ &+ \int_V \sigma_t^2 \psi_m b_i dV \end{aligned} \tag{2.75}$$

$$\begin{aligned}\text{RHS} := &\int_V Q_m \vec{\Omega}_m \cdot \vec{\nabla} b_i dV \\ &+ \int_V \sigma_t \; Q_m \; b_i \; dV \end{aligned} \tag{2.76}$$

for $\vec{\Omega}_m \cdot \vec{n} \leq 0$

Therefore, we can see that we have a consistent weak form for both $\vec{\Omega}_m \cdot \vec{n} > 0$ and $\vec{\Omega}_m \cdot \vec{n} \leq 0$. The unified weak form is complemented by the Dirichlet boundary condition Eq. (2.41) for $\vec{\Omega}_m \cdot \vec{n} \leq 0$ only. Also, in order to keep the system matrix SPD and make use of the CG solver, one needs to remove those Dirichlet DoF's completely from the linear system, instead of simply overwriting the weak form for those DoF's.

### *2.3.2 Solution by Direction - Iterative Solution Techniques*

The $S_N$ equations along the different directions are coupled through the scattering operator. Therefore, we have to solve the equations direction by direction and converge the angular dependency in the solution iteratively. To this end, we use Source Iteration (SI), a commonly used technique for solving the $S_N$ equations.

Diffusion Synthetic Acceleration (DSA) is also employed to accelerate the SI when applicable. We review briefly these techniques in the following sections.

#### *2.3.2.1 Source Iteration*

The total source contributions appearing on the right-hand-side (RHS) are lagged for all directions (computed with the angular intensity unknowns at iteration $(\ell)$), and, for each direction $m$, the resulting decoupled diffusion-like equations are solved for the angular intensities for the next iteration $(\ell+1)$:

For Even-parity $S_N$ equations, a single iteration of the source iteration is given as follows:

$$-\vec{\Omega}_m \cdot \vec{\nabla} \frac{1}{\sigma_t} \vec{\Omega}_m \cdot \vec{\nabla} \psi_m^{+,(\ell+1)} + \sigma_t \psi_m^{+,(\ell+1)} = Q_m^{+,(\ell)} - \vec{\Omega}_m \cdot \vec{\nabla} \frac{Q_m^{-,(\ell)}}{\sigma_t}, \tag{2.77}$$

where $m = 1, \cdots, \frac{N(N+2)}{2}$ and $\ell$ is the iteration index. The total source is updated using the most recent values $\psi_m^{+,(\ell+1)}$ for the next iteration; it is straightforward to compute the even angular moments from $\psi_m^+$, and thus it is obvious to update $Q_m^+$. To update $Q_m^-$, one needs the odd angular moments, and thus $\psi_m^-$ which is obtained from:

$$\psi_m^{-,(\ell+1)} = -\frac{\vec{\Omega}_m}{\sigma_t} \cdot \vec{\nabla} \psi_m^{+,(\ell+1)} + \frac{1}{\sigma_t} Q_m^{-,(\ell)}, \qquad m = 1, \cdots, \frac{N(N+2)}{2}. \tag{2.78}$$

For Least-squares $S_N$ equations, a single iterate of the source iteration is given as follows:

$$-\vec{\Omega}_m \cdot \vec{\nabla} \vec{\Omega}_m \cdot \vec{\nabla} \psi_m^{(\ell+1)} - \vec{\Omega}_m \psi_m^{(\ell+1)} \cdot \vec{\nabla} \sigma_t + \sigma_t^2 \psi_m^{(\ell+1)} = -\vec{\Omega}_m \cdot \vec{\nabla} Q_m^{(\ell)} + \sigma_t Q_m^{(\ell)}$$
$$m = 1, \ldots, N(N+2) \tag{2.79}$$

#### *2.3.2.2 Diffusion Synthetic Acceleration*

SI can be very slowly converging when the scattering ratio $c = \sigma_s/\sigma_t$ is close to 1.0. As $c$ approaches unity, low-frequency error modes are not sufficiently attenuated by the SI process and the spectral radius of SI approaches unity, making SI a poor scheme to employ in highly diffusive configurations. However, for weakly anisotropic scattering, diffusion synthetic acceleration (DSA) can effectively attenuate the low-frequency error modes. The idea of DSA is to use a lower order diffusion equation to evaluate the iterative error after each SI step. In order to obtain the diffusion operator, we assume linear angular dependency in $\psi(\underline{\boldsymbol{x}}, \Omega)$:

$$\psi(\underline{\boldsymbol{x}}, \Omega) = \frac{\phi(\underline{\boldsymbol{x}}) + 3\vec{J}(\underline{\boldsymbol{x}}) \cdot \vec{\Omega}}{4\pi}. \tag{2.80}$$

For Even-parity $S_N$ equations, we obtain the even- and odd-parity components as:

$$\psi^+ = \frac{\psi(\vec{\Omega}) + \psi(-\Omega)}{2} = \frac{\phi}{4\pi}, \tag{2.81}$$

$$\psi^- = \frac{\psi(\vec{\Omega}) - \psi(-\Omega)}{2} = \frac{3\vec{J} \cdot \vec{\Omega}}{4\pi}. \tag{2.82}$$

Substituting from Eq. (2.81) into Eq. (2.12), we get:

$$\vec{\Omega} \cdot \vec{\nabla} \frac{3\vec{J} \cdot \vec{\Omega}}{4\pi} + \sigma_t \frac{\phi}{4\pi} = Q^+. \tag{2.83}$$

Substituting from Eq. (2.82) into Eq. (2.13), we get:

$$\vec{\Omega} \cdot \vec{\nabla} \frac{\phi}{4\pi} + \sigma_t \frac{3\vec{J} \cdot \vec{\Omega}}{4\pi} = Q^-. \tag{2.84}$$

Then by substituting from Eq. (2.84) into Eq. (2.83) to eliminate the $\vec{J}\cdot\vec{\Omega}$, we obtain:

$$-\vec{\Omega}\cdot\vec{\nabla}\frac{\vec{\Omega}}{\sigma_t}\cdot\vec{\nabla}\frac{\phi}{4\pi}+\sigma_t\frac{\phi}{4\pi}=Q^{+}-\vec{\Omega}\cdot\vec{\nabla}\frac{Q^{-}}{\sigma_t}. \tag{2.85}$$

Finally, integrating Eq. (2.85) with respect to $\Omega$ over $4\pi$ while assuming isotropic scattering, we obtain diffusion equation:

$$-\vec{\nabla}\frac{1}{3\sigma_t}\vec{\nabla}\phi+\sigma_a\phi=q, \tag{2.86}$$

where $q$ is the total contribution from the external source:

$$q=\int_{4\pi}\left(\frac{S(\vec{\Omega})+S(-\vec{\Omega})}{2}-\vec{\Omega}\cdot\vec{\nabla}\frac{S(\vec{\Omega})+S(-\vec{\Omega})}{2\sigma_t}\right)d\Omega. \tag{2.87}$$

One step of the SI+DSA combination is as follows. First, an SI of the original Even-parity $S_N$ equations are performed to solve for the angular intensities at the mid-stage ($\psi^{(\ell+1/2)}$):

$$-\vec{\Omega}_m\cdot\vec{\nabla}\frac{1}{\sigma_t}\vec{\Omega}_m\cdot\vec{\nabla}\psi_m^{+,(\ell+1/2)}+\sigma_t\psi_m^{+,(\ell+1/2)}=Q_m^{+,(\ell)}-\vec{\Omega}_m\cdot\vec{\nabla}\frac{Q_m^{-,(\ell)}}{\sigma_t}, \tag{2.88}$$

$$\psi_m^{-,(\ell+1)}=-\frac{\vec{\Omega}_m}{\sigma_t}\cdot\vec{\nabla}\psi_m^{+,(\ell+1)}+\frac{1}{\sigma_t}Q_m^{-,(\ell)}. \tag{2.89}$$

And the angular integrated intensity at the mid-stage ($\phi^{(\ell+1/2)}$) is computed as:

$$\phi^{(\ell+1/2)}=\sum_{m=1}^{N(N+2)/2}2\;\psi_m^{+,(\ell+1/2)}w_m. \tag{2.90}$$

Second, a low order estimate of the correction $\delta\phi^{(\ell+1/2)}$ is obtained by means of a diffusion solve (Eq. (2.86)) acting on the difference of two successive iterates of the

scattering source:

$$-\vec{\nabla}\frac{1}{3\sigma_t}\vec{\nabla}\delta\phi^{(\ell+1/2)} + \sigma_a\delta\phi^{(\ell+1/2)} = \sigma_s(\phi^{(\ell+1/2)} - \phi^{(\ell)}). \tag{2.91}$$

Finally, the next iterate for the angular integrated intensity is given by:

$$\phi^{(\ell+1)} = \phi^{(\ell+1/2)} + \delta\phi^{(\ell+1/2)}. \tag{2.92}$$

The DSA is also possible for the Least-squares $S_N$ equations but it is not implemented and tested in this research. For detail about the DSA scheme for Least-squares $S_N$ equations, we refer the reader to [8]. For additional details regarding the general DSA technique, we refer the reader to [1].

# 3. LOWER-RESOLUTION RADIATION TRANSPORT MODELS: $SP_N$*

The Even-parity $S_N$ equations can become very expensive to solve as $N$ increases, in terms of both computational cost and memory cost, as its number of unknowns is on the order of $O(N^2)$. In response to this difficulty, the Simplified $P_N$ ($SP_N$) equations are developed as an inexpensive alternative, with the number of unknowns on the order of $O(N)$. The $SP_N$ equations were first derived by Gelbard in the early 1960s as a means of obtaining a multidimensional transport approximation that captured a significant amount of the physics of the $P_N$ approximation at a relatively low computational cost [4, 5, 6]. The derivation of the $SP_N$ equations is usually presented in one of three manners: (i) heuristically, by writing the one dimensional $P_N$ equations in slab geometry, replacing the $d/dx$ spatial derivatives with $\vec{\nabla}$ for the even intensity moments and with $\vec{\nabla}\cdot$ for odd intensity moments, and then eliminating the odd-moments from the even-moment equations [10]; (ii) by means of an asymptotic analysis [10, 17]; or (iii) with a variational approach [17, 3].

Despite the relatively heuristic original derivation by Gelbard, and significant reduction of the number of unknowns, the $SP_N$ equations are shown and proven to be a surprisingly good approximation when the problem is very diffusive and scattering dominant [10], or when the solution is locally 1-D [17]. Furthermore, in slab geometry (1-D problems) the $SP_N$ equations are always equivalent to the $S_{N+1}$ equations (with a proper angular quadrature set) and the $P_N$ equations (with $N$ odd). In this section, we will review various commonly used $SP_N$ formulations together with their suitable iterative solution techniques, and determine the best

*Reprinted with permission from "Iterative performance of various formulations of the $SP_N$ equations" by Y. Zhang, J. Ragusa, and J. Morel, 2013. Journal of Computational Physics, 252, 558-572, Copyright [2013] by Elsevier.

performing one for our application.

## 3.1 $SP_N$ Formalisms

The 1-D $P_N$ equations form a system of $N+1$ first-order coupled equations, but the multidimensional $SP_N$ equations are usually expressed as a system of $M = (N+1)/2$ coupled diffusion equations. We restrict our study to the most common diffusion-like formulations of the $SP_N$ equations: (i) the so-called standard form, obtained by elimination of the odd intensity moments from the odd equations [10], (ii) the composite-moment form, obtained by operating a change of variables on the standard form [12, 20], and (iii) the canonical form [10, 16], obtained from the standard form by a similarity transformation. The standard form results in three Laplacian-like operators coupling three even intensity moments per equation. The composite form transforms the standard form such that a single Laplacian-like operator is present in each equation with a reaction (mass) operator coupling all moments together; this form was originally suggested by Gelbard because it is easily implementable in a multigroup diffusion code. The canonical form, formally derived by invoking the equivalence between the 1-D $P_N$ equations and the 1-D $S_{N+1}$ equations, also yields a single "Laplacian" operator per intensity unknown but couples all of the unknowns via a scattering operator.

### *3.1.1 Standard Form of $SP_N$*

We briefly present the standard form of the $SP_N$ equations, details of derivation can be found, for instance, in [10]. Starting from the 1-D $P_N$ transport equations, the $SP_N$ equations are obtained by first replacing the spatial derivatives of the even moments with $\vec{\nabla}$ operator and the spatial derivatives of the odd moments with the $\vec{\nabla}\cdot$ operator. Implicit in this substitution is the assumption that the even-moments

are scalars and the odd-moments are vectors, yielding

$$\frac{n}{2n+1}\vec{\nabla}\cdot\vec{\phi}_{n-1}+\frac{n+1}{2n+1}\vec{\nabla}\cdot\vec{\phi}_{n+1}+\sigma_n\phi_n=S_n \qquad n=0,2,\ldots,N-1, \tag{3.1a}$$

$$\frac{n}{2n+1}\vec{\nabla}\phi_{n-1}+\frac{n+1}{2n+1}\vec{\nabla}\phi_{n+1}+\sigma_n\vec{\phi}_n=\vec{S}_n \qquad n=1,3,\ldots,N, \tag{3.1b}$$

(with the closure convention that $\vec{\phi}_{-1}=0$ and $\phi_n=0=\vec{\phi}_n$ for $n>N$). Here, $S_n$ denotes an even moment of the external source and $\vec{S}_n$ an odd source moment. $\sigma_n$ is defined as

$$\sigma_n=\sigma_t-\sigma_{s,n}, \tag{3.2}$$

where $\sigma_t$ is the total cross section and $\sigma_{s,n}$ is the $n$-th Legendre moment of the scattering cross section. Eqs. (3.1) are next manipulated to eliminate the odd intensity moments from the odd equations, yielding the standard form of the $SP_N$ equations as a system of coupled diffusion-like equations

$$\begin{aligned}
&-\vec{\nabla}\cdot\left[\frac{1}{\sigma_{n-1}}\frac{n(n-1)}{(2n+1)(2n-1)}\right]\vec{\nabla}\phi_{n-2}\\
&\quad-\vec{\nabla}\cdot\left[\frac{1}{\sigma_{n-1}}\frac{n^2}{(2n+1)(2n-1)}+\frac{1}{\sigma_{n+1}}\frac{(n+1)^2}{(2n+3)(2n+1)}\right]\vec{\nabla}\phi_n\\
&\quad-\vec{\nabla}\cdot\left[\frac{1}{\sigma_{n+1}}\frac{(n+2)(n+1)}{(2n+3)(2n+1)}\right]\vec{\nabla}\phi_{n+2}+\sigma_n\phi_n\\
&\quad=S_n-\vec{\nabla}\cdot\left(\frac{1}{\sigma_{n-1}}\frac{n}{2n+1}\vec{S}_{n-1}+\frac{1}{\sigma_{n+1}}\frac{n+1}{2n+1}\vec{S}_{n+1}\right)
\end{aligned} \tag{3.3}$$

for $n=0,\,2,\,\ldots,N-1$. Introducing a matrix notation, Eq. (3.3) can be written concisely as

$$-\vec{\nabla}\cdot\left[K^{std}\vec{\nabla}\Phi^e\right]+\Sigma^e\Phi^e=S^e-\vec{\nabla}\cdot\left(C^{std}(\Sigma^o)^{-1}\vec{S}^o\right), \tag{3.4}$$

where $\Phi^e = [\phi_0, \phi_2, \ldots \phi_{N-1}]$ represents the vector even intensity moments, $S^e$ and $\vec{S}^o$ the vector of even/odd source moments. $\Sigma^e$, $\Sigma^o$, $C^{std}$, and $K^{std}$ are matrices of size $M \times M$. $\Sigma^e$ and $\Sigma^o$ are diagonal matrices containing the even/odd values of the cross section $\sigma_n$, respectively. $K^{std}$ is a tridiagonal matrix and $C^{std}$ is lower bi-diagonal. Their entries, for any row $i = n/2 + 1$ $(1 \leq i \leq M)$, are given below:

$$\begin{aligned}
K^{std}_{i,i-1} &= \frac{1}{\sigma_{n-1}} \frac{n(n-1)}{(2n+1)(2n-1)} \\
K^{std}_{i,i} &= \frac{1}{\sigma_{n-1}} \frac{n^2}{(2n+1)(2n-1)} + \frac{1}{\sigma_{n+1}} \frac{(n+1)^2}{(2n+3)(2n+1)} \\
K^{std}_{i,i+1} &= \frac{1}{\sigma_{n+1}} \frac{(n+2)(n+1)}{(2n+3)(2n+1)} \\
C^{std}_{i,i-1} &= \frac{n}{2n+1} \\
C^{std}_{i,i} &= \frac{n+1}{2n+1}.
\end{aligned}$$

$K^{std}$ can actually be written as the sum of a lower bidiagonal matrix and an upper bidiagonal matrix (whose coefficients depend on $n$ only) multiplied by $(\Sigma^o)^{-1}$. Since $K^{std}$ is tridiagonal, it is obvious that three consecutive even intensity moments are coupled via Laplacian operators. Note that the reaction term only involves one even intensity moment since $\Sigma^e$ is diagonal.

### *3.1.2 Composite Form of $SP_N$*

In the composite form of the $SP_N$ equations, a composite intensity variable, denoted here by $\digamma$, is used. $\digamma$ is a linear combination of two even intensity moments. Usually, the derivation of this form is presented starting from the standard 1-D $P_N$ equations. However, in order to obtain more amenable coefficients, an alternate normalization is employed in the 1-D $P_N$ equations [12, 20], in which the 1-D angular

intensity and its moments are expressed as

$$\psi(x,\mu) = \sum_{\ell=0}^{\infty} \alpha_\ell \phi_\ell(x) P_\ell(\mu), \tag{3.5a}$$

where

$$\phi_\ell(x) = \frac{2\ell+1}{2\alpha_\ell} \int_{-1}^{1} d\mu\, \psi(x,\mu) P_\ell(\mu), \tag{3.5b}$$

(similar expressions hold for the source moments). Note that if $\alpha_n = \frac{2n+1}{2}$, the standard expression for the $P_N$ equations is recovered. However, the final expressions are greatly simplified by the following choice for $\alpha_n$

$$\alpha_0 = 1, \qquad \alpha_n = \frac{4n^2-1}{n\alpha_{n-1}} \text{ for } n > 0,$$

and the following redefinitions

$$\sigma_n \leftarrow \frac{\alpha_n^2}{2n+1}(\sigma_t - \sigma_{s,n}), \qquad S_n \leftarrow \frac{\alpha_n^2}{2n+1} S_n.$$

Replacing the spatial derivatives with the appropriate 3-D operators yields the following equations:

$$\vec{\nabla}\cdot\vec{\phi}_{n-1} + \vec{\nabla}\cdot\vec{\phi}_{n+1} + \sigma_n \phi_n = S_n \qquad \text{for } 0 \le n \le N-1 \text{ even}, \tag{3.6a}$$

$$\vec{\nabla}\phi_{n-1} + \vec{\nabla}\phi_{n+1} + \sigma_n \vec{\phi}_n = \vec{S}_n. \qquad \text{for } 1 \le n \le N \text{ odd}. \tag{3.6b}$$

Obviously, Eq. (3.1) and Eq. (3.6) are very similar; the alternate normalization has simply yielded a form more amenable to the introduction of the composite moments for any order $N$ (for the reader interested in the composite form with the standard normalization, we suggest Gelbard's original article [4] where the $SP_3$ equations

are given and a recent article by Klose et al.[9] for all equations up to $SP_7$ ). To obtain the composite form of the $SP_N$ equations, the composite intensity moments $\mathcal{F}_{1+n/2} = \phi_n + \phi_{n+2}$ for any even $n$ (i.e. $n = 0, 2, \ldots, N-1$) are introduced. This relationship can conveniently be written as

$$\mathcal{F} = C\Phi^e, \tag{3.7}$$

with the vector of composite moments $\mathcal{F} = [\mathcal{F}_1, \mathcal{F}_2, \ldots, \mathcal{F}_M]^T$ and, again, the vector of even intensity moments $\Phi^e = [\phi_0, \phi_2, \ldots, \phi_{N-1}]^T$. $C$ is a simple matrix of size $M \times M$ coupling the various even moments ($C_{ij} = 1$ for $i = j$ and $i = j - 1$, and $C_{ij} = 0$ otherwise). Here, matrix $C$ has the same bidiagonal structure has $C^{std}$ of the standard form, but with simpler entries. Introducing the vector of odd angular moments, $\vec{\Phi}^o = [\vec{\phi}_1, \ldots, \vec{\phi}_N]^T$, Eqs. (3.6) become

$$\vec{\nabla}\cdot\vec{\Phi}^o + C^{-T}\Sigma^e C^{-1}\mathcal{F} = C^{-T}S^e, \tag{3.8a}$$

$$\vec{\nabla}\mathcal{F} + \Sigma^o\vec{\phi}^o = \vec{S}^o, \tag{3.8b}$$

where $\Sigma^e, \Sigma^o$ are the same diagonal matrices previously defined. The even/odd sources, $S^e$ and $\vec{S}^o$, follow the same definitions as $\Phi^e$ and $\vec{\Phi}^o$. We can combine this first-order system into the diffusion-like composite moment $SP_N$ formulation by inserting the odd intensity moments $\vec{\Phi}^o$ from equation Eq. (3.8b) into equation Eq. (3.8a). Therefore, the composite even moments formulation of the $SP_N$ equations is given by:

$$-\vec{\nabla}\cdot(\Sigma^o)^{-1}\vec{\nabla}\mathcal{F} + B^{cmp}\mathcal{F} = C^{-T}S^e - \vec{\nabla}\cdot(\Sigma^o)^{-1}\vec{S}^o, \tag{3.9}$$

with

$$B^{cmp} = C^{-T}\Sigma^{e}C^{-1}. \tag{3.10}$$

Eq. (3.9) contains a single Laplacian operator acting only upon a single composite intensity per equation (this is the analogous of having $K^{std}$ be a diagonal matrix in the standard form), but the reaction operator matrix $B^{cmp}$ is now a full matrix (where the off-diagonal terms are akin to up/downscattering terms); this reaction operator couples all composite moments together. In the early days of the $SP_N$ theory, this composite moment formulation was found particularly attractive because any multigroup diffusion code could solve the composite moment $SP_N$ equations with virtually no modifications. Finally, we note that any even intensity moment can be easily obtained by inverting relation Eq. (3.7), yielding

$$\phi_n = \sum_{i=n/2+1}^{M} (-1)^{n/2+1+i} F_i = F_{n+1} - F_{n+2} + \ldots + (-1)^{M+1+n/2} F_M. \tag{3.11}$$

In particular, the angle-integrated intensity $\phi_0$ is obtained by letting $n = 0$ in Eq. (3.11).

### *3.1.3 Canonical Form of $SP_N$*

The canonical form of the $SP_N$ equations was introduced in [10, 16]. The derivation of this form relies on a similarity transformation between the 1-D $P_N$ equation and the 1-D $S_{N+1}$ equations with Gauss quadrature and $P_N$ scattering cross-section expansion. The 1-D $S_{N+1}$ equations are

$$\mu_m \frac{d\psi_m}{dx} + \sigma_t \psi_m = Q_m, \qquad m = 1, \ldots, N+1, \tag{3.12}$$

where $m$ denotes the direction index in the Gaussian quadrature $(w_m, \mu_m)_{1 \leq m \leq N+1}$ and the total directional source is given by

$$Q_m = \sum_{n=0}^{N} \frac{2n+1}{2} \sigma_{s,n} P_n(\mu_m) \phi_n \ + S_m, \tag{3.13}$$

with $S_m$ the angular external source. Introducing the even/odd parity angular intensities

$$\psi^{\pm}(\mu_m) = \frac{1}{2} \left( \psi(\mu_m) \pm \psi(-\mu_m) \right), \tag{3.14}$$

we can re-cast the $S_{N+1}$ equations as

$$\mu_m \frac{d\psi_m^-}{dx} + \sigma_t \psi_m^+ = Q_m^+, \tag{3.15a}$$

$$\mu_m \frac{d\psi_m^+}{dx} + \sigma_t \psi_m^- = Q_m^-, \tag{3.15b}$$

(for $m = 1, \ldots, M = \frac{N+1}{2}$) where the total source terms $Q_m^{\pm}$ are given by

$$Q_m^+ = \sum_{n=0,2,\ldots}^{N-1} (2n+1) \sigma_{s,n} P_n(\mu_m) \phi_n \ + S_m^+, \tag{3.16a}$$

$$Q_m^- = \sum_{n=1,3,\ldots}^{N} (2n+1) \sigma_{s,n} P_n(\mu_m) \phi_n \ + S_m^-. \tag{3.16b}$$

The definition for $S_m^{\pm}$ is identical to the one given in Eq. (3.14) for for $\psi_m^{\pm}$. The intensity moments are computed using the quadrature rule

$$\phi_n = \begin{cases} \sum_{m=1}^{M} w_m P_n(\mu_m) \psi_m^+ & \text{for } n \text{ even} \\ \sum_{m=1}^{M} w_m P_n(\mu_m) \psi_m^- & \text{for } n \text{ odd.} \end{cases} \tag{3.17}$$

The canonical form of the $SP_N$ equations is obtained by (a) replacing the spatial derivatives with $\vec{\nabla}\cdot$ in Eq. (3.15a) and with $\vec{\nabla}$ in Eq. (3.15b), and (b) by eliminating the odd unknowns $\vec{\psi}_m^-$ into the even equations, yielding

$$-\mu_m^2 \vec{\nabla}\cdot\frac{1}{\sigma_t}\vec{\nabla}\psi_m^+ + \sigma_t\psi_m^+ = Q_m^+ - \mu_m\vec{\nabla}\cdot\left(\frac{\vec{Q}_m^-}{\sigma_t}\right) \text{ for } m = 1,\ldots,M. \tag{3.18a}$$

$$\vec{\psi}_m^- = -\frac{\mu_m}{\sigma_t}\vec{\nabla}\psi_m^+ + \frac{\vec{Q}_m^-}{\sigma_t} \tag{3.18b}$$

In order to re-cast the canonical form using a matrix notation, we re-write Eq. (3.16) as

$$Q^+ = M^+\Sigma^+D^+\Psi^+ + S^+ = H^+\Psi^+ + S^+, \tag{3.19a}$$

$$\vec{Q}^- = M^-\Sigma^-D^-\vec{\Psi}^- + \vec{S}^- = H^-\vec{\Psi}^- + \vec{S}^-, \tag{3.19b}$$

where the parity total source vectors $Q^+ = [Q_1^+,\ldots,Q_M^+]^T$ and $\vec{Q}^- = [\vec{Q}_1^-,\ldots,\vec{Q}_M^-]^T$ are expressed using $M^\pm$, the moment-to-discrete matrix, $D^\pm$, the discrete-to-moment matrix, and $\Sigma^\pm$, the diagonal scattering matrix containing the even/odd coefficients $\sigma_n$. The vectors of parity intensities are $\Psi^+ = [\psi_1^+,\ldots,\psi_M^+]^T$ and $\vec{\Psi}^- = [\vec{\psi}_1^-,\ldots,\vec{\psi}_M^-]^T$. And similarly are the vectors of parity sources, $S^+$ and $\vec{S}^-$. In the above formulation, we have actually borrowed the standard scattering source representation employed in $S_N$ codes but used the matrix representation of the Galerkin quadrature method [13]. Finally, the odd intensity is eliminated from the $\vec{Q}^-$ expression using

$$\vec{\Psi}^- = \left(I - \frac{H^-}{\sigma_t}\right)^{-1}\frac{\vec{S}^- - W\vec{\nabla}\Psi^+}{\sigma_t} \tag{3.20}$$

($W$ = diagonal matrix containing the direction cosine $\mu_m$'s), yielding

$$
\begin{aligned}
-\vec{\nabla}\cdot K^{can}\vec{\nabla}\Psi^{+} + \sigma_t\Psi^{+} & \\
&= H^{+}\Psi^{+} + W\vec{\nabla}\cdot\left(\frac{H^{-}}{\sigma_t}\left(I-\frac{H^{-}}{\sigma_t}\right)^{-1}W\vec{\nabla}\right)\Psi^{+} \\
&\quad + S^{+} - W\vec{\nabla}\cdot\left(I-\frac{H^{-}}{\sigma_t}\right)^{-1}\vec{S}^{-}, \quad (3.21)
\end{aligned}
$$

where $K^{can}$ is an $M \times M$ diagonal matrix, with entries equal to $\frac{\mu_m^2}{\sigma_t}$ ($K^{can} = W^2/\sigma_t$). The left-hand-side of Eq. (3.21) is clearly diagonal (no coupling between the various $\psi_m^+$'s), thus these diffusion-like equations can be solved simultaneously. However, the coupling between the various moments occurs in the right-hand-side through the scattering source contributions. It is also obvious that a natural iterative technique to solve Eq. (3.18) is standard Source Iteration (SI) with preconditioning as commonly used in $S_N$ codes.

### *3.1.4 $SP_N$ Boundary Conditions*

As with the Even-parity $S_N$ equations, we used Mark type boundary conditions for the all forms of $SP_N$ equations. The difference is that because the 3-D $SP_N$ equations are generalized from 1-D angular dependency, there is no real 3-D direction variable $\vec{\Omega}_m$ present in the $SP_N$ equations. Instead, a 1-D direction cosine, $\mu_m$ serves as a direction indicator. And the $\mu_m$ is defined with respect to the normal vector of the surface where is boundary condition is given. For the incoming directions ($\mu_m < 0$)

$$\psi(\mu_m) = \psi_m^{+} + \vec{\psi}_m^{-}\cdot\vec{n} = g(\mu_m) = g_m. \quad (3.22)$$

Or in terms of the out-going directions ($\mu_m > 0$):

$$\psi(\mu_m) = \psi_m^+ - \vec{\psi}_m^- \cdot \vec{n} = g(\mu_m) = g_m \tag{3.23}$$

Analogous to the treatment to Even-parity $S_N$ equations, we renormalize the $g_m$ as follows:

$$g_m' = g_m \frac{\int_{\mu<0} g(\mu)|\mu| d\mu}{\sum_{m|\mu_m<0} g_m |\mu_m| w_m} \tag{3.24}$$

## 3.2 $SP_N$ Solution Techniques

For all the $SP_N$ forms, we still use the first order continuous finite element spatial discretization technique to solve the diffusion-like equations along each direction. The angular iterative scheme, however, is tailored to each specific formalism. For the standard form, we used Gauss-Seidel iteration; For the composite-moment form, we used both Gauss-Seidel and EXPLICIT iteration; For the canonical form, we used the SI due to its structural similarity to the Even-parity $S_N$ equations.

### *3.2.1 Spatial Discretization*

In this section we present the weak forms for all the $SP_N$ formalism within our consideration. Mark boundary condition implementation for standard and composite-moment forms are discussed in detail, as well as the special treatment for discretizing the odd-parity equations (Eq. (3.15b)) in the canonical form.

#### *3.2.1.1 Standard Form*

The weak form of the standard $SP_N$ equations can be obtained by multiplying the Eq. (3.1a) by a basis function ($b_i$) in the trial space and integrating over the

volume:

$$\underbrace{\oint_{\partial V} b_i \beta_n \tilde{\vec{\phi}}_{n-1} \cdot \vec{n} dA + \oint_{\partial V} b_i \gamma_n \tilde{\vec{\phi}}_{n+1} \cdot \vec{n} dA}_{\text{surface}} - \underbrace{\int_V \beta_n \tilde{\vec{\phi}}_{n-1} \cdot \vec{\nabla} b_i dV - \int_V \gamma_n \tilde{\vec{\phi}}_{n+1} \cdot \vec{\nabla} b_i dV}_{\text{interior}}$$
$$+ \int_V b_i \sigma_n \tilde{\phi}_n dV = \int_V b_i S_n dV, \quad n = 0, 2, \ldots, N-1, \quad (3.25)$$

where

$$\beta_n = \frac{n}{2n+1}, \quad (3.26)$$
$$\gamma_n = \frac{n+1}{2n+1}. \quad (3.27)$$

In order to eliminate the odd moments in the boundary term, we first assume an angular intensity reconstruction:

$$\psi(\underline{\boldsymbol{x}}, \mu) = \sum_{n \text{ even}} \frac{2n+1}{2} \phi_n(\underline{\boldsymbol{x}}) P_n(\mu) + \sum_{n \text{ odd}} \frac{2n+1}{2} \vec{\phi}_n(\underline{\boldsymbol{x}}) \cdot \vec{n} P_n(\mu) \quad (3.28)$$

Note that this reconstruction is rigorous in 1-D but generally not in 3-D. By inserting Eq. (3.28) into Eq. (3.22), we get a relationship between the even moments ($\Phi^e$) and the normal component of the odd moments ($\vec{\Phi}^o \cdot \vec{n}$) on the boundary, in the matrix notation as follows:

$$O^{std} \vec{\Phi}^o \cdot \vec{n} = g' - E^{std} \Phi^e \quad (3.29)$$

where

$$\begin{aligned} O^{std}_{i,j} &= \frac{4j-1}{2} P_{2j-1}(\mu_i) \\ E^{std}_{i,j} &= \frac{4j-3}{2} P_{2j-2}(\mu_i) \\ g' &= \left[ g'_1, g'_2, \ldots, g'_{\frac{N+1}{2}} \right]^T \end{aligned}$$

By inserting Eq. (3.29) into Eq. (3.25) to eliminate the $\vec{\phi}^o$ in the surface term and by inserting Eq. (3.1b) into Eq. (3.25) to eliminate the $\vec{\phi}^o$ in the interior term, we can re-express the weak form in a matrix notation as follows:

$$\begin{aligned} &- \oint_{\partial V} b_i G^{std} \left(O^{std}\right)^{-1} E^{std} \tilde{\Phi}^e dA + \int_V \vec{\nabla} b_i \cdot K^{std} \vec{\nabla} \tilde{\Phi}^e dV + \int_V b_i \Sigma^e \tilde{\Phi}^e dV \\ &\quad = \int_V b_i S^e dV + \int_V \vec{\nabla} b_i \cdot \left[ C^{std} (\Sigma^o)^{-1} \vec{S}^o \right] dV - \oint_{\partial V} b_i G^{std} \left(O^{std}\right)^{-1} g' dA, \end{aligned} \quad (3.30)$$

where $G^{std}$ is a $M \times M$ matrix. Its entries, for any row $i = 1 \cdots M$, are given below:

$$\begin{aligned} G^{std}_{i,i} &= \gamma_{n+1}, \\ G^{std}_{i,i-1} &= \beta_{n-1}, \end{aligned}$$

where

$$n = 2(i-1) \quad (3.31)$$

#### *3.2.1.2 Composite-moment Form*

The spatial discretization of the composite-moment form is similar to that of the standard form. Starting with Eq. (3.8a), the weak form can be obtained as:

$$\oint_{\partial V} b_i \tilde{\vec{\Phi}}^o \cdot \vec{n} dA - \int_V \vec{\nabla} b_i \tilde{\vec{\Phi}}^o dV + \int_V b_i C^{-T} \Sigma^e C^{-1} \tilde{F} \, dV = \int_V b_i C^{-T} S^e dV, \quad (3.32)$$

The implementation of the Mark boundary conditions is also similar to that for the standard form. The trick is to first find the relationship between $\vec{\Phi}^o$ and $\Phi^e$, then relate $\Phi^e$ to $F$. By substituting from the composite-moment angular intensity

reconstruction:

$$\psi(\underline{\boldsymbol{x}},\mu)=\sum_{n\text{ even}}\frac{2n+1}{2}\alpha_n\phi_n(\underline{\boldsymbol{x}})P_n(\mu)+\sum_{n\text{ odd}}\frac{2n+1}{2}\alpha_n\vec{\phi}_n(\underline{\boldsymbol{x}})\cdot\vec{n}P_n(\mu) \tag{3.33}$$

into the Mark boundary condition Eq. (3.22), we get:

$$O^{cmp}\vec{\Phi}^o\cdot\vec{n}=g'-E^{cmp}\Phi^e \tag{3.34}$$

where

$$\begin{aligned}O^{cmp}_{i,j} &= \frac{4j-1}{2}\alpha_{2j-1}P_{2j-1}(\mu_i)\\ E^{cmp}_{i,j} &= \frac{4j-3}{2}\alpha_{2j-2}P_{2j-2}(\mu_i)\\ g' &= \left[g'_1,g'_2,\ldots,g'_{\frac{N+1}{2}}\right]^T\end{aligned}$$

Then converting $\Phi^e$ to $\digamma$ using the conversion matrix $C$, we obtain the relationship between $\vec{\Phi}^o$ and $\digamma$:

$$O^{cmp}\vec{\Phi}^o\cdot\vec{n}=g'-E^{cmp}C^{-1}\digamma \tag{3.35}$$

Now insert Eq. (3.35) into Eq. (3.32) to eliminate the $\vec{\Phi}^o$ in the surface term and insert Eq. (3.8b) into Eq. (3.32) to eliminate the $\vec{\Phi}^o$ in the interior term, we obtain the final weak form with boundary condition imposed as follows:

$$\begin{aligned}-\oint_{\partial V}b_i\left(O^{cmp}\right)^{-1}E^{cmp}C^{-1}\tilde{\digamma}\,dA-\int_V\vec{\nabla}b_i(\Sigma^o)^{-1}\vec{\nabla}\tilde{\digamma}\,dV+\int_V b_iB^{cmp}\tilde{\digamma}\,dV\\ =\int_V b_iC^{-T}S^e dV+\int_V\vec{\nabla}b_i\cdot(\Sigma^o)^{-1}\vec{S}^o dV-\oint_{\partial V}b_i\left(O^{cmp}\right)^{-1}g'dA.\end{aligned} \tag{3.36}$$

#### *3.2.1.3 Canonical Form*

The finite element spatial discretization of the even-parity equations in the canonical form, Eq. (3.18a), is similar to that of the even-parity equations in the Even-parity $S_N$. The primary unknowns, $\psi_m^+$, are projected onto a first order continuous finite element space as follows:

$$\tilde{\psi}_m^+(\underline{\boldsymbol{x}}) = \sum_{i=0}^{K} \tilde{\psi}_{m,i}^+ b_i(\underline{\boldsymbol{x}}) \tag{3.37}$$

The secondary unknowns, $\vec{\psi}_m^-$, add a new complexity into the discretization. Because anisotropic scattering is allowed in our $SP_N$ equations, we can not avoid dealing with the odd-parity unknowns, and thus the odd-parity equations (Eq. (3.15b)). Based on Eq. (3.15b), we propose to represent the $\vec{\psi}_m^-$ with some spatial derivatives of $\{b_i\}$. This can be done in two different approaches.

The first approach is to treat each component of $\vec{\psi}_m^-$, denoted by $\psi_m^{(-,j)}$ where $j$ can be $x$, $y$, or $z$, as an independent unknown. And for any $j$, $\psi_m^{(-,j)}$ lives in space spanned by $\{\nabla_j b_i\}$, where

$$\nabla_j = \frac{\partial}{\partial j}, \quad j = x, y, z. \tag{3.38}$$

Observing that each $\{\nabla_j b_i\}$ forms a subspace of that spanned by $\{b_i\}$ inside each cell,

$$b_i(x,y,z) = c_1 + c_2 x + c_3 y + c_4 z + c_5 xy + c_6 yz + c_7 xz + c_8 xyz, \tag{3.39}$$

$$\nabla_x b_i(x,y,z) = c_2 + c_5 y + c_7 z + c_8 yz, \tag{3.40}$$

$$\nabla_y b_i(x,y,z) = c_3 + c_5 x + c_6 z + c_8 xz, \tag{3.41}$$

$$\nabla_z b_i(x,y,z) = c_4 + c_6 y + c_7 x + c_8 xy, \tag{3.42}$$

we can still use the tri-linear finite element space as the space for $\{\nabla_j b_i\}$, but it will not be continuous at the cell interfaces. Thus it will require us to virtually use a combination of 4 tri-linear discontinuous finite element spaces to represent the secondary unknown, that is 24 degrees of freedom (DoF) per cell. Even if we customize the finite element space for each component and keep only those non-trivial ones, there will still be 12 DoFs per cell. And it is much more difficult to implement in an existing finite element code package.

Or as a second approach, we can regard the whole vector $\vec{\psi}_m^-$ as a single unknown. And we project it onto a new space spanned by $\left\{\vec{\nabla} b_i\right\}$. This a vector finite element space, thus no longer a subspace of *span* $\{b_i\}$. It is also a discontinuous trial space, in the sense that $\left\{\vec{\nabla} b_i\right\}$ is the gradient of the piece-wise continuous linear space of $\{b_i\}$. However, the extra degrees of freedom at the discontinuities are eliminated because the new space is derived from the known space $\{b_i\}$, rather than blindly allowing for any possible discontinuity scenario. Therefore, it does maintain the same number of DoFs per cell and their support points are at the same location as in the original $\{b_i\}$ space. The secondary unknown can be represented as:

$$\tilde{\vec{\psi}}_m^-(\underline{\boldsymbol{x}}) = \sum_{i=0}^{K} \tilde{\psi}_{m,i}^- \vec{\nabla} b_i(\underline{\boldsymbol{x}}) \tag{3.43}$$

Note that we converted the scalar secondary unknown into a scalar finite element unknown. By following this approach, we actually insured that the spatial discretization of $\psi_m^+$ and $\vec{\psi}_m^-$ is consistent. And the value of $\tilde{\psi}_{m,i}^-$ can be determined by collocating the Eq. (3.15b) at those DoF support points. We can algebraically obtain the value of $\tilde{\psi}_{m,i}^-$ as:

$$\tilde{\psi}_{m,i}^- = -\frac{\mu_m}{\sigma_t} \tilde{\psi}_{m,i}^+ + \frac{\tilde{Q}_{m,i}^-}{\sigma_t} \tag{3.44}$$

where

$$\tilde{Q}^{-}_{m,i} = \sum_{n=1,3,\ldots}^{N} (2n+1)\sigma_{s,n} P_n(\mu_m)\tilde{\phi}_{n,i} + \tilde{S}^{-}_{m,i}. \tag{3.45}$$

In the above expressions for $\tilde{Q}^{-}_{m,i}$, the Legendre angular moments $\tilde{\phi}_{n,i}$ can be computed from $\tilde{\psi}^{-}_{m,i}$ using angular quadrature rule at the DoF points. The external source, $\tilde{S}^{-}_{m,i}$, needs some special treatment. Because $\vec{\psi}^{-}_{m}$ is projected onto $\left\{\vec{\nabla} b_i\right\}$, we have to do the same to the $\vec{S}^{-}_{m}$ in order for the algebraic Eq. (3.44) to be appropriate. The idea is to find a $\tilde{S}^{-}_{m}$ whose gradient is $\vec{S}^{-}_{m}$. Thus:

$$\tilde{S}^{-}_{m,i}\vec{\nabla} b_i = \vec{S}^{-}_{m,i} \tag{3.46}$$

To compute the $\tilde{S}^{-}_{m,i}$, we can integrate the $\vec{S}^{-}_{m}$ along an arbitrary line from an arbitrary reference point. Since Eq. (3.44) is evaluated cell by cell, we can pick a reference point for each cell, for example the vertex with the lowest $x$, $y$, and $z$ coordinate; for the integration line, we choose to first integrate along $x$ direction from the reference point to the point of interest ($\underline{\boldsymbol{x}}_i$), and the along $y$ direction, and then finally the $z$ direction. Quadrature rules are employed to do the numerical line integration, and the same order of quadrature as used in assembling the system matrix (i.e., integrating the product between basis functions) is good enough to not introduce extra numerical error. For instance, in the linear finite element case, second-order accuracy is maintained.

In our code, instead of using Eq. (3.44) directly, we take Legendre moments of it and use the odd moments of the angular intensity ($\tilde{\vec{\phi}}_n$) as our secondary unknown because it is more easily plugged into the Eq. (3.18a) to get the odd parity scattering source.

$$\tilde{\phi}_{n,i} = \frac{1}{\sigma_t} \sum_{m=1}^{N+1} \mu_m \tilde{\psi}^{+}_{m,i} P_n(\mu_m) w_m + \sigma_{s,n}\tilde{\phi}_{n,i} + \tilde{S}_{n,i} \tag{3.47}$$

The $\left\{\vec{\nabla} b_i\right\}$ approach requires constructing $\tilde{S}_{n,i}$ (or $\tilde{S}^{-}_{m,i}$), but it uses virtually a differential hierarchy of the same trial space for both primary and secondary unknowns, making the spatial discretization consistent, and requires less memory to store the DoFs of the secondary unknown (that's 8 versus 12 as the best scenario for the first approach).

The Mark boundary condition implementation follows from that for the Even-parity $S_N$ equations. The weak form of the canonical $SP_N$ can be obtained as:

$$\oint_{\partial V} \mu_m b_i \tilde{\vec{\psi}}^{-}_m \cdot \vec{n} dA - \int_V \mu_m \vec{\nabla} b_i \cdot \tilde{\vec{\psi}}^{-}_m dV + \int_V \sigma_t b_i \tilde{\psi}^{+}_m dV = \int_V b_i Q^{+}_m dV \tag{3.48}$$

Substituting in the Eq. (3.22) to eliminate the $\tilde{\vec{\psi}}^{-}_m$ in the surface term and the Eq. (3.18b) to eliminate the $\tilde{\vec{\psi}}^{-}_m$ in the interior term, we get:

$$\begin{aligned} -\oint_{\partial V} \mu_m b_i \tilde{\psi}^{+}_m dA + \int_V \frac{\mu_m^2}{\sigma_t} \vec{\nabla} \cdot b_i \vec{\nabla} \tilde{\psi}^{+}_m dV + \int_V \sigma_t b_i \tilde{\psi}^{+}_m dV \\ = \int_V b_i Q^{+}_m dV + \int_V \mu_m \vec{\nabla} b_i \cdot \frac{\vec{Q}^{-}_m}{\sigma_t} - \oint_{\partial V} \mu_m b_i g_m dA \end{aligned} \tag{3.49}$$

### *3.2.2 Iterative Schemes*

In this section, we present the iterative techniques commonly employed to solve the various diffusion-like formulations of the $SP_N$ equations. For any given matrix $A$, we introduce its splitting into an strictly upper triangular matrix and a lower triangular matrix as $A = \overline{A} + \underline{A}$. We restrict our consideration to iteration schemes that require only the solution of a set of independent diffusion equations per iteration.

#### *3.2.2.1 Gauss-Seidel Iteration*

In the case of the standard form, the structure of the system matrix (neglecting discretization of the spatial operators) is block-tridiagonal (the diagonal terms

contain a diffusion plus reaction operator while the off-diagonal entries only contain diffusion operators). In the case of the composite moment formulation, the structure of the system matrix is full because matrix $B^{cmp}$ is full (the diagonal terms containing a diffusion plus reaction operator while the off-diagonal entries only contain a reaction operator). For both of these forms, a standard procedure for solving the system is Gauss-Seidel iteration (also called FLIP by Gelbard [7]). For the standard form, Gauss-Seidel iteration can be expressed as follows,

$$-\vec{\nabla}\cdot(\underline{K}^{std})\vec{\nabla}\Phi^{e,(\ell+1)}+\Sigma^{e}\Phi^{e,(\ell+1)}=\vec{\nabla}\cdot(\overline{K}^{std})\vec{\nabla}\Phi^{e,(\ell)}+S^{e}-\vec{\nabla}\cdot\Big(C^{std}(\Sigma^{o})^{-1}\vec{S}^{o}\Big)\,, \quad (3.50)$$

and for the composite form,

$$-\vec{\nabla}\cdot(\Sigma^{o})^{-1}\vec{\nabla}\boldsymbol{F}^{(\ell+1)}+\underline{B}^{cmp}\boldsymbol{F}^{(\ell+1)}=-\overline{B}^{cmp}\boldsymbol{F}^{(\ell)}+C^{-T}S^{e}-\vec{\nabla}\cdot(\Sigma^{o})^{-1}\vec{S}^{o}, \quad (3.51)$$

where the superscript $\ell$ denotes the iteration index.

#### *3.2.2.2 EXPLICIT Iteration*

In [3], Brantley and Larsen proposed, for the composite form of the $SP_3$ equations, a modified Gauss-Seidel iteration, which they coined the "EXPLICIT" scheme. The idea behind the $SP_3$ "EXPLICIT" scheme is to be able to rapidly capture the infinite medium solution, $\phi_0 \simeq S_0/\sigma_0$. Indeed, if the problem has an isotropic external source and contains large optically thick regions, the higher order moments will vanish in these regions and the angular integrated intensity will approach a value of $S_0/\sigma_0$. Brantley and Larsen therefore proposed to modify the Gauss-Seidel (FLIP) procedure as follows for the $SP_3$ equations

$$-\vec{\nabla}\cdot\frac{1}{\sigma_1}\vec{\nabla}\boldsymbol{F}_{1}^{(\ell+1)}+\sigma_0\boldsymbol{F}_{1}^{(\ell+1)}=\sigma_0\boldsymbol{F}_{2}^{(\ell)}+S_0 \quad (3.52a)$$

$$-\vec{\nabla}\cdot\frac{1}{\sigma_3}\vec{\nabla}F_2^{(\ell+1)} + \sigma_2 F_2^{(\ell+1)} = \sigma_0\left(F_1^{(\ell+1)} - F_2^{(\ell)}\right) - S_0. \tag{3.52b}$$

Recalling from Eq. (3.11) that $\phi_0 = F_1 - F_2$, we note that Eq. (3.52a) will yield, in optically thick regions far away from boundaries and interfaces,

$$\sigma_0 F_1^{(\ell+1)} - \sigma_0 F_2^{(\ell)} - S_0 \simeq 0, \tag{3.53}$$

which is indeed the iterative equivalent of $\phi_0 = F_1 - F_2 \simeq S_0/\sigma_0$. The "EXPLICIT" scheme is characterized by lagging part of the $F_2$ reaction term so as to obtain the left side of Eq. (3.53) on the right side of Eq. (3.52b). The resulting smallness of the right side of Eq. (3.52b) implies that $F_2^{(\ell+1)} = \phi_2^{(\ell+1)} \approx 0$, which is consistent with the infinite-medium solution.

The "EXPLICIT" idea can be generalized for any order $N$ of the $SP_N$ equations as follows. Assuming (a) an isotropic external source and (b) a solution that approaches the infinite medium solution, $\phi_0 \simeq S_0/\sigma_0$ and $\phi_{n>0} = 0$, then the first of the $M$ equations in the $SP_N$ composite form yields

$$\sigma_0 F_1^{(\ell+1)} = \sigma_0 \sum_{i=2}^{M} (-1)^i F_i^{(\ell)} + S_0. \tag{3.54}$$

Using Eq. (3.11), we note that Eq. (3.54) is simply an iterative form for $\sigma_0\phi_0 = S_0$. where

$$\phi_0 = F_1^{(\ell+1)} + \sum_{i=2}^{M} (-1)^{i-1} F_i^{(\ell)}. \tag{3.55}$$

The iterative expression, Eq. (3.55), is then used for all the $\phi_0$'s appearing in remaining $M-1$ equations, in order to minimize the $\sigma_0\phi_0 - S_0$ term that shows up in every one of them. To illustrate the "EXPLICIT" scheme in matrix form, we first introduce a auxiliary matrix ($O$) that dictates which terms should be lagged in order

to preserve the $\phi_0$ after solving the $\mathbf{F}_1$ equation.

$$O = \begin{bmatrix} 0 & -\sigma_0 & \sigma_0 & -\sigma_0 & \cdots & (-1)^N\sigma_0 \\ 0 & \sigma_0 & -\sigma_0 & \sigma_0 & \cdots & (-1)^{(1+N)}\sigma_0 \\ \vdots & \vdots & \vdots & \vdots & \ddots & \vdots \\ 0 & (-1)^{(N+1)}\sigma_0 & \cdots & \cdots & \cdots & (-1)^{(N+N)}\sigma_0 \end{bmatrix} \tag{3.56}$$

Finally, the splitting of $B^{cmp}$ is as follows

$$B_1^{cmp} = \underline{B^{cmp}} - \underline{O}, \tag{3.57}$$

$$B_2^{cmp} = \overline{B^{cmp}} + \underline{O}, \tag{3.58}$$

and the generalization of the "EXPLICIT" scheme to any order of $SP_N$ approximation is

$$-\vec{\nabla}\cdot(\Sigma^o)^{-1}\vec{\nabla}\mathbf{F}^{(\ell+1)} + B_1^{cmp}\mathbf{F}^{(\ell+1)} = -B_2^{cmp}\mathbf{F}^{(\ell)} + C^{-T}S^e - \vec{\nabla}\cdot(\Sigma^o)^{-1}\vec{S}^o. \tag{3.59}$$

#### *3.2.2.3 Source Iteration*

Due to the similarity between the canonical $SP_N$ equations and the 1-D Even-parity $S_N$, all of the iterative methods we previously reviewed for the 1-D Even-parity $S_N$ equations apply with identical effect to the multidimensional canonical $SP_N$ equations, notably source iteration (SI) and SI preconditioned with diffusion synthetic acceleration (SI+DSA). We give the expressions for the SI iterative equations here and will discuss the acceleration schemes in the following section (Section 3.2.3).

SI for the canonical form can be illustrated as follows ( for $m = 1, \ldots, M$):

$$-\mu_m^2\vec{\nabla}\cdot\frac{1}{\sigma_t}\vec{\nabla}\psi_m^{+,(\ell+1)} + \sigma_t\psi_m^{+,(\ell+1)} = Q_m^{+,(\ell)} - \mu_m\vec{\nabla}\cdot\left(\frac{Q_m^{-,(\ell)}}{\sigma_t}\right), \tag{3.60a}$$

$$\psi_m^{-,(\ell+1)} = -\frac{\mu_m}{\sigma_t}\vec{\nabla}\psi_m^{+,(\ell+1)} + \frac{1}{\sigma_t}Q_m^{-,(\ell)}. \tag{3.60b}$$

For the purpose of the subsequent Fourier analysis, we recast the SI process in matrix notation:

$$\begin{bmatrix} -\vec{\nabla}\cdot K^{can}\vec{\nabla} + \sigma_t & 0 \\ \frac{W}{\sigma_t}\vec{\nabla} & I \end{bmatrix} \begin{bmatrix} \Psi^+ \\ \vec{\Psi}^- \end{bmatrix}^{(\ell+1)} = \begin{bmatrix} H^+ & -W\vec{\nabla}\cdot\frac{H^-}{\sigma_t} \\ 0 & \frac{H^-}{\sigma_t} \end{bmatrix} \begin{bmatrix} \Psi^+ \\ \vec{\Psi}^- \end{bmatrix}^{(\ell)} + \begin{bmatrix} S^+ - W\vec{\nabla}\cdot\frac{\vec{S}^-}{\sigma_t} \\ \frac{\vec{S}^-}{\sigma_t} \end{bmatrix}, \tag{3.61}$$

or, more concisely,

$$\mathcal{K}\boldsymbol{\Psi}^{(\ell+1)} = \mathcal{S}\boldsymbol{\Psi}^{(\ell)} + \mathcal{Q}. \tag{3.62}$$

where

$$\boldsymbol{\Psi}^{(\ell+1/2)} = [\psi_1^+, \ldots, \psi_M^+, \vec{\psi}_1^-, \ldots, \vec{\psi}_M^-]^T \tag{3.63}$$

It is easy to note that Eq. (3.21) is recovered from Eq. (3.61) by dropping the iteration index and eliminating the odd-parity flux.

### *3.2.3 Acceleration Methods*

The iterative acceleration schemes presented here are intended for only the canonical form of the $SP_N$ equations. As noted before, DSA can be directly borrowed from the solution of the Even-parity $S_N$ equations as discussed in Section 2.3.2.2. However, DSA is only effective when scattering is largely isotropic. And because we are allowing anisotropic scattering in the canonical Even-parity $S_N$ equations, we will also apply $P_1$ synthetic acceleration ($P_1$SA) and angular multi-grid acceleration (AnMG) as supplements. It has to be pointed out that the latter two methods are also extended from the $S_N$ equations solution technique where anisotropic scattering is present.

#### *3.2.3.1 DSA and $P_1$SA*

For ease of discussion and subsequent Fourier analysis, we cast the DSA for canonical $SP_N$ in matrix form. First, solve the Eq. (3.62) for $\mathbf{\Psi}^{(\ell+1/2)}$:

$$\mathbf{\Psi}^{(\ell+1/2)} = \mathcal{K}^{-1}(\mathcal{S}\mathbf{\Psi}^{(\ell)} + \mathcal{Q}) \tag{3.64}$$

Then use the full discrete-to-moment matrix, $\mathcal{D} = diag(D^+, D^-)$ to obtain the moments vector $\mathbf{\Phi}^{(\ell+1/2)} = [\phi_0^+, \phi_2^+, \ldots, \phi_{N-1}^+, \vec{\phi}_1^-, \vec{\phi}_3^-, \ldots, \vec{\phi}_N^-]^T$:

$$\mathbf{\Phi}^{(\ell+1/2)} = \mathcal{D}\mathbf{\Psi}^{(\ell+1/2)}, \tag{3.65}$$

Next solve the diffusion equation for the correction on $\phi_0^{(\ell+1/2)}$:

$$\delta\phi_0^{(\ell+1/2)} = \mathcal{T}_0^{-1} R_{N\to 0}\Sigma(\mathbf{\Phi}^{(\ell+1/2)} - \mathbf{\Phi}^{(\ell)}), \tag{3.66}$$

And finally the next iterate for the angular moments:

$$\mathbf{\Phi}^{(\ell+1)} = \mathbf{\Phi}^{(\ell+1/2)} + P_{0\to N}\delta\phi_0^{(\ell+1/2)}, \tag{3.67}$$

where $\mathcal{T}_0$ is the DSA operator ($\mathcal{T}_0 = -\vec{\nabla}\cdot\frac{1}{3\sigma_a}\vec{\nabla} + \sigma_t$), $\Sigma = diag(\Sigma^+, \Sigma^-)$ is the full even/odd scattering matrix, $R_{N\to 0}$ is the restriction matrix of $\boldsymbol{\phi}$ (all moments) to the angular integrated intensity $\phi_0$, and $P_{0\to N}$ is the projection matrix of $\phi_0$ back to $\boldsymbol{\phi}$.

Recall that in DSA we assumed isotropic scattering. If we account for the $P_1$ anisotropic scattering when deriving the diffusion correction equations, we get the $P_1$ synthetic acceleration ($P_1$SA) scheme, which include correction to both the $P_0$

and $P_1$ moments. This requires us to replace Eq. (3.66) with:

$$\delta\phi_0^{(\ell+1/2)} = \mathcal{T}_{0^*}^{-1}\left[R_{N\to 0}\Sigma - R_{N\to 1}\vec{\nabla}\frac{\Sigma}{\sigma_t I - \Sigma}\right](\mathbf{\Phi}^{(\ell+1/2)} - \mathbf{\Phi}^{(\ell)}), \tag{3.68a}$$

$$\delta\vec{\phi}_1^{(\ell+1/2)} = -\frac{1}{3(\sigma_t - \sigma_0)}\vec{\nabla}\delta\phi_0^{(\ell+1/2)} + R_{N\to 1}\frac{\Sigma}{\sigma_t I - \Sigma}(\mathbf{\Phi}^{(\ell+1/2)} - \mathbf{\Phi}^{(\ell)}). \tag{3.68b}$$

where $\mathcal{T}_{0^*} = -\vec{\nabla}\cdot\frac{1}{3(\sigma_t - \sigma_{s,1})}\vec{\nabla} + \sigma_a$. And Eq. (3.67) is replaced by:

$$\mathbf{\Phi}^{(\ell+1)} = \mathbf{\Phi}^{(\ell+1/2)} + P_{0\to N}\delta\phi_0^{(\ell+1/2)} + P_{1\to N}\delta\vec{\phi}_1^{(\ell+1/2)}. \tag{3.69}$$

The $P_1$SA is more effective than the DSA when the scattering is moderately anisotropic. And because Eq. (3.68b) does not require inverting any operator, the $P_1$SA does not incur significant extra computational cost compared to the standard DSA. For this reason, we will use the $P_1$SA in place of DSA in further analyses.

#### *3.2.3.2 Angular Multigrid*

In the highly forward-peaked scattering limit, it is well known that both DSA and $P_1$SA become ineffective. In response to this deficiency, Morel and Manteuffel [15] developed an angular multigrid method for the 1-D $S_N$ equations. This method is quite efficient, costing roughly twice as much as DSA per source iteration, and yields a maximum spectral radius of approximately 0.6 in the Fokker-Planck limit. Morel and Manteuffel's angular multigrid method uses a variation of the extended transport correction [11] to attenuate the "upper half" of the angular moments (higher frequencies) via transport sweeps. The "lower half" of the angular moments (lower frequencies) is accelerated using the $S_{N/2}$ equations. These $S_{N/2}$ equations are themselves accelerated using $S_{N/4}$ equations. The order of the transport operator is divided by two until the $S_4$ level, at which point, the $P_1$ equations are used to accelerate the $S_4$

equations.

Due to the analogy between the canonical $SP_N$ equations ($N$ odd) and the $S_{N+1}$ equations, the angular multigrid method is easily extended to apply to the 3-D $SP_N$ equations. Adapting from Morel and Manteufel, we define:

$$Half(N) = \begin{cases} \dfrac{N-1}{2}, & \text{if } \dfrac{N+1}{2} \text{ is even,} \\ \dfrac{N+1}{2}, & \text{if } \dfrac{N+1}{2} \text{ is odd} \end{cases} \tag{3.70}$$

Using this definition of "*Half*" to coarsen the "angular" grid, the sequence of $SP_N$ solves for an $SP_{15}$ base level is ($SP_{15} - SP_7 - SP_3-$diffusion) and, for a $SP_{13}$ base level, ($SP_{13} - SP_7 - SP_3-$diffusion). Every time a transport sweep is performed, the optimal transport correction needs to be used [15]. This correction is said to be optimal because it minimizes the "high-frequency" angular errors. For a $P_N$ expansion of the cross sections, the corrected cross sections are given by :

$$\sigma_j^* = \sigma_j - \frac{\sigma_{s,Half(N)} + \sigma_{s,N}}{2} \quad \text{with } j = \{t\} \text{ or } \{s,n\} \tag{3.71}$$

To demonstrate the AnMG process, we give the equations for AnMG applied to the

$SP_{15}$ equations:

$$\mathcal{K}_{15}\boldsymbol{\Psi}_{15}^{(\ell+1/2)} = \mathcal{S}_{15}\boldsymbol{\Psi}_{15}^{(\ell)} + \mathcal{Q}, \tag{3.72a}$$

$$\boldsymbol{\Phi}_{15}^{(\ell+1/2)} = \mathcal{D}_{15}\boldsymbol{\Psi}_{15}^{(\ell+1/2)}, \tag{3.72b}$$

$$\mathcal{K}_{7}\delta\boldsymbol{\Psi}_{7}^{(\ell+1/2)} = \mathcal{S}_{7}\mathcal{D}_{7}^{-1}R_{15\to 7}(\boldsymbol{\Phi}_{15}^{(\ell+1/2)} - \boldsymbol{\Phi}_{15}^{(\ell)}), \tag{3.72c}$$

$$\delta\boldsymbol{\Phi}_{7}^{(\ell+1/2)} = \mathcal{D}_{7}\delta\boldsymbol{\Psi}_{7}^{(\ell+1/2)}, \tag{3.72d}$$

$$\mathcal{K}_{3}\delta\boldsymbol{\Psi}_{3}^{(\ell+1/2)} = \mathcal{S}_{3}\mathcal{D}_{3}^{-1}R_{7\to 3}\delta\boldsymbol{\Phi}_{7}^{(\ell+1/2)}, \tag{3.72e}$$

$$\delta\boldsymbol{\Phi}_{3}^{(\ell+1/2)} = \mathcal{D}_{3}\delta\boldsymbol{\Psi}_{3}^{(\ell+1/2)}, \tag{3.72f}$$

$$\delta\boldsymbol{\Phi}_{1}^{(\ell+1/2)} = \mathcal{T}_{1}^{-1}R_{3\to 1}\delta\boldsymbol{\Phi}_{3}^{(\ell+1/2)}, \tag{3.72g}$$

$$\boldsymbol{\Phi}_{15}^{(\ell+1)} = \boldsymbol{\Phi}_{15}^{(\ell+1/2)} + P_{7\to 15}\delta\boldsymbol{\Phi}_{7}^{(\ell+1/2)} + P_{3\to 15}\delta\boldsymbol{\Phi}_{3}^{(\ell+1/2)} + P_{1\to 15}\delta\boldsymbol{\Phi}_{1}^{(\ell+1/2)}, \tag{3.72h}$$

where the $\mathcal{T}_1$ is the $P_1$SA operator representing Eq. (3.68). For additional details on the angular multigrid, we refer the reader to [15, 19].

## 3.3 Iterative Performance Comparison between Various $SP_N$ Forms

To compare the convergence rates of the different $SP_N$ formulations and corresponding iteration schemes, Fourier analyses are carried out for two different scattering scenarios: isotropic scattering and Fokker-Planck scattering; the definitions of the scattering cross sections are given below. 1-D finite element codes have also been developed and used to confirm the Fourier analyses results.

### *3.3.1 Scattering Laws*

The various iterative schemes for the $SP_N$ equations are tested with both isotropic scattering and Fokker-Planck scattering. For isotropic scattering, only the zero-th Legendre moment of the scattering cross section, $\sigma_{s,0}$, is non-zero. Fokker-Planck (FP) scattering is employed as a representative form for highly forward-peaked scat-

tering. Fokker-Planck scattering represents an asymptotic limit in which the average cosine of the scattering angle approaches 1 while the scattering cross section increases without bound but in such a way that the momentum transfer or transport-corrected scattering cross section remains fixed at an arbitrary value of $\alpha$. The moments of its scattering cross section depend upon the order of the Legendre expansion. In particular, for an expansion of degree $N$, the cross-section expansion coefficients can be expressed as follows:

$$\sigma_{s,k} = \frac{\alpha}{2}\left[N(N+1) - k(k+1)\right], \quad k = 0, \ldots, N. \tag{3.73}$$

The dependence of the expansion coefficients upon the degree of the expansion is a mathematical rather than a physical property that arises from the fact that the Fokker-Planck scattering limit involves an unbounded physical cross section. The expansion coefficients defined above are not unique. However, the total attenuation coefficients (or the eigenvalues of the Fokker-Planck scattering operator) are unique:

$$\sigma_{s,0} - \sigma_{s,k} = \frac{\alpha}{2}k(k+1), \quad k = 0, \ldots, \infty. \tag{3.74}$$

### *3.3.2 Fourier Analyses*

Fourier analyses are carried out to evaluate the convergence rates of the iteration schemes proposed for the different $SP_N$ forms. The iteration error is decomposed into a continuum of Fourier modes $e^{i\vec{\Lambda}\cdot\vec{r}}$ (where $\vec{\Lambda} = [\lambda_x, \lambda_y, \lambda_z]^T$, and with $\lambda_{x,y,z} \in (-\infty, +\infty)$) whose error amplitude coefficients depends upon $\vec{\Lambda}$. Therefore, all spatial derivatives appearing in the $SP_N$ forms are replaced with the following: $i\vec{\Lambda}\cdot \leftarrow \vec{\nabla}\cdot$ and $i\vec{\Lambda} \leftarrow \vec{\nabla}$, where $i^2 = -1$. Since the Fourier modes are eigenfunctions of spatial differential operators, this process results in a linear system relating the

iteration error at $\ell+1$, denoted next by $\mathcal{E}_{\vec{\Lambda}}^{(\ell+1)}$, to the previous iteration error, $\mathcal{E}_{\vec{\Lambda}}^{(\ell)}$, and is written in general as follows:

$$\mathcal{A}(\vec{\Lambda})\mathcal{E}_{\vec{\Lambda}}^{(\ell+1)} = \mathcal{B}(\vec{\Lambda})\mathcal{E}_{\vec{\Lambda}}^{(\ell)}. \tag{3.75}$$

Table 3.1 provides the definitions of the iteration matrices for the various $SP_N$ forms analyzed here. Additional details regarding these Fourier analyses are provided in Appendix B, where we show that the eigenvalues of the iteration matrix, $[\mathcal{A}(\vec{\Lambda})]^{-1}\mathcal{B}(\vec{\Lambda})$, only depend on $\lambda^2 = \|\vec{\Lambda}\|^2 = \lambda_x^2 + \lambda_y^2 + \lambda_z^2$, the squared norm of the wave number. Thus, the analyses need only to be carried out for $\lambda^2 \in [0, \infty)$, regardless of the spatial dimension of the problem at hand.

| $SP_N$ form | $\mathcal{A}$ | $\mathcal{B}$ |
|---|---|---|
| Standard (GS) (see Eq. (3.50)) | $\lambda^2\underline{K^{std}} + \Sigma^e$ | $-\lambda^2\overline{(K^{std})}$ |
| Composite (GS) (see Eq. (3.51)) | $\lambda^2(\Sigma^o)^{-1} + \underline{B^{cmp}}$ | $-\overline{B^{cmp}}$ |
| Composite (EX) (see Eq. (3.59)) | $\lambda^2(\Sigma^o)^{-1} + B_1^{cmp}$ | $-B_2^{cmp}$ |
| Canonical (see Eq. (3.61)) | $\mathcal{K}_{\vec{\Lambda}}$ | $\mathcal{S}_{\vec{\Lambda}}$ |

Table 3.1: Iteration matrices for the various $SP_N$ forms (GS=Gauss-Seidel, EX="Explicit")

where

$$\mathcal{K}_{\vec{\Lambda}} = \begin{bmatrix} \lambda^2 K^{can} + \sigma_t & 0 \\ \frac{W}{\sigma_t}\vec{\Lambda} & I \end{bmatrix}, \quad \mathcal{S}_{\vec{\Lambda}} = \begin{bmatrix} H^+ & -iW\vec{\Lambda}\cdot\frac{H^-}{\sigma_t} \\ 0 & \frac{H^-}{\sigma_t} \end{bmatrix} \tag{3.76}$$

Define

$$\mathcal{M} = \mathcal{K}_{\vec{\Lambda}}^{-1}\mathcal{S}_{\vec{\Lambda}}, \tag{3.77}$$

Then the $\mathcal{A}^{-1}\mathcal{B}$ matrices for the canonical form solved with SI+DSA and SI+$P_1$SA are give as follows:

1. SI+DSA

$$\mathcal{A}^{-1}\mathcal{B} = \mathcal{D}^{-1}\left[\mathcal{D}\mathcal{M} + P_{0\to N}\mathcal{T}_0^{-1}R_{N\to 0}\Sigma\mathcal{D}(\mathcal{M}-I)\right] \tag{3.78}$$

2. SI+$P_1$SA

$$\begin{aligned}\mathcal{A}^{-1}\mathcal{B} &= \mathcal{M} \\ +\mathcal{D}^{-1}&\left[P_{0\to N} - P_{1\to N}\frac{1}{3(\sigma_t-\sigma_0)}i\vec{\Lambda}\right]\mathcal{T}_{0^*}^{-1}\left(R_{N\to 0}\Sigma - R_{N\to 1}i\vec{\Lambda}\frac{\Sigma}{\sigma_t I-\Sigma}\right)\mathcal{D}(\mathcal{M}-I) \\ &+\mathcal{D}^{-1}P_{1\to N}R_{N\to 1}\frac{\Sigma}{\sigma_t I-\Sigma}\mathcal{D}(\mathcal{M}-I)\end{aligned} \tag{3.79}$$

The $\mathcal{A}^{-1}\mathcal{B}$ for the SI+AnMG can be obtained in a similar approach. However since it involves a hierarchy of acceleration processes that depends on the order of $SP_N$, its Fourier analysis matrix can be only formulated in a recursive manner. The expression will be too lengthy to be presented here but it is not difficult to obtain by following the logic manifested in Eqs.(3.72).

The largest eigenvalue of the iteration matrix $\mathcal{A}^{-1}\mathcal{B}$, for any value of $\lambda$, is then the spectral radius of the iterative method. A simple routine was written to compute the eigenvalues $\mathcal{A}^{-1}\mathcal{B}$ for a homogeneous infinite domain (limiting the search for values of $\lambda$ in $[0,\infty)$).

### *3.3.3 1-D Finite Element Code Verification*

The $SP_N$ forms and their iterative schemes have been implemented in 1-D continuous finite element codes for numerical verification of the spectral radii obtained with the Fourier analysis. These Fourier analyses do not account for boundary conditions because the assumed medium is infinite in extent. One expects to be able to computationally reproduce the Fourier analysis results in the limit as the optical thickness of the medium increases without bound. To simulate an infinite medium

configuration, we equip the computational domain with reflective boundary conditions.

The scattering ratio is varied from 0 to 1. However, when $c = 1$, there are no particle loss mechanism for problems with reflective boundaries and iterative schemes do not converge, as expected. Thus, for purely scattering tests, vacuum boundary conditions and zero volumetric sources are employed, and a random initial guess is chosen (the exact solution for such configurations is a uniformly 0 and one can drive the convergence criteria of the iterative schemes close to machine round-off). We also choose to employ an optical thickness of 100 mean-free-paths (mfp) and spatial grid resolutions that adequately approximate an infinite medium, as judged by the agreement between analysis and computation.

Tabulated in Tables 3.2–3.10 are some spectral radius results for $SP_3$, $SP_7$, and $SP_{15}$ calculations. The scattering ratios used are $c = 0$, 0.5, and 1.0. In these Tables, the following abbreviations are employed: **ISO** for isotropic scattering, **F.P.** for Fokker-Planck scattering, **F.A.** for Fourier analysis results, **Disc.** for spatially discretized numerical results, $\mathbf{P_1SA}$ for $P_1$ synthetic acceleration, and **AnMG** for angular multigrid method. These results show a very good agreement between the Fourier analyses and the numerical computations. Additional comments are provided below:

- the spectral radius of the standard form solved with both Gauss-Seidel and explicit scheme increases towards 1 from below as $N$ increases; as $c$ increases, the spectral radius of the scheme remains unaltered in the case of isotropic scattering, and increases for FP scattering;

- the spectral radius of the composite form solved with Gauss-Seidel decreases as $c$ increases (in the pure scattering case, i.e., $c = 1$, the composite $SP_3$ scheme

even has a spectral radius of 0). The higher the $SP_N$ order, the larger the spectral radius, but the spectral radius remains bounded by 1 from below;

- The "EXPLICIT" iterative technique presents a smaller spectral radius than the Gauss-Seidel scheme for the composite form for low values of $N$ (as noted by Brantley and Larsen for $SP_3$, [3]). But for all $N$'s, as $c$ increases, the "EXPLICIT" scheme spectral radii converge to the Gauss-Seidel results.

- iterative properties of the canonical form follow that of 1D $S_{N+1}$ schemes, namely: (1) SI+DSA is effective for isotropic scattering (the spectral radius tends towards the well known value of $0.2247c$ as $N$ increases); (2) SI+DSA is increasingly ineffective for highly anisotropic scattering as $c$ reaches 1; (3) the spectral radius of the SI+AnMG scheme behaves as $(3N-6)/(5N-2)$ for $c = 1$ (as expected, see [15]);

- for vacuum boundary configurations (i.e., when $c = 1$ in our tests), the effect of the moment coupling due to boundary conditions is noticeable for the $SP_3$ composite form (the infinite medium Fourier analysis predicts a spectral radius of 0; the numerical simulations with an optically thick medium placed in a vacuum yield a spectral radius of $\approx 0.05$).

| $c = 0.0$ | | **ISO** | | **F.P.** | |
|---|---|---|---|---|---|
| $SP_3$ | | **F.A.** | **Disc.** | **F.A.** | **Disc.** |
| **Standard** | G-S | 0.50907 | 0.50639 | 0.50907 | 0.50646 |
| **Composite** | G-S | 0.44444 | 0.44444 | 0.44444 | 0.44444 |
| | EXPLICIT | 0.22675 | 0.22569 | 0.22675 | 0.22559 |
| **Canonical** | SI+DSA | 0.00000 | 0.00000 | 0.00000 | 0.00000 |
| | SI +AnMG | 0.00000 | 0.00000 | 0.00000 | 0.00000 |

Table 3.2: Spectral radii for $c = 0.0$, $SP_3$ calculation

| $c = 0.0$ | | **ISO** | | **F.P.** | |
|---|---|---|---|---|---|
| $SP_7$ | | **F.A.** | **Disc.** | **F.A.** | **Disc.** |
| **Standard** | G-S | 0.85641 | 0.85218 | 0.85641 | 0.85160 |
| **Composite** | G-S | 0.73469 | 0.73438 | 0.73469 | 0.73441 |
| | EXPLICIT | 0.66460 | 0.66399 | 0.66460 | 0.66397 |
| **Canonical** | SI +DSA | 0.00000 | 0.00000 | 0.00000 | 0.00000 |
| | SI +AnMG | 0.00000 | 0.00000 | 0.00000 | 0.00000 |

Table 3.3: Spectral radii for $c = 0.0$, $SP_7$ calculation

| $c = 0.0$ | | **ISO** | | **F.P.** | |
|---|---|---|---|---|---|
| $SP_{15}$ | | **F.A.** | **Disc.** | **F.A.** | **Disc.** |
| **Standard** | G-S | 0.96241 | 0.95761 | 0.96241 | 0.95720 |
| **Composite** | G-S | 0.87111 | 0.87157 | 0.87111 | 0.87159 |
| | EXPLICIT | 0.85658 | 0.85641 | 0.85658 | 0.85652 |
| **Canonical** | SI +DSA | 0.00000 | 0.00000 | 0.00000 | 0.00000 |
| | SI +AnMG | 0.00000 | 0.00000 | 0.00000 | 0.00000 |

Table 3.4: Spectral radii for $c = 0.0$, $SP_{15}$ calculation

| $c = 0.5$ | | **ISO** | | **F.P.** | |
|---|---|---|---|---|---|
| $SP_3$ | | **F.A.** | **Disc.** | **F.A.** | **Disc.** |
| **Standard** | G-S | 0.50908 | 0.50700 | 0.63999 | 0.63794 |
| **Composite** | G-S | 0.28571 | 0.28546 | 0.34783 | 0.34745 |
| | EXPLICIT | 0.15221 | 0.15135 | 0.22915 | 0.22191 |
| **Canonical** | SI +DSA | 0.06896 | 0.06897 | 0.14285 | 0.14270 |
| | SI +AnMG | 0.06896 | 0.06907 | 0.14285 | 0.14299 |

Table 3.5: Spectral radii for $c = 0.5$, $SP_3$ calculation

| $c = 0.5$ | | **ISO** | | **F.P.** | |
|---|---|---|---|---|---|
| $SP_7$ | | **F.A.** | **Disc.** | **F.A.** | **Disc.** |
| **Standard** | G-S | 0.85642 | 0.85251 | 0.89833 | 0.89632 |
| **Composite** | G-S | 0.70374 | 0.70345 | 0.64865 | 0.64838 |
| | EXPLICIT | 0.66460 | 0.66405 | 0.59647 | 0.58225 |
| **Canonical** | SI +DSA | 0.09280 | 0.09259 | 0.28725 | 0.28688 |
| | SI +AnMG | 0.04331 | 0.04313 | 0.19149 | 0.19141 |

Table 3.6: Spectral radii for $c = 0.5$, $SP_7$ calculation

| $c = 0.5$ | | **ISO** | | **F.P.** | |
|---|---|---|---|---|---|
| $SP_{15}$ | | **F.A.** | **Disc.** | **F.A.** | **Disc.** |
| **Standard** | G-S | 0.96241 | 0.95839 | 0.97314 | 0.97063 |
| **Composite** | G-S | 0.86424 | 0.86440 | 0.81837 | 0.81978 |
| | EXPLICIT | 0.85658 | 0.85644 | 0.80812 | 0.80362 |
| **Canonical** | SI +DSA | 0.09565 | 0.09554 | 0.32204 | 0.32171 |
| | SI +AnMG | 0.02122 | 0.02116 | 0.21212 | 0.21197 |

Table 3.7: Spectral radii for $c = 0.5$, $SP_{15}$ calculation

| $c = 1.0$ | | **ISO** | | **F.P.** | |
|---|---|---|---|---|---|
| $SP_3$ | | **F.A.** | **Disc.** | **F.A.** | **Disc.** |
| **Standard** | G-S | 0.50908 | 0.50767 | 0.86154 | 0.86065 |
| **Composite** | G-S | 0.00000 | 0.05074 | 0.00000 | 0.03846 |
| | EXPLICIT | 0.00000 | 0.05074 | 0.00000 | 0.03846 |
| **Canonical** | SI +DSA | 0.18484 | 0.18434 | 0.40759 | 0.40651 |
| | SI +AnMG | 0.18484 | 0.18460 | 0.40759 | 0.40707 |

Table 3.8: Spectral radii for $c = 1.0$, $SP_3$ calculation

| $c = 1.0$ | | **ISO** | | **F.P.** | |
|---|---|---|---|---|---|
| $SP_7$ | | **F.A.** | **Disc.** | **F.A.** | **Disc.** |
| **Standard** | G-S | 0.85642 | 0.85323 | 0.98361 | 0.98261 |
| **Composite** | G-S | 0.66460 | 0.66432 | 0.38095 | 0.38089 |
| | EXPLICIT | 0.66460 | 0.66401 | 0.38093 | 0.38067 |
| **Canonical** | SI +DSA | 0.22223 | 0.22151 | 0.80587 | 0.80415 |
| | SI +AnMG | 0.13581 | 0.13603 | 0.48005 | 0.47332 |

Table 3.9: Spectral radii for $c = 1.0$, $SP_7$ calculation

| $c = 1.0$ | | **ISO** | | **F.P.** | |
|---|---|---|---|---|---|
| $SP_{15}$ | | **F.A.** | **Disc.** | **F.A.** | **Disc.** |
| **Standard** | G-S | 0.96241 | 0.95809 | 0.99797 | 0.99766 |
| **Composite** | G-S | 0.85658 | 0.85652 | 0.65882 | 0.65876 |
| | EXPLICIT | 0.85658 | 0.85649 | 0.65881 | 0.65877 |
| **Canonical** | SI +DSA | 0.22465 | 0.22378 | 0.94947 | 0.94890 |
| | SI +AnMG | 0.08807 | 0.09066 | 0.53846 | 0.53779 |

Table 3.10: Spectral radii for $c = 1.0$, $SP_{15}$ calculation

For convenience, the spectral radii ($\rho$) obtained with various schemes are graphed as a function of the scattering ratio $c$ in Fig. 3.1–3.5 for $SP_3$ and $SP_{15}$.

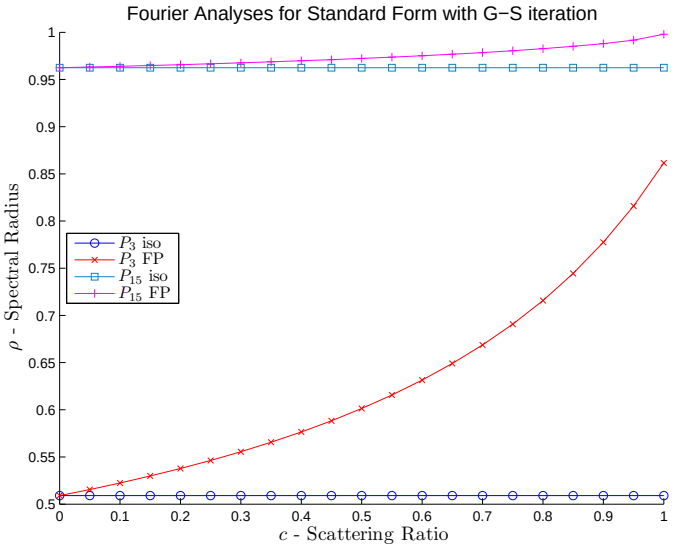


Figure 3.1: Standard form with G-S iteration

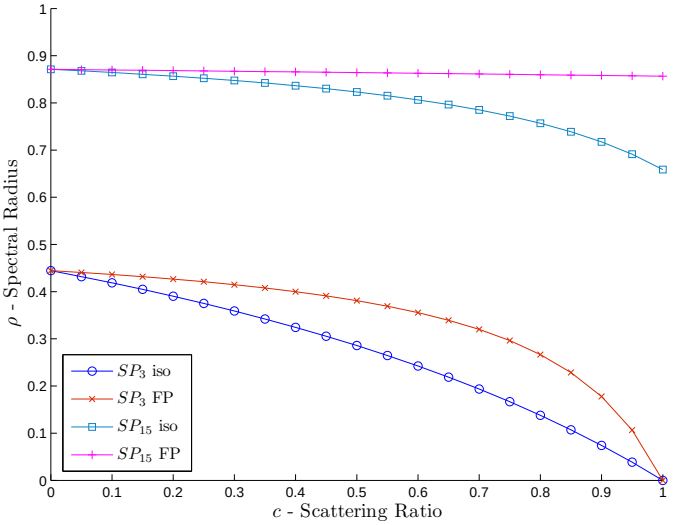


Figure 3.2: Composite form with G-S iteration

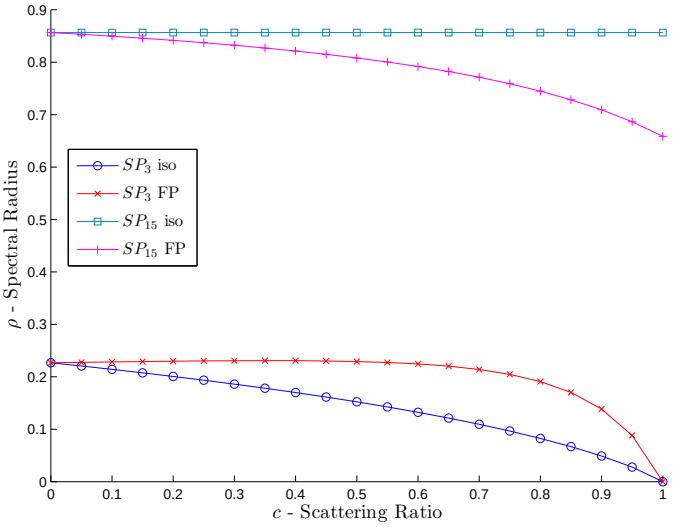


Figure 3.3: Composite form with EXPLICIT iteration

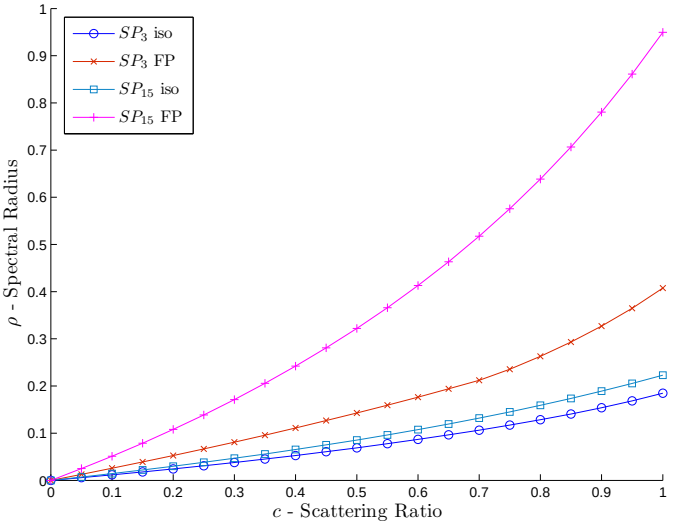


Figure 3.4: Canonical form with SI and $P_1SA$

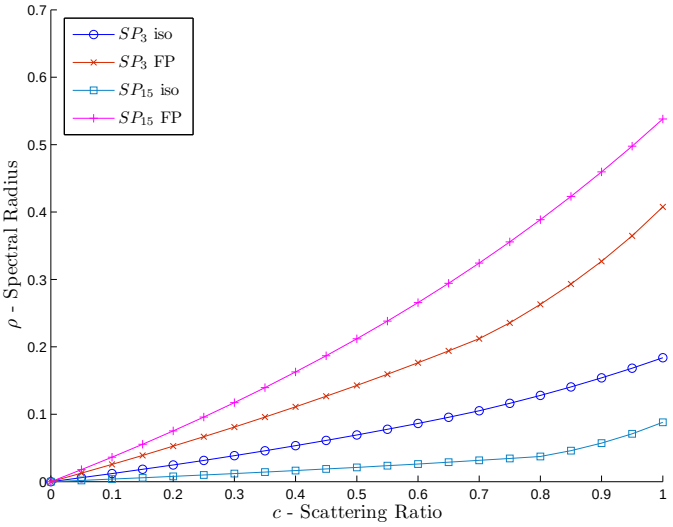


Figure 3.5: Canonical form with SI and AnMG

### *3.3.4 Iterative Efficiency*

With the knowledge of the spectral radius ($\rho$) for any given $SP_N$ form and iterative scheme, one can assess the effectiveness of the various solution techniques as follows: the slowest decaying error mode is attenuated by a factor of $\rho$ at each iteration. Thus the attenuation factor, $f$, after $\ell$ iterations is

$$f = \rho^{\ell}. \tag{3.80}$$

Therefore, to achieve an error reduction factor of $f$, the number of iterations required would be:

$$\ell = \frac{\log f}{\log \rho} \tag{3.81}$$

Noting that the number of diffusion operator solves per iteration is equal to $n$, we define the computational cost as Cost $= \ell \times n$. The iterative efficiency, $\eta$, is inversely proportional to the attenuation factor $f$ (the stronger the attenuation, the more efficient the scheme) and to the cost (the smaller the computational cost, the more efficient the scheme). $\eta$ is thus defined as:

$$\eta = \frac{1}{f \times \text{Cost}}. \tag{3.82}$$

Substitute in the definition for Cost,

$$\eta = \frac{\log \sqrt[n]{\rho}}{f \times \log f}. \tag{3.83}$$

Once an accuracy goal (i.e., a value of $f$) has been set, the efficiency of the scheme is dictated by

$$\eta \propto -\log \sqrt[n]{\rho} = -\frac{\log \rho}{n}. \tag{3.84}$$

The efficiencies for all the $SP_N$ forms and iterative methods discussed above are tabulated in Table 3.11 for $SP_3$, $SP_7$, and $SP_{15}$, and $c = 0.0, 0.5, 1.0$, respectively. From this table, we note that

- the canonical form of the $SP_N$ equations, solved with DSA or AnMG preconditioned SI, is the most effective approach for a wide range of $SP_N$ orders and a wide range of scattering ratios;

- the composite form, solved either with the Gauss-Seidel scheme or the explicit scheme, is the most effective scheme for low $SP_N$ orders and high scattering ratios; between the two scheme, the "EXPLICIT" is more favorable when $N$ is low and $c$ is away from unity.

- for highly anisotropic and highly scattering media, the composite form (solved with either Gauss-Seidel or "EXPLICIT") seems be a slightly better alternative than the canonical form with angular multi-grid for low to moderately high $SP_N$ orders, but for high $SP_N$ orders, the canonical formulation with multi-grid is more efficient. To demonstrate this, results of a Fourier analysis for $SP_{31}$ with $c = 1$ are presented in Table 3.12 where we note that, for high $SP_N$ orders, the canonical form with angular multigrid preconditioner is indeed the most efficient scheme and the composite form with either Gauss-Seidel or "EXPLICIT" procedures the second most efficient (a composite formulation is about 10 times more efficient than the canonical form with DSA preconditioning);

- the standard form of the $SP_N$ equations seems to be an overall poor scheme and is not recommended.

| | | | $c = 0.0$ | | $c = 0.5$ | | $c = 1.0$ | |
|---|---|---|---|---|---|---|---|---|
| | | | **ISO** | **F.P.** | **ISO** | **F.P.** | **ISO** | **F.P.** |
| $SP_3$ | **Standard** | G-S | 0.148 | 0.148 | 0.147 | 0.098 | 0.147 | 0.033 |
| | **Composite** | G-S | 0.176 | 0.176 | 0.272 | 0.230 | 0.552 | 0.525 |
| | | EXPLICIT | 0.323 | 0.323 | 0.409 | 0.327 | 0.552 | 0.525 |
| | **Canonical** | SI +$P_1$SA | 10.12 | 4.534 | 0.387 | 0.282 | 0.245 | 0.130 |
| | | SI +AnMG | 5.237 | 2.867 | 0.387 | 0.282 | 0.245 | 0.130 |
| $SP_7$ | **Standard** | G-S | 0.017 | 0.017 | 0.017 | 0.012 | 0.017 | 0.002 |
| | **Composite** | G-S | 0.034 | 0.034 | 0.038 | 0.047 | 0.044 | 0.105 |
| | | EXPLICIT | 0.002 | 0.002 | 0.019 | 0.004 | 0.051 | 0.107 |
| | **Canonical** | SI +$P_1$SA | 5.220 | 2.268 | 0.207 | 0.108 | 0.131 | 0.019 |
| | | SI +AnMG | 2.896 | 1.499 | 0.195 | 0.103 | 0.124 | 0.046 |
| $SP_{15}$ | **Standard** | G-S | 0.002 | 0.002 | 0.002 | 0.002 | 0.002 | 0.000 |
| | **Composite** | G-S | 0.007 | 0.007 | 0.008 | 0.011 | 0.008 | 0.023 |
| | | EXPLICIT | -0.053 | -0.053 | -0.049 | -0.052 | -0.045 | -0.014 |
| | **Canonical** | SI +$P_1$SA | 2.705 | 1.036 | 0.113 | 0.055 | 0.072 | 0.003 |
| | | SI +AnMG | 1.389 | 0.697 | 0.112 | 0.045 | 0.070 | 0.018 |

Table 3.11: Efficiency for various $SP_N$ forms and iterative methods, higher number means higher efficiency.

| $c = 1.0$ | | **ISO** | | **F.P.** | |
|---|---|---|---|---|---|
| $SP_{31}$ | | $\rho$ | $\eta$ | $\rho$ | $\eta$ |
| **Standard** | G-S | 0.99043 | 0.00026 | 0.99975 | 0.00001 |
| **Composite** | G-S | 0.93319 | 0.00188 | 0.82111 | 0.00535 |
| | EXPLICIT | 5.75013 | -0.04748 | 3.26213 | -0.03209 |
| **Canonical** | SI +$P_1$SA | 0.22289 | 0.03835 | 0.98411 | 0.00041 |
| | SI +AnMG | 0.06917 | 0.03742 | 0.56861 | 0.00791 |

Table 3.12: Spectral radii ($\rho$) and efficiency ($\eta$) for $SP_{31}$ with $c = 1.0$.

### *3.3.5 Conclusion*

Three different forms of the $SP_N$ equations have been reviewed: the standard form, the composite-moment form, and the canonical form. These forms cast the $SP_N$ equations into a system of coupled diffusion-like equations, to which various iterative techniques can be applied: a Gauss-Seidel approach for both the standard and the composite forms, with also a modified Gauss-Seidel variant for the composite form, and preconditioned source iteration for the canonical form. In this section we presented a comparison of the iterative properties for the various $SP_N$ formulations and their associated solution techniques. Fourier analysis results, performed for infinite medium, have also been verified using finite-element simulations. Both isotropic and highly anisotropic (Fokker-Planck) scattering laws have been considered. The scattering ratio has been varied from pure absorber ($c = 0$) to pure scatterer ($c = 1$) medium. Our results indicated that the canonical form is globally the most efficient approach to solve the $SP_N$ equations. In most situations, a $P_1$SA-preconditioned source iteration is the most favorable technique to solve the canonical form, but for high $SP_N$ orders with Fokker-Planck scattering, the angular multigrid preconditioner should be preferred. The composite form solved using "EXPLICIT" scheme can be more advantageous in some specific cases: for low $SP_N$ orders with highly anisotropic and highly scattering materials. The standard form never outperforms any other form and is not recommended for implementation.

# 4. MODEL ERROR QUANTIFICATION

The main objective of this Dissertation research is to establish a set of methods to estimate the model error associated with the $SP_N$ equations and to apply them to the PECOS problem to quantify the error in the quantities of interest. We use an $S_N$ solution of high value for $N$ as the true transport solution to compare the $SP_N$ solution with. We propose three types of approaches to estimate the model error: a *direct* method, a *residual* method, and an *adjoint* method. The first two fall in the forward method category, which requires both the $SP_N$ solution and the $S_N$ solution whenever the source condition is changed. The third one, however, only requires one $S_N$ adjoint solution. When the source condition changes, only the $SP_N$ equations need to be solved to compute the error in a response. The *direct* method is straightforward and thus the major part of the discussion in this section is dedicated to the latter two methods.

## 4.1 Model Error vs. Numerical Error

A numerical calculation usually suffers from two types of errors: model error and numerical error. Numerical error mainly arises from the discretization and solution process, while model error is associated with the modeling equation itself. To separate the model error from the numerical error, we need to suppress the numerical error by using fine space and angle meshes so that the numerical error is negligible compared to the model error.

Also, because we are comparing two numerical methods with each other ($SP_N$ vs. $S_N$), we also need to pay attention to the projection error, i.e., the error generated when projecting the solution from one mesh to another, if the meshes or the discretization schemes used by the two methods are different. To avoid the projection

error, we choose to investigate the difference between the canonical form of the $SP_N$ equations and even-parity form of the $S_N$ equations. One justification for choosing the Canonical $SP_N$ is that all the $SP_N$ forms are equivalent and we have shown that the canonical form offers the best iterative solution performance. More importantly, both canonical $SP_N$ and even-parity $S_N$ equations can be cast into second order forms and can be discretized using the same spatial discretization scheme, namely a tri-linear continuous finite-element scheme. Therefore, if we use the same spatial mesh for these two methods, no projection will be needed to compare the two solutions.

As stated at the beginning of this section, we want to quantify the model error by looking at various responses of interest. Although the second order forms have the advantage of iteratively decoupling unknowns along all the directions and being readily solved using a finite-element based diffusion solver, it poses its own technical challenge when the adjoint formula is called for, which will be very important when evaluating the error in the responses. Although many researchers have worked on the first-order adjoint $S_N$ equations, it seems that few have worked with the second order adjoint $S_N$ equations. The adjoint approach for the second-order form of the $S_N$ is by no means as straight-forward as for the first-order form, considering that it also has a set of first-order auxiliary equations for the odd-parity intensity as secondary unknowns. Furthermore, in this research we want to evaluate the error in both even and odd parity responses while only solving for the even-parity equations, we have to analyze the parity property of the response functions carefully and adjust our adjoint approach accordingly.

## 4.2 Four Classes of $QoI$

We are particularly interested in model errors for four types of quantities of interest ($QoI$): interior angular-integrated intensity, general interior flux, cell-averaged

interior flux, and boundary surface leakage, because they are of the keenest concern for the vehicle re-entry problem and also are the frequently sought-after $QoI$ in nuclear reactor engineering. For the $S_N$ transport equation, each of these quantities can be characterized by a response function ($r$), whose inner product with the angular intensity solution ($\psi$) will produce the response or $QoI$:

$$QoI = \langle r, \psi \rangle \, . \tag{4.1}$$

The response function $r$ is usually a function of $\underline{\boldsymbol{x}}$ and $\Omega$ and can be decomposed into a space-dependent function $\kappa(\underline{\boldsymbol{x}})$ and a angle-dependent function $\vartheta(\vec{\Omega})$:

$$r(\underline{\boldsymbol{x}}, \vec{\Omega}) = \kappa(\underline{\boldsymbol{x}})\vartheta(\vec{\Omega}). \tag{4.2}$$

For $SP_N$, while the $\Omega$-dependency is replaced by $\mu$-dependency, the general form of the inner product remains the same:

$$\langle f, g \rangle = \int_{-1}^{1} \int_{V} f \; g \; dV d\mu. \tag{4.3}$$

The only exception is that for the $SP_N$ response of the general interior flux, we need to construct the physical $\psi^-(\Omega)$ from the non-physical $SP_N$ solution $\vec{\psi}^-(\mu)$ and treat it as an $S_N$ response; or we can simply take the $\vec{\phi}_1$ at the point of interest, because in the $SP_N$ approximation, $\vec{\phi}_1$ represents the flux vector. We will discuss this later and it can be shown that the two approaches are equivalent.

### *4.2.1 Angle-integrated Intensity QoI*

The response function for the interior angle-integrated intensity is straightforward. The $S_N$ response function is simply

$$\vartheta(\vec{\Omega}) = 1.0, \qquad \text{for all } \Omega, \tag{4.4a}$$

$$\kappa(\underline{\boldsymbol{x}}) = \begin{cases} 1, & \text{in area of interest} \subset V, \\ 0, & \text{otherwise.} \end{cases} \tag{4.4b}$$

Similarly for the $SP_N$, $\vartheta(\mu) = 1.0$ for all $\mu$. Obviously this is an even-parity response function $r$. Since we are solving the even-parity equations for the even-parity angular intensity, the response can be easily computed using only even-parity quantities as:

$$QoI = \langle r, \psi \rangle = \left\langle r, \psi^{+} \right\rangle . \tag{4.5}$$

In special cases where the $QoI$ at a particular point ($\underline{\boldsymbol{x}}_0$) is desired, the space dependent component $\kappa$ becomes a delta function:

$$\kappa(\underline{\boldsymbol{x}}) = \delta(\underline{\boldsymbol{x}} - \underline{\boldsymbol{x}}_0), \tag{4.6}$$

and the angle-integrated $QoI$ is evaluated at that point.

### *4.2.2 Interior Flux QoI: General*

The response for the interior flux deserves some extra attention. For the $S_N$ method, the response functions is:

$$\vec{\vartheta}(\Omega) = \vec{\Omega}, \tag{4.7a}$$

$$\kappa(\underline{\boldsymbol{x}}) = \begin{cases} 1, & \text{in area of interest} \subset V \backslash \partial V, \\ 0, & \text{otherwise.} \end{cases} \tag{4.7b}$$

Note that we are only concerned with the interior flux here, therefore $\kappa$ has to be zero on the boundary, that is, the area of interest should not include boundary in this response. This is a vector response, whose components have to be computed one at a time. For illustration purpose, we consider the response along $\vec{e}_x$ direction, that is, we replace $\vec{\vartheta}$ with $\vartheta_x$:

$$\vartheta_x(\Omega) = \Omega_x, \tag{4.8}$$

and

$$r_x = \kappa \vartheta_x. \tag{4.9}$$

This is also an odd-parity response, which is orthogonal to the even-parity intensity that we are solving for, under the inner product defined as in Eq. (2.26). Although we can solve for the odd-parity intensity as a post-processing step and take its inner product with the above defined response function for the forward approach, it is not obvious how to develop an adjoint approach to compute the same response based on post-processing. However, the $\psi^-$ equation, Eq. (2.21), suggests that we can re-express $\psi^-$ in terms of $\vec{\nabla}\psi^+$. Substituting Eq. (2.21) into Eq. (4.1) and dropping the direction index $m$, we get:

$$\begin{aligned} QoI_x &= \left\langle r_x, \psi^- \right\rangle \\ &= \left\langle r_x, -\frac{\vec{\Omega}}{\sigma_t} \cdot \vec{\nabla}\psi^+ + \frac{1}{\sigma_t} Q^- \right\rangle \\ &= \underline{\underline{\left\langle r_x, -\frac{\vec{\Omega}}{\sigma_t} \cdot \vec{\nabla}\psi^+ \right\rangle}} + \left\langle r_x, \frac{1}{\sigma_t} Q^- \right\rangle. \end{aligned} \tag{4.10}$$

The second term only involves known quantities, hence we only need to focus on the first term, underlined. In order to eliminate the gradient operator on $\psi^+$, we integrate by parts:

$$\underline{\underline{\left\langle r_x, \ -\frac{\vec{\Omega}}{\sigma_t}\cdot\vec{\nabla}\psi^+ \right\rangle}} = -\int_{4\pi}\oint \frac{\vec{\Omega}\cdot\vec{n}}{\sigma_t} \underbrace{r_x}_{=0 \text{ on boundary}} \psi^+ dA d\Omega + \left\langle \vec{\Omega}\cdot\vec{\nabla}\frac{r_x}{\sigma_t}, \ \psi^+ \right\rangle. \tag{4.11}$$

We know that $r_x = 0$ the boundary, hence the above boundary term vanishes. We then notice that the remaining second term is an inner product between $\psi^+$ and an even parity quantity $\vec{\Omega}\cdot\vec{\nabla}\frac{r_x}{\sigma_t}$. This structure is very similar to the angle-integrated response of Eq. (4.5), with a substitution of $\vec{\Omega}\cdot\vec{\nabla}\frac{r_x}{\sigma_t}$ for the even parity response function $r$. This suggests that we can regard $\vec{\Omega}\cdot\vec{\nabla}\frac{r_x}{\sigma_t}$ as an equivalent even-parity response function $r'_x$:

$$r'_x = \vec{\Omega}\cdot\vec{\nabla}\frac{r_x}{\sigma_t}. \tag{4.12}$$

Due to the gradient operator acting on $r_x$, it will be difficult to deal with the point-wise response where the $\kappa$ is a spatial delta function. However, this difficulty can be circumvented in the adjoint approach in a finite element setting, as will be shown later. For the forward approach, we still recommend using the original response function given in Eq. (4.7).

For the $SP_N$ approach, we recall that it does not yield the true angular intensity (the $SP_N$ $\vec{\psi}^-$ does not carry physical sense since it is a vector instead of a scalar), a reconstruction scheme is needed to estimate the angular intensity from the $SP_N$ solution. After reconstruction, computing the response will be carried out in the same way as with the $S_N$ approach. Alternatively, one can skip the reconstruction step and directly obtain the vector $SP_N$ flux, $\vec{\phi}_1$, by taking the $P_1$ moment of the

$SP_N$ $\vec{\psi}^-$:

$$\vec{\phi}_1 = 2 \sum_{m=1}^{(N+1)/2} \mu_m \vec{\psi}_m^- w_m \tag{4.13}$$

The two methods may give the same result if a Legendre expansion based reconstruction scheme is used, thanks to the orthogonality of the Legendre polynomials used in that reconstruction process, which will be discussed in Section 4.3.

### *4.2.3 Interior Flux QoI: Cell-averaged*

Sometimes it is convenient to query the flux averaged over a cell (a fundamental element in a spatial discretization). The $S_N$ response function is the same as in the general flux response case, except that the support of the $\kappa$ is restricted to the cell of interest:

$$\kappa(\underline{\boldsymbol{x}}) = \begin{cases} 1/V_{\text{cell}}, & \text{inside the cell of interest,} \\ 0, & \text{otherwise.} \end{cases} \tag{4.14}$$

As before, the straightforward response function is not easy to work with in the adjoint approach because it requires knowledge of $\psi^-$. But averaging over a single cell allows us to tackle this problem in a different manner. It is not hard to see that this response can be transformed to rely on $\vec{\nabla}\psi^+$ averaged over a cell. Let us revisit Eq. (4.11) by substituting in $r_x = \kappa\vartheta_x$ and expanding out the inner product:

$$\begin{aligned} \underline{\underline{\left\langle r_x, \ -\frac{\vec{\Omega}}{\sigma_t} \cdot \vec{\nabla}\psi^+ \right\rangle}} &= -\int_{4\pi}\int_V \kappa\vartheta_x \frac{\vec{\Omega}}{\sigma_t}\vec{\nabla}\psi^+ \, dV d\Omega \\ &= -\int_{4\pi} \vec{\Omega}\vartheta_x \int_V \frac{1}{\sigma_t}\kappa\vec{\nabla}\psi^+ dV \, d\Omega. \end{aligned} \tag{4.15}$$

Noting that $\kappa$ is restricted to a single cell and assuming $\sigma_t$ is cell-wise constant, we get:

$$\underline{\underline{\left\langle r_x, \quad -\frac{\vec{\Omega}}{\sigma_t} \cdot \vec{\nabla}\psi^+ \right\rangle}} = -\int_{4\pi} \frac{\vec{\Omega}}{\sigma_{t,\text{cell}}} \vartheta_x \underbrace{\frac{1}{V_{\text{cell}}} \int_{\text{cell}} \vec{\nabla}\psi^+ dV}_{\overline{\vec{\nabla}\psi^+}} \, d\Omega. \tag{4.16}$$

If we least-square fit the $\psi^+$ on to a set of bilinear polynomials in 2D (or trilinear in 3D), which will be exact within each cell if we are solving the equations using first-order finite element method, we can approximate the average of $\vec{\nabla}\psi^+$ within any single cell with an integral operator. That operator can then be manufactured into our response function. That is, with a modified response function $r'$, we can take $\langle r', \psi^+ \rangle$ which is equivalent to $\langle r, \psi^- \rangle$, which is the flux response that we seek.

#### *4.2.3.1 Least-square Approximation to $\vec{\nabla}$ on a Linear Trial Basis*

Take 2D for example. Suppose we approximate an arbitrary spatially varying function ($f$) within a given cell by least-squares fitting a bilinear polynomial, which is:

$$\tilde{f}(x,y) \approx {}_0\tilde{f} + {}_1\tilde{f} \cdot (x - x_0) + {}_2\tilde{f} \cdot (y - y_0) + {}_3\tilde{f} \cdot (x - x_0)(y - y_0), \tag{4.17}$$

where $x_0$ and $y_0$ are the coordinates of the cell center and the coefficients ${}_0\tilde{f}$, ${}_1\tilde{f}$, ${}_2\tilde{f}$, and ${}_3\tilde{f}$ are to be determined. By taking the gradient of the above linear approximation Eq. (4.17) and then averaging them across the cell, we get:

$$\nabla_x \tilde{f}(x,y) = {}_1\tilde{f} + {}_3\tilde{f}(y - y_0) \quad \Rightarrow \overline{\nabla_x \tilde{f}(x,y)} = {}_1\tilde{f}, \tag{4.18a}$$

$$\nabla_y \tilde{f}(x,y) = {}_2\tilde{f} + {}_3\tilde{f}(x - x_0) \quad \Rightarrow \overline{\nabla_y \tilde{f}(x,y)} = {}_2\tilde{f}. \tag{4.18b}$$

Since we are only concerned with the average gradient over the cell, let us determine the coefficient ${}_1\tilde{f}$ and ${}_2\tilde{f}$. According to least-square fitting theory, the trial basis functions should be orthogonal to the error in the trial space, thus:

$$\iint_{\text{cell}} [f(x,y) - \tilde{f}(x,y)](x - x_0)dxdy = 0, \tag{4.19a}$$

$$\iint_{\text{cell}} [f(x,y) - \tilde{f}(x,y)](y - y_0)dxdy = 0. \tag{4.19b}$$

Plugging in the expression for $\tilde{f}$ and carrying out the integration, we get

$$\iint_{\text{cell}} f(x,y)(x - x_0)dxdy = {}_1\tilde{f} \cdot \underbrace{\iint_{\text{cell}} (x - x_0)^2 dxdy}_{\text{coeff}_x} \tag{4.20a}$$

and

$$\iint_{\text{cell}} f(x,y)(y - y_0)dxdy = {}_2\tilde{f} \cdot \underbrace{\iint_{\text{cell}} (y - y_0)^2 dxdy}_{\text{coeff}_y}. \tag{4.20b}$$

Therefore,

$$\overline{\nabla_x f} \approx \overline{\nabla_x \tilde{f}} = {}_1\tilde{f} = \frac{\iint_{\text{cell}} f(x,y)(x - x_0)dxdy}{\text{coeff}_x}, \tag{4.21a}$$

and

$$\overline{\nabla_y f} \approx \overline{\nabla_y \tilde{f}} = {}_2\tilde{f} = \frac{\iint_{\text{cell}} f(x,y)(y - y_0)dxdy}{\text{coeff}_y}. \tag{4.21b}$$

#### 4.2.3.2 The Modified Response Function

Using Eq. (4.21), we can express the average gradient of the even-parity angular intensity, $\overline{\vec{\nabla}\psi^+}$, as:

$$\begin{aligned}
\overline{\vec{\nabla}\psi^+} &\approx \overline{\nabla_x\tilde{\psi}^+}\,\vec{e}_x + \overline{\nabla_y\tilde{\psi}^+}\,\vec{e}_y && (4.22)\\
&= \frac{\iint_{\text{cell}}\psi^+(x,y)(x-x_0)dxdy}{\text{coeff}_x}\vec{e}_x + \frac{\iint_{\text{cell}}\psi^+(x,y)(y-y_0)dxdy}{\text{coeff}_y}\vec{e}_y && (4.23)\\
&= \iint_{\text{cell}}\left[\frac{(x-x_0)\vec{e}_x}{\text{coeff}_x} + \frac{(y-y_0)\vec{e}_y}{\text{coeff}_y}\right]\psi^+(x,y)dxdy, && (4.24)
\end{aligned}$$

where, in our context, $\psi^+(x,y)$ is the finite-element approximation to the even-parity angular intensity in that cell. Plugging Eq. (4.24) in Eq. (4.16), we obtain:

$$\begin{aligned}
\underline{\underline{\left\langle r_x,\ -\frac{\vec{\Omega}}{\sigma_t}\cdot\vec{\nabla}\psi^+\right\rangle}} &\approx -\int_{4\pi}\frac{\vec{\Omega}}{\sigma_{t,\text{cell}}}\vartheta_x\iint_{\text{cell}}\left[\frac{(x-x_0)\vec{e}_x}{\text{coeff}_x} + \frac{(y-y_0)\vec{e}_y}{\text{coeff}_y}\right]\psi^+dxdy\,d\Omega\\
&= -\int_{4\pi}\iint_{\text{cell}}\frac{\vartheta_x}{\sigma_{t,\text{cell}}}\left[\frac{(x-x_0)\Omega_x}{\text{coeff}_x} + \frac{(y-y_0)\Omega_y}{\text{coeff}_y}\right]\psi^+dxdyd\Omega. && (4.25)
\end{aligned}$$

We can further recast the above expression into an integration over the whole phase space by using a modified spatial function $\kappa'$:

$$\underline{\underline{\left\langle r_x,\ -\frac{\vec{\Omega}}{\sigma_t}\cdot\vec{\nabla}\psi^+\right\rangle}} \approx \int_{4\pi}\iint\underbrace{-\kappa'\frac{\vartheta_x}{\sigma_{t,\text{cell}}}\left[\frac{(x-x_0)\Omega_x}{\text{coeff}_x} + \frac{(y-y_0)\Omega_y}{\text{coeff}_y}\right]}_{r'_x}\psi^+dxdyd\Omega, \tag{4.26}$$

where

$$r'_x = -\kappa'\frac{\vartheta_x}{\sigma_{t,\text{cell}}}\left[\frac{(x-x_0)\Omega_x}{\text{coeff}_x} + \frac{(y-y_0)\Omega_y}{\text{coeff}_y}\right], \tag{4.27}$$

and

$$\kappa'(\underline{\boldsymbol{x}}) = \begin{cases} 1, & \text{inside the cell of interest,} \\ 0, & \text{otherwise.} \end{cases} \tag{4.28}$$

We can see that Eq. (4.26) is in an pure integral form that is consistent with our definition of the inner product, Eq. (4.1). And here $\vec{r'}$ is our modified response function, whose response along the x-axis, $\langle r'_x, \psi^+ \rangle$, for instance, is equivalent to $\left\langle r_x, -\frac{\vec{\Omega}}{\sigma_t} \cdot \vec{\nabla}\psi^+ \right\rangle$. In the same way as we did in the general flux case, the quantify of interest along the $x$-direction can be computed as:

$$\begin{aligned} QoI_x &= \underline{\underline{\left\langle r_x, -\frac{\vec{\Omega}}{\sigma_t} \cdot \vec{\nabla}\psi^+ \right\rangle}} + \left\langle r_x, \frac{1}{\sigma_t} Q^- \right\rangle \\ &\approx \left\langle r'_x, \psi^+ \right\rangle + \left\langle r_x, \frac{1}{\sigma_t} Q^- \right\rangle, \end{aligned} \tag{4.29}$$

where $Q^-$ is not present if scattering and the external source are isotropic. In that case, the expression reduces to:

$$QoI_x \approx \left\langle r'_x, \psi^+ \right\rangle \tag{4.30}$$

Again, the response computed in this way is a least-square approximation to the cell-averaged flux. Furthermore, when first-order finite element is used in solving the equations, the approximation is exact.

For $SP_N$, we can start with the $P_1$ equations (assuming isotropic scattering and external source, i.e., $\sigma_{s,l} = Q_l = 0$ for $l > 0$):

$$\frac{2}{3}\vec{\nabla}\phi_2 + \frac{1}{3}\vec{\nabla}\phi_0 + \sigma_t \vec{J} = 0, \tag{4.31}$$

where $\vec{J} = \vec{\phi}_1$ is the $SP_N$ flux, the response we are after in this section. Hence:

$$\overrightarrow{QoI} = \overline{\vec{J}} = \int_V \kappa' \vec{\phi}_1 dV = -\frac{1}{\sigma_t}\left(\frac{2}{3}\overline{\vec{\nabla}\phi_2} + \frac{1}{3}\overline{\vec{\nabla}\phi_0}\right). \tag{4.32}$$

Applying Eq. (4.21) to the expression for $\vec{J}$ above, we get:

$$\begin{aligned}\overrightarrow{QoI} \approx & -\frac{1}{\sigma_t}\left[\frac{2}{3}\frac{\iint \kappa'\phi_2(x,y)(x-x_0)dxdy}{\text{coeff}_x} + \frac{1}{3}\frac{\iint \kappa'\phi_0(x,y)(x-x_0)dxdy}{\text{coeff}_x}\right]\vec{e}_x \\ & -\frac{1}{\sigma_t}\left[\frac{2}{3}\frac{\iint \kappa'\phi_2(x,y)(y-y_0)dxdy}{\text{coeff}_y} + \frac{1}{3}\frac{\iint \kappa'\phi_0(x,y)(y-y_0)dxdy}{\text{coeff}_y}\right]\vec{e}_y. \end{aligned} \tag{4.33}$$

Note that:

$$\begin{aligned}\phi_0 &= \textstyle\int_{-1}^{1} \psi d\mu = \int_{-1}^{1} \psi^+ d\mu, \\ \phi_2 &= \textstyle\int_{-1}^{1} P_2(\mu)\psi d\mu = \int_{-1}^{1} P_2(\mu)\psi^+ d\mu.\end{aligned} \tag{4.34}$$

Substituting Eq. (4.34) into Eq. (4.33), we obtain a modified response function $\vec{r'}$, whose components are given by:

$$r'_x = -\frac{\kappa'}{3\sigma_t}\left(\frac{2P_2(\mu)}{\text{coeff}_x} + \frac{1}{\text{coeff}_x}\right)(x - x_0), \tag{4.35a}$$

$$r'_y = -\frac{\kappa'}{3\sigma_t}\left(\frac{2P_2(\mu)}{\text{coeff}_y} + \frac{1}{\text{coeff}_y}\right)(y - y_0). \tag{4.35b}$$

Then the $\overrightarrow{QoI}$ can be computed using the inner product notation:

$$\overrightarrow{QoI} \approx \left\langle \vec{r'}, \psi^+ \right\rangle. \tag{4.36}$$

The above analyses are done in 2-D as an example. They can be easily generalized to 3-D.

### *4.2.4 Boundary Leakage QoI*

The boundary leakage response function is different from all previously discussed response functions in that the boundary leakage response function is only defined on the boundaries of the problem domain and the angular component of the response function is only defined for the out-going directions. For an $S_N$ response, these two restrictions are imposed on $\vartheta(\vec{\Omega})$ and $\kappa(\underline{\boldsymbol{x}})$ respectively:

$$\begin{aligned} \vartheta(\vec{\Omega}) &= \begin{cases} \vec{\Omega}\cdot\vec{n}, & \vec{\Omega}\cdot\vec{n}\geq 0, \\ 0, & \text{otherwise}, \end{cases} \\ \kappa(\underline{\boldsymbol{x}}) &= \begin{cases} 1, & \text{in area of interest} \subset \partial V, \\ 0, & \text{other area} \subset \partial V. \end{cases} \end{aligned} \tag{4.37}$$

Accordingly, the inner product needs to be modified such that the integral is only carried out over the surface, rather than the whole volume. We denote the surface inner product by $\lceil\cdot,\cdot\rceil$ and the boundary leakage response can be computed as:

$$QoI = \lceil r,\psi\rceil = \int_{4\pi}\oint_{\partial V}\kappa(\underline{\boldsymbol{x}})\vartheta(\vec{\Omega})\psi(\underline{\boldsymbol{x}},\vec{\Omega})dAd\Omega, \tag{4.38}$$

where the $\lceil\cdot,\cdot\rceil$ inner product between two arbitrary functions $f$ and $g$ is defined as:

$$\lceil f,g\rceil = \int_{4\pi}\oint_{\partial V} f\ g\ dAd\Omega. \tag{4.39}$$

Note that the surface inner product is no longer an integration over the whole phase space.

For $SP_N$, $\vartheta(\vec{\Omega})$ is changed to $\vartheta(\mu)$:

$$\vartheta(\mu) = \begin{cases} \mu, & \mu \geq 0, \\ 0, & \text{otherwise}, \end{cases} \tag{4.40}$$

and the inner product is changed to:

$$\lceil f, g \rceil = \int_{-1}^{1} \oint_{\partial V} f \; g \; dA d\mu. \tag{4.41}$$

A subtlety of this kind of response is that it requires knowledge of the full angular intensity ($\psi$) for the out-going directions on the surface but our $\psi^-$ is defined on the basis of $\vec{\nabla}\psi^+$, which only lives in cell interior. However, we can infer the $\psi^-$ value by using the boundary condition ($g$). For $S_N$, we can use Eq. (2.19) to obtain $\psi^-$ for the out-going directions:

$$\psi^-(\Omega) = \psi^+(\Omega) - g(-\Omega), \qquad \text{for } \vec{\Omega} \cdot \vec{n} > 0. \tag{4.42}$$

Then,

$$\psi(\Omega) = \psi^+(\Omega) + \psi^-(\Omega) = 2\psi^+(\Omega) - g(-\Omega), \qquad \text{for } \vec{\Omega} \cdot \vec{n} > 0. \tag{4.43}$$

Similarly for $SP_N$, the $\vec{\psi}^-(\mu) \cdot \vec{n}$ for the out-going directions can be obtained from Eq. (3.23):

$$\vec{\psi}^-(\mu) \cdot \vec{n} = \psi^+(\mu) - g(\mu), \qquad \text{for } \mu > 0. \tag{4.44}$$

Then

$$\psi(\mu) = \psi^+(\mu) + \vec{\psi}^-(\mu) \cdot \vec{n} = 2\psi^+(\mu) - g(\mu), \qquad \text{for } \mu > 0. \tag{4.45}$$

So, generally for both $S_N$ and $SP_N$ models, the $QoI$ associated with boundary leakage can be computed as:

$$QoI = \lceil r, \psi \rceil = \lceil r, 2\psi^+ - g \rceil. \tag{4.46}$$

## 4.3 Reconstructing Angular Intensity from $SP_N$ Solutions

We now address how the angular intensity is reconstructed from the $SP_N$ solution. Recall that in the $SP_N$ equations, the even-parity unknowns are scalars, while the odd-parity unknowns are vectors. It is not obvious how to interpret the vectors of odd-parity 'angular intensities' or 'moments'. In fact only the zero-th and first order moments carry a physical meaning: $\phi_0$ represents the angle integrated intensity, and $\vec{\phi}_1$ represents the flux. Higher order moments are auxiliary unknowns produced by the mathematical manipulation leading to the $SP_N$ formulation. There is one exception, however, that for 1-D problems the vectors of odd-parity unknowns reduce to scalar quantities and regain their physical sense. Indeed, in 1-D the $SP_N$ equations are equivalent to the $S_{N+1}$ equations and they produce the same angular intensity if we use the same quadrature set for $\mu_m$ in $SP_N$ and polar angle in $S_{N+1}$. Also, the boundary conditions need to be consistent between $SP_N$ and $S_{N+1}$, for example in Mark boundary conditions we need to make sure the $SP_N$ incident angular intensity corresponding to direction cosine $\mu_m = \vec{\Omega}_{m'} \cdot \vec{n}$ is actually the angular integral of the $S_{N+1}$ over the angular domain defined by $\{\vec{\Omega}_{m'} | \vec{\Omega}_{m'} \cdot \vec{n} = \mu_m\}$. This is consistent with the fact that the $SP_N$ is originally derived from the 1-D $S_{N+1}$ and generalized to 3-D. How to reasonably reconstruct a meaningful angular intensity from the $SP_N$ solution is a very important prerequisite for model error analyses. To our knowledge this is still an open question.

In this research, we developed two sets of angular intensity reconstruction schemes for the $SP_N$ formulation. The logic behind one of the schemes is to preserve the

zero-th and first order $SP_N$ moments. The other is to preserve the zero-th order moment while ensuring the relationship between the even- and odd-parity intensities be compatible with the $S_N$ equations. They all have to yield the original $SP_N$ solution when the problem is 1-D. As we shall see later, each reconstruction scheme has its unique virtue that can be used to our advantage in different aspects of the error analyses process.

The two reconstruction schemes share one basic idea in common. We know that $SP_N$ solution converges to $S_{N+1}$ solution when the solution becomes locally 1-D. In that locally 1-D setting we can make some physical sense out of the $\mu$-dependency of the $SP_N$ solution by considering that the $\mu$ can be interpreted as $\vec{\Omega} \cdot \vec{k}$, where $\vec{\Omega}$ is the angular direction vector and $\vec{k}$ is the reference direction along which the solution varies locally. At the boundary, the $SP_N$ solutions tend to vary along the surface normal ($\vec{n}$) direction, therefore we choose $\vec{k} = \vec{n}$ on the boundary. In the interior, the reference direction is dictated by the $SP_N$ flux, $\vec{\phi}_1$:

$$\vec{k} = \begin{cases} \vec{n} & \text{on the boundary,} \\ \frac{\vec{\phi}_1}{\|\vec{\phi}_1\|} & \text{in the interior.} \end{cases} \tag{4.47}$$

By relating $\mu$ in the $SP_N$ formulation to $\vec{\Omega}$ through $\vec{k}$, we are ready to reconstruct a physical angular intensity from generally non-physical $SP_N$ quantities.

### *4.3.1 A Legendre Expansion Reconstruction Scheme*

This first scheme is based on the fact that in 1-D $SP_N$, which is equivalent to 1-D $P_n$, the angular intensity is expanded in Legendre polynomials. That is:

$$\psi(\underline{\boldsymbol{x}}, \mu) = \sum_{l=0}^{n} \frac{2l+1}{2} \phi_l(\underline{\boldsymbol{x}}) P_l(\mu). \tag{4.48}$$

There are two difficulties when trying to adapt Eq. (4.48) in 3-D. The first is that although $\mu$ is well defined in 1-D, it meaning is ambiguous in 3-D. The other is that in 3-D the odd $SP_N$ moments $(\vec{\phi}_1, \vec{\phi}_3, \vec{\phi}_5, \cdots)$ are vectors, which cannot be directly plugged into Eq. (4.48).

We tackle the first difficulty by relating the $\mu$ to $\vec{\Omega} \cdot \vec{k}$. For the vector odd moments, we simply take their projection along $\vec{k}$, $\vec{\phi}_l \cdot \vec{k}$, and use it in place of the original odd moments in Eq. (4.48). We hereby stress again that reconstructing the angular intensity is still an open area and we chose our method because it suits our needs, but it may not be necessarily the best. Finally, the reconstruction scheme is:

$$\psi_{SP_N \to S_{N'}}(\underline{\boldsymbol{x}}, \vec{\Omega}_m) = \sum_{l=0,2,\cdots}^{N-1} \frac{2l+1}{4\pi} \phi_l(\underline{\boldsymbol{x}}) P_l(\vec{\Omega}_m \cdot \vec{k}) + \sum_{l=1,3,\cdots}^{N} \frac{2l+1}{4\pi} \vec{\phi}_l(\underline{\boldsymbol{x}}) \cdot \vec{k} P_l(\vec{\Omega}_m \cdot \vec{k}), \tag{4.49}$$

where $m = 1, \ldots, N'(N'+1)/2$. Alternatively, one can express the reconstruction in terms of even- and odd-parity components:

$$\psi^{+}_{SP_N \to S_{N'}}(\underline{\boldsymbol{x}}, \vec{\Omega}) = \sum_{l=0,2,\cdots}^{N-1} \frac{2l+1}{4\pi} \phi_l(\underline{\boldsymbol{x}}) P_l(\vec{\Omega} \cdot \vec{k}), \tag{4.50}$$

$$\psi^{-}_{SP_N \to S_{N'}}(\underline{\boldsymbol{x}}, \vec{\Omega}) = \sum_{l=1,3,\cdots}^{N} \frac{2l+1}{4\pi} \vec{\phi}_l(\underline{\boldsymbol{x}}) \cdot \vec{k} P_l(\vec{\Omega} \cdot \vec{k}). \tag{4.51}$$

where we dropped the angular index $m$ for simplicity. It can be easily seen that in 1-D, $\vec{k}$ becomes the $x$-direction thus $\vec{\Omega} \cdot \vec{k} = \mu$. Furthermore, the odd moments revert back to the scalar version and the Eq. (4.49) reduces to Eq. (4.48), therefore the 1-D $SP_N$ solution is preserved. In 3-D, the $SP_N$ zero-th moment and first moment are still preserved, as can be shown as follows:

Zero-th moment:

$$\phi_{0,SP_N\to S_{N'}} = \int_{4\pi} \psi_{SP_N\to S_{N'}} d\Omega = \int_{4\pi} \psi_{SP_N\to S_{N'}} P_0(\vec{\Omega}\cdot\vec{k}) d\Omega \xrightarrow[\text{orthogonality}]{\text{Legendre polynomial}} \phi_0. \tag{4.52}$$

First moment:

To prove that the first moment is preserved, we need to decompose the direction vector $\vec{\Omega}$ into its components along $\vec{k}$ direction and perpendicular to $\vec{k}$ direction:

$$\vec{\Omega} = \vec{\Omega}_k + \vec{\Omega}_{k\perp}, \tag{4.53}$$

where

$$\vec{\Omega}_k = (\vec{\Omega}\cdot\vec{k})\vec{k} = \Omega_k\vec{k}, \tag{4.54}$$

$$\vec{\Omega}_{k\perp} = \vec{\Omega} - \vec{\Omega}_k. \tag{4.55}$$

Then, taking the first moment of $\psi_{SP_N\to S_{N'}}$ and plugging in Eq. (4.49), we get:

$$\begin{aligned}\vec{\phi}_{1,SP_N\to S_{N'}} &= \int_{4\pi} \vec{\Omega}\psi_{SP_N\to S_{N'}} d\Omega \\ &= \sum_{l=0,2,\cdots}^{N-1} \frac{2l+1}{4\pi} \int_{4\pi} \phi_l(\underline{\boldsymbol{x}})\ P_l(\Omega_k)\ (\vec{\Omega}_k + \vec{\Omega}_{k\perp})\ d\Omega \\ &\quad + \sum_{l=1,3,\cdots}^{N} \frac{2l+1}{4\pi} \int_{4\pi} \vec{\phi}_l(\underline{\boldsymbol{x}})\cdot\vec{k}\ P_l(\Omega_k)\ (\vec{\Omega}_k + \vec{\Omega}_{k\perp})\ d\Omega.\end{aligned} \tag{4.56}$$

It is easy to see from Fig. 4.1 that for a given $\Omega_k$, the $P_l(\Omega_k)$ is fixed and the $\vec{\Omega}_{k\perp}$ is $2\pi$ symmetric with respect to the $\vec{k}$ axis, therefore the integration over the angular domain defined by $\Omega_k$ is zero. And the the same thing holds true for all $\Omega_k \in [-1, 1]$.

Hence the entire integration over $4\pi$ is zero. This conclusion does not depend on $P_l$ order so we can safely eliminate all the $\vec{\Omega}_{k\perp}$ terms in Eq. (4.56).

Now for the $\vec{\Omega}_k$ term, we can write it out as $\vec{\Omega}_k = \Omega_k \vec{k}$. and plug back to Eq. (4.56):

$$\vec{\phi}_{1,SP_N \to S_{N'}} = \sum_{l=0,2,\cdots}^{N-1} \frac{2l+1}{4\pi} \vec{k} \int_{4\pi} \phi_l(\underline{\boldsymbol{x}})\ P_l(\Omega_k)\ \Omega_k\ d\Omega + \sum_{l=1,3,\cdots}^{N} \frac{2l+1}{4\pi} \vec{k} \int_{4\pi} \vec{\phi}_l(\underline{\boldsymbol{x}}) \cdot \vec{k}\ P_l(\Omega_k)\ \Omega_k\ d\Omega. \tag{4.57}$$

We can further decompose $d\Omega$ as $d\Omega = d\Omega_k d\varphi$ where $\varphi$ is as shown in the Fig. 4.1.

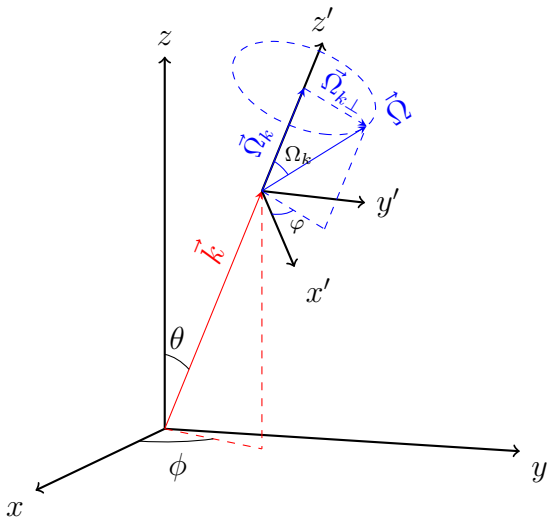


Figure 4.1: Decomposition of $\vec{\Omega}$ with respect to $\vec{k}$

The integration now becomes:

$$\vec{\phi}_{1,SP_N\to S_{N'}} = \sum_{l=0,2,\cdots}^{N-1} \frac{2l+1}{4\pi}\vec{k}\int_{2\pi}\left[\int_{-1}^{1}\phi_l(\underline{\boldsymbol{x}})\ P_l(\Omega_k)\ \Omega_k\ d\Omega_k\right]d\varphi$$
$$+\sum_{l=1,3,\cdots}^{N} \frac{2l+1}{4\pi}\vec{k}\int_{2\pi}\left[\int_{-1}^{1}\vec{\phi}_l(\underline{\boldsymbol{x}})\cdot\vec{k}\ P_l(\Omega_k)\ \Omega_k\ d\Omega_k\right]d\varphi. \qquad (4.58)$$

Applying the orthogonality of the Legendre polynomial again (recall $P_1(\Omega_k) = \Omega_k$) we are left with only the first moment term:

$$\vec{\phi}_{1,SP_N\to S_{N'}} = (\vec{\phi}_1(\underline{\boldsymbol{x}})\cdot\vec{k})\vec{k} = \vec{\phi}_1. \qquad (4.59)$$

### *4.3.2 A Hybrid Reconstruction Scheme*

The purpose of the Hybrid scheme is to make the reconstructed angular intensity satisfy the $S_N$ even-odd parity relationship, namely, Eq. (2.21). Dropping the direction index $m$ and neglecting the odd-parity source, we have

$$\psi^- = -\frac{\vec{\Omega}}{\sigma_t}\cdot\vec{\nabla}\psi^+. \qquad (4.60)$$

We start with the same reconstruction scheme for the $\psi^+_{SP_N\to S_{N'}}$ as given in the first scheme, Eq. (4.50). But to ensure the $S_N$ relationship, we substitute the $\psi^+_{SP_N\to S_{N'}}$ into Eq. (4.60) and generate the corresponding $\psi^-_{SP_N\to S_{N'}}$:

$$\psi^-_{SP_N\to S_{N'}} = -\frac{\vec{\Omega}}{\sigma_t}\cdot\vec{\nabla}\psi^+_{SP_N\to S_{N'}}. \qquad (4.61)$$

In 1-D, Eq. (4.61) reduce to:

$$\psi^-_{SP_N\to S_{N'}} = -\frac{\mu}{\sigma_t}\frac{\partial}{\partial x}\psi^+_{SP_N\to S_{N'}}, \qquad (4.62)$$

which conforms with the odd-parity equation in the canonical $SP_N$ form, namely, Eq. (3.18b). Therefore, the $SP_N$ even/odd parity relationship is satisfied by the Hybrid scheme in 1-D scenario. Considering that the same $\psi^+_{SP_N\to S_{N'}}$ from the Legendre expansion scheme has been shown to preserve the 1-D $SP_N$ solution, we can conclude that the entire Hybrid scheme also preserves the 1-D $SP_N$ solution.

In 3-D, the Hybrid scheme still preserves the zero-th moment, because the zero-th moment only depends on $\psi^+_{SP_N\to S_{N'}}$ which has been proved to preserve the zero-th moment previously. Higher order moments, however, are generally not preserved by the Hybrid scheme, because the $SP_N$ relationship is not satisfied. There are two exceptions to this statement: one is that when the problem becomes 1-D, all the higher moments are preserved; the other one is that if we are reconstructing from an $SP_1$ solution, the Hybrid scheme will preserve both $P_0$ and $P_1$ moments. The first one is obvious from our 1-D discussion; the latter one can be shown as follows:

$$\psi^+_{SP_N\to S_{N'}} = \frac{\phi_0}{4\pi}, \tag{4.63}$$

$$\psi^-_{SP_N\to S_{N'}} = -\frac{\vec{\Omega}}{\sigma_t}\cdot\vec{\nabla}\psi^+_{SP_N\to S_{N'}} = -\frac{\vec{\Omega}}{\sigma_t}\cdot\vec{\nabla}\left(\frac{\phi_0}{4\pi}\right), \tag{4.64}$$

$$\begin{aligned}\vec{\phi}_{1,SP_N\to S_{N'}} &= \int_{4\pi}\psi^-_{SP_N\to S_{N'}}\vec{\Omega}d\Omega = \int_{4\pi}\left(-\frac{\vec{\Omega}}{\sigma_t}\cdot\vec{\nabla}\frac{\phi_0}{4\pi}\right)\vec{\Omega}d\Omega \\ &= -\frac{1}{4\pi\sigma_t}\vec{\nabla}\phi_0\cdot\int_{4\pi}\vec{\Omega}\otimes\vec{\Omega}d\Omega \\ &= -\frac{1}{3\sigma_t}\vec{\nabla}\phi_0 \quad .\end{aligned} \tag{4.65}$$

Eq. (4.65) is actually the Fick's law, which is satisfied by the $SP_1$ equations.

One more comment on the reconstruction schemes: both schemes can rigorously reproduce the $SP_N$ angle-integrated intensity ($P_0$ moment) by adopting a simple isotropic reconstruction that truncates all the higher order moments starting from

$P_1$. This is illustrated in Eq. (4.63). This statement can be verified easily using Legendre polynomial orthogonality.

## 4.4 Three Methods to Compute the Model Error in $QoI$s

As introduced at the beginning of this section, three methods for evaluating the model error in a quantity of interest have been were proposed and investigated. In the forward method category we have the *direct* method and the *residual* method. The third approach is based on the *adjoint* . The latter two methods require an angular intensity reconstruction and are mathematically equivalent. The relationship between these three methods is illustrated in the Table 4.1.

| | | |
|---|---|---|
| Forward | Direct Method | |
| | Residual Method | require angular intensity reconstruction |
| | Adjoint Method | |

Table 4.1: Three methods for error estimation.

Because the *direct* method does not require any reconstruction scheme, the model error computed by this method is considered to be the reference. While we have shown that both reconstruction schemes are rigorous in a $P_0$ sense, the $S_N$-compatible hybrid scheme generally does not preserve the $SP_N$ first moment, thus the error in the flux $QoI$ produced by either the *residual* method or the *adjoint* method based on this reconstruction scheme does not represent the model error exactly. For the boundary leakage $QoI$, since no reconstruction scheme preserves all the higher moments, the error produced by the *residual* method and *adjoint* method will always be different from the reference model error. However, we can compensate for that difference

accurately by knowing the $SP_N$ solution. Since we need to perform one $SP_N$ solve regardless of which method is used, this error compensation does not incur any additional computational cost (in terms of diffusion solves). We will discuss this topic later in this section.

### *4.4.1 Forward Approach: Direct Method*

Applying the *direct* method to obtain the model error is straightforward. After a single $SP_N$ calculation and a single $S_N$ calculation, performed separately, the error in the $QoI$ ($\delta QoI$) is given by:

$$\delta QoI = QoI_{S_{N'}} - QoI_{SP_N} = \left\langle r_{S_N}, \psi_{S_{N'}} \right\rangle - \left\langle r_{SP_N}, \psi_{SP_N} \right\rangle . \tag{4.66}$$

#### *4.4.1.1 Angle-integrated QoI*

As shown in Section 4.2.1, the angular component of both response functions are unity. Therefore the response functions $r$ are given by $r_{S_N} = \kappa(\underline{\boldsymbol{x}})$ and $r_{SP_N} = \kappa(\underline{\boldsymbol{x}})$ respectively. The error in the $QoI$ can then be computed as follows:

$$\delta QoI = \left\langle r_{S_N}, \psi_{S_{N'}} \right\rangle - \left\langle r_{SP_N}, \psi_{SP_N} \right\rangle = \left\langle r_{S_N}, \psi^+_{S_{N'}} \right\rangle - \left\langle r_{SP_N}, \psi^+_{SP_N} \right\rangle . \tag{4.67}$$

#### *4.4.1.2 Interior Current QoI: General*

For *direct* method, we use the conventional response function. According to Section 4.2.2:

$$\vartheta_{S_N} = \vec{\Omega}, \tag{4.68}$$

$$\vartheta_{SP_N} = \mu. \tag{4.69}$$

The rest of the computation can be done following the general procedure as shown in Eq. (4.66).

#### *4.4.1.3 Interior Current QoI: Cell-averaged*

As discussed in Section 4.2.3, this response is based on trilinear least-square fitting. Therefore, both $S_N$ and $SP_N$ response should be computed using the modified response function derived from the least-square fitting process. Let us take the 2-D example given in Section 4.2.3 and generalize it to 3-D:

$$\vec{r'}_{S_N} = \begin{pmatrix} \kappa' \frac{\Omega_x}{\sigma_{t,\text{cell}}} \left[ \frac{(x-x_0)\Omega_x}{\text{coeff}_x} + \frac{(y-y_0)\Omega_y}{\text{coeff}_y} + \frac{(z-z_0)\Omega_z}{\text{coeff}_z} \right] \\ \kappa' \frac{\Omega_y}{\sigma_{t,\text{cell}}} \left[ \frac{(x-x_0)\Omega_x}{\text{coeff}_x} + \frac{(y-y_0)\Omega_y}{\text{coeff}_y} + \frac{(z-z_0)\Omega_z}{\text{coeff}_z} \right] \\ \kappa' \frac{\Omega_z}{\sigma_{t,\text{cell}}} \left[ \frac{(x-x_0)\Omega_x}{\text{coeff}_x} + \frac{(y-y_0)\Omega_y}{\text{coeff}_y} + \frac{(z-z_0)\Omega_z}{\text{coeff}_z} \right] \end{pmatrix}, \tag{4.70}$$

$$\vec{r'}_{SP_N} = \begin{pmatrix} -\frac{\kappa'}{3\sigma_t} \left[ \frac{P_2(\mu)}{\text{coeff}_x} + \frac{1}{\text{coeff}_x} \right] \\ -\frac{\kappa'}{3\sigma_t} \left[ \frac{P_2(\mu)}{\text{coeff}_y} + \frac{1}{\text{coeff}_y} \right] \\ -\frac{\kappa'}{3\sigma_t} \left[ \frac{P_2(\mu)}{\text{coeff}_z} + \frac{1}{\text{coeff}_z} \right] \end{pmatrix}. \tag{4.71}$$

where $\kappa'$ is defined by Eq. (4.28). Then the error in response can be computed with the even-parity unknowns:

$$\delta\overrightarrow{QoI} = \left\langle \vec{r'}_{S_N}, \psi^+_{S_{N'}} \right\rangle - \left\langle \vec{r'}_{SP_N}, \psi^+_{SP_N} \right\rangle. \tag{4.72}$$

#### *4.4.1.4 Boundary Leakage QoI*

For the forward scheme we simply take the response functions given in Section 4.2.4 and use the modified inner product defined by Eq. (4.39) and Eq. (4.41) for $S_N$ and $SP_N$, respectively. The model error in the $QoI$ is computed as:

$$\delta QoI = \lceil r_{S_N}, 2\psi^+_{S_{N'}} - g \rceil - \lceil r_{SP_N}, 2\psi^+_{SP_N} - g \rceil. \tag{4.73}$$

### *4.4.2 Forward Approach: Residual Method*

The *residual* based model error method falls under the forward method category. It is an "intermediate" stage method between the *direct* method and the *adjoint* method. It is still a forward method because it requires a new $S_N$ solve whenever the source condition is changed and does not involve any adjoint calculation. But, as with the *adjoint* method, the *residual* method requires an angular intensity reconstruction scheme. The first step of the *residual* method is to obtain a $S_N$ residual ($\mathcal{R}$) by plugging the $SP_N$ reconstructed angular intensity into the $S_N$ equation:

$$\mathcal{R} = Q - \mathbf{L}\psi_{SP_N \to S_{N'}}, \tag{4.74}$$

where $Q$ is $S_N$ source, and $\mathbf{L}$ is $S_N$ transport operator. Then, the $S_N$ transport equations are solved with the residual as the new source term in order to estimate the error in angular intensities:

$$\delta\psi = \mathbf{L}^{-1}\mathcal{R} = \mathbf{L}^{-1}(Q - \mathbf{L}\psi_{SP_N \to S_{N'}}) = \psi_{S_{N'}} - \psi_{SP_N \to S_{N'}}. \tag{4.75}$$

Finally, taking the inner product between the error in angular intensity and the $S_N$ response function gives us an estimate of the error in the $QoI$.

$$\begin{aligned} \delta QoI = \langle r_{S_N}, \delta\psi \rangle &= \left\langle r_{S_N}, \psi_{S_{N'}} - \psi_{SP_N \to S_{N'}} \right\rangle \\ &= \left\langle r_{S_N}, \psi_{S_{N'}} \right\rangle - \left\langle r_{S_N}, \psi_{SP_N \to S_{N'}} \right\rangle. \end{aligned} \tag{4.76}$$

Comparing Eq. (4.76) with Eq. (4.66), we find that the *residual* method does not yield the same model error between $QoI_{S_{N'}}$ and $QoI_{SP_N}$. Rather, it gives the error between $QoI_{S_{N'}}$ and $QoI_{SP_N \to S_{N'}}$, which is the response computed with the $S_{N'}$

angular intensity reconstructed from the $SP_N$ solution. Because our reconstruction scheme only preserves the $P_0$ moment in 3-D, $\delta QoI$ given by the *residual* method and the *direct* method are generally not consistent. However, as stated earlier in the section, the distance between these two can be readily computed given the $SP_N$ solution:

$$\delta\delta QoI = \delta QoI_{direct} - \delta QoI_{residual} = \langle r_{SP_N}, \psi_{SP_N} \rangle - \left\langle r_{S_N}, \psi_{SP_N \to S_{N'}} \right\rangle, \tag{4.77}$$

where $\psi_{SP_N \to S_{N'}}$ is computed from $\psi_{SP_N}$. As we can see, the only thing required to compute the $\delta\delta QoI$ is $\psi_{SP_N}$, which is already computed in the first place. Therefore, at no additional cost, we can obtain a compensation for the error estimated by the residual method, and make it consistent with the direct method to produce the same model error.

#### *4.4.2.1 Angle-integrated QoI*

Because we are solving the even-parity equations, we need to form the even-parity residual in a way similar to Eq. (4.74):

$$\mathcal{R}^+ = Q^+ - \mathbf{L}^+ \psi^+_{SP_N \to S_{N'}}, \tag{4.78}$$

where $(\mathcal{R}^+, Q^+, \mathbf{L}^+)$ are the even-parity residual, the total source appearing in even-parity equation, and the even-parity transport operator, respectively. Then, the error in $QoI$ can be computed as:

$$\delta QoI = \left\langle r_{S_N}, \mathbf{L}^{+,-1} \mathcal{R}^+ \right\rangle, \tag{4.79}$$

where the response function $r_{S_N}$ is given by Eq. (4.4) and:

$$\mathbf{L}^{+,-1} = (\mathbf{L}^{+})^{-1}. \tag{4.80}$$

We point out that for this angle-integrated $QoI$, we can obtain the correct $\delta QoI$ by using a simpler $\psi^{+}_{SP_N \to S_{N'}}$ that is based on an isotropic recontruction scheme, as shown in Eq. (4.63). It can be justified as follows:

$$\begin{aligned} \delta QoI &= \left\langle r_{S_N}, \mathbf{L}^{+,-1}\mathcal{R}^{+} \right\rangle \\ &= \left\langle r_{S_N}, \mathbf{L}^{+,-1}(Q^{+} - \mathbf{L}^{+}\psi^{+}_{SP_N \to S_{N'}}) \right\rangle \\ &= \left\langle r_{S_N}, \psi^{+}_{S_{N'}} \right\rangle - \left\langle r_{S_N}, \psi^{+}_{SP_N \to S_{N'}} \right\rangle. \end{aligned} \tag{4.81}$$

Replacing $\psi^{+}_{SP_N \to S_{N'}}$ with $\phi_{0,SP_n}/4\pi$, and carrying out the inner product:

$$\delta QoI = \phi_{0,S_{N'}} - \phi_{0,SP_n}, \tag{4.82}$$

which is the same model error in the $QoI$. The same is true for any angle independent response whose angular component is $\vartheta = 1$.

#### *4.4.2.2 Interior Flux QoI: General*

An odd-parity response function expressed as an even-parity response function was given, in the general case, by Eq. (4.12). We re-write it here for an interior flux $QoI$ in 3-D geometry:

$$\vec{r}_{S_N} = \vec{\Omega}\vec{\nabla}\cdot\frac{\kappa\vec{\Omega}}{\sigma_t}. \tag{4.83}$$

With the residual obtained as in Eq. (4.78), the error in response can be computed as:

$$\delta\overrightarrow{QoI} = \left\langle \vec{r}_{S_N}, \mathbf{L}^{+,-1}\mathcal{R}^{+} \right\rangle. \tag{4.84}$$

#### 4.4.2.3 Interior Flux QoI: Cell-averaged

The error in this *QoI* follows the same formalism as in the general interior flux case except that the response function is given by Eq. (4.70).

#### 4.4.2.4 Boundary Leakage QoI

Recall that in computing the boundary leakage response the inner product $\langle \cdot, \cdot \rangle$ is replaced by $\lceil \cdot, \cdot \rceil$. The error in the boundary leakage *QoI* can be computed as:

$$\begin{aligned} \delta QoI &= \left\lceil r_{S_N}, 2\psi^+_{S_{N'}} - g \right\rceil - \left\lceil r_{S_N}, 2\psi^+_{SP_N \to S_{N'}} - g \right\rceil && (4.85) \\ &= 2 \left\lceil r_{S_N}, \psi^+_{S_{N'}} - \psi^+_{SP_N \to S_{N'}} \right\rceil && (4.86) \\ &= 2 \left\lceil r_{S_N}, L^{+,-1}\mathcal{R}^+ \right\rceil, && (4.87) \end{aligned}$$

where the $r_{S_N}$ is defined as in Eq. (4.37) and $\lceil \cdot, \cdot \rceil$ is defined by Eq. (4.39).

### 4.4.3 Adjoint Approach

The *adjoint* method is generally based on the *residual* method, while making use of the property of adjoint operators:

$$\begin{aligned} \delta QoI &= \left\langle r_{S_N}, \mathbf{L}^{-1}\mathcal{R} \right\rangle \\ &= \left\langle \mathbf{L}^{*,-1} r_{S_N}, \mathcal{R} \right\rangle + \Gamma \\ &= \langle \psi^*, \mathcal{R} \rangle + \Gamma, && (4.88) \end{aligned}$$

where $\mathbf{L}^*$ is the adjoint transport operator, $\psi^*$ is the adjoint solution using $r_{S_N}$ as the adjoint source, $\Gamma$ is the boundary correction term due to the integration by parts,

and

$$\mathbf{L}^{*,-1} = (\mathbf{L}^{*})^{-1}, \tag{4.89}$$

$$\mathbf{L}^{*}\psi^{*} = r_{S_N}. \tag{4.90}$$

The advantage of the adjoint-based method is that only one transport solve is required to obtain $\psi^*$. Then, whenever the source condition is changed, one only needs to re-compute the residual $\mathcal{R}$, which requires only a new $SP_N$ solve plus some plain algebraic manipulation, thus very inexpensive.

The general approach for an adjoint method requires setting the adjoint boundary condition to zero for the out-going directions (as seen in Eq. (2.31) and Eq. (2.32), so that forward unknowns do not show up in the boundary correction term $\Gamma$. However, for the boundary leakage response, the response function resides on the boundary and our quantity of interest is buried in $\Gamma$, therefore, in that case, we set the adjoint boundary condition to be equivalent to the boundary response function and adopt a different approach.

As can be seen from the derivation above, the *adjoint* method is mathematically equivalent to the *residual* method. Therefore the error compensation method demonstrated in Eq. (4.77) also applies to the *adjoint* method.

#### *4.4.3.1 Angle-integrated QoI*

Similar to in the *residual* method case, we first need to convert the general scheme into an even-parity scheme to fit our purpose. Replacing the residual and the operator

in Eq. (4.88) with their even-parity counterparts, we obtain:

$$\begin{aligned} \delta QoI &= \left\langle r_{S_N}, (\mathbf{L}^{+})^{-1}\mathcal{R}^{+} \right\rangle \\ &= \left\langle (\mathbf{L}^{+,*})^{-1} r_{S_N}, \mathcal{R}^{+} \right\rangle + \Gamma \\ &= \left\langle \psi^{+,*}, \mathcal{R}^{+} \right\rangle + \Gamma, \end{aligned} \tag{4.91}$$

where the response function $r_{S_N}$ is given by Eq. (4.4). The key is computing $\Gamma$. According to Eq. (4.91):

$$\begin{aligned} \Gamma &= \left\langle r_{S_N}, (\mathbf{L}^{+})^{-1}\mathcal{R}^{+} \right\rangle - \left\langle (\mathbf{L}^{+,*})^{-1} r_{S_N}, \mathcal{R}^{+} \right\rangle \\ &= \left\langle \mathbf{L}^{+,*}\psi^{+,*}, \delta\psi^{+} \right\rangle - \left\langle \psi^{+,*}, \mathbf{L}^{+}\delta\psi^{+} \right\rangle. \end{aligned} \tag{4.92}$$

The idea is to expand $\left\langle \mathbf{L}^{+,*}\psi^{+,*}, \delta\psi^{+} \right\rangle$ and $\left\langle \psi^{+,*}, \mathbf{L}^{+}\delta\psi^{+} \right\rangle$ and compute the difference. However, since we already know that the interaction operator ($\sigma_t$) and the scattering operator ($\sigma_s/4\pi$) are self-adjoint, their corresponding terms are going to cancel out each other in Eq. (4.92). Therefore, we do not account for those terms in our expansion and keep our focus on the streaming term $\left\langle \psi^{+,*}, \vec{\Omega}\cdot\vec{\nabla}\frac{1}{\sigma_t}\vec{\Omega}\cdot\vec{\nabla}\delta\psi^{+} \right\rangle$ and $\left\langle \vec{\Omega}\cdot\vec{\nabla}\frac{1}{\sigma_t}\vec{\Omega}\cdot\vec{\nabla}\delta\psi^{+,*}, \psi^{+} \right\rangle$. Actually the algebra is analogous to Eq. (2.33). The only difference is that this time the forward source is the residual $\mathcal{R}^{+}$ instead of $Q^{+}$, correspondingly the forward solution is the error in the even-parity angular intensity $\delta\psi^{+}$ and the boundary condition for the forward equation now becomes:

$$\delta\psi(\Omega_m) = \delta\psi_m^{+} + \delta\psi_m^{-} = \delta g(\Omega_m) = \delta g_m, \qquad \text{for } \vec{\Omega}_m\cdot\vec{n} < 0, \tag{4.93}$$

$$\delta\psi(-\Omega_m) = \delta\psi_m^{+} - \delta\psi_m^{-} = \delta g(-\Omega_m) = \delta g_m, \qquad \text{for } \vec{\Omega}_m\cdot\vec{n} > 0, \tag{4.94}$$

where $\delta g = g - g_{SP_N \to S_{N'}}$ is the boundary residual. Another change that deserves more discussion is the odd-parity equation for $\delta\psi^-$. Although for an even-parity response the knowledge of $\delta\psi^-$ is not required, the odd-parity equation will help us simplify the expression for $\Gamma$. Recall that $\psi^-_{SP_N \to S_{N'}}$ is reconstructed from $\psi^+_{SP_N \to S_{N'}}$ using the $S_N$ odd-parity equation, we obtain:

$$\psi^-_{SP_N \to S_{N'}} = -\frac{\vec{\Omega}}{\sigma_t} \cdot \vec{\nabla} \psi^+_{SP_N \to S_{N'}} + \frac{Q^-}{\sigma_t}. \tag{4.95}$$

While the true $\psi^-_{S_{N'}}$ is given by:

$$\psi^-_{S_{N'}} = -\frac{\vec{\Omega}}{\sigma_t} \cdot \vec{\nabla} \psi^+_{S_{N'}} + \frac{Q^-}{\sigma_t}. \tag{4.96}$$

Subtracting the reconstruction equation from the $S_N$ odd-parity equation, we get:

$$\begin{aligned} \delta\psi^- &= \psi^-_{S_{N'}} - \psi^-_{SP_N \to S_{N'}} = -\frac{\vec{\Omega}}{\sigma_t} \cdot \vec{\nabla} (\psi^+_{S_{N'}} - \psi^+_{SP_N \to S_{N'}}) \\ &= -\frac{\vec{\Omega}}{\sigma_t} \cdot \vec{\nabla} (\delta\psi^+). \end{aligned} \tag{4.97}$$

Eq. (4.97) is the odd-parity equation for $\delta\psi^-$. Note that there is no odd-parity source in Eq. (4.97).

Applying all the above substitutions to Eq. (2.33), we obtain:

$$
\begin{aligned}
\Gamma &= \left\langle -\vec{\Omega}\cdot\vec{\nabla}\frac{1}{\sigma_t}\vec{\Omega}\cdot\vec{\nabla}\psi^{+,*}, \delta\psi^{+}\right\rangle - \left\langle \psi^{+,*}, -\vec{\Omega}\cdot\vec{\nabla}\frac{1}{\sigma_t}\vec{\Omega}\cdot\vec{\nabla}\delta\psi^{+}\right\rangle \\
&= -\int_{4\pi}\oint \delta\psi^{+}\underbrace{\psi^{-,*}}_{\text{adjoint BC}}\vec{\Omega}\cdot\vec{n}dAd\Omega - \int_{4\pi}\oint \psi^{+,*}\underbrace{\delta\psi^{-}}_{\text{forward BC}}\vec{\Omega}\cdot\vec{n}dAd\Omega \\
&= -\int_{\vec{\Omega}\cdot\vec{n}<0}\oint \delta\psi^{+}\psi^{-,*}\vec{\Omega}\cdot\vec{n}dAd\Omega - \int_{\vec{\Omega}\cdot\vec{n}<0}\oint \psi^{+,*}\delta\psi^{-}\vec{\Omega}\cdot\vec{n}dAd\Omega \\
&\quad -\int_{\vec{\Omega}\cdot\vec{n}>0}\oint \delta\psi^{+}\psi^{-,*}\vec{\Omega}\cdot\vec{n}dAd\Omega - \int_{\vec{\Omega}\cdot\vec{n}>0}\oint \psi^{+,*}\delta\psi^{-}\vec{\Omega}\cdot\vec{n}dAd\Omega \\
&= -\int_{\vec{\Omega}\cdot\vec{n}<0}\oint \delta\psi^{+}\psi^{+,*}\vec{\Omega}\cdot\vec{n}dAd\Omega - \int_{\vec{\Omega}\cdot\vec{n}<0}\oint \psi^{+,*}[\delta g(\Omega)-\delta\psi^{+}]\vec{\Omega}\cdot\vec{n}dAd\Omega \\
&\quad -\int_{\vec{\Omega}\cdot\vec{n}>0}\oint \delta\psi^{+}(-\psi^{+,*})\vec{\Omega}\cdot\vec{n}dAd\Omega - \int_{\vec{\Omega}\cdot\vec{n}>0}\oint \psi^{+,*}[\delta\psi^{+}-\delta g(-\Omega)]\vec{\Omega}\cdot\vec{n}dAd\Omega \\
&= -\int_{\vec{\Omega}\cdot\vec{n}<0}\oint \psi^{+,*}\delta g(\Omega)\vec{\Omega}\cdot\vec{n}dAd\Omega + \int_{\vec{\Omega}\cdot\vec{n}>0}\oint \psi^{+,*}\delta g(-\Omega)\vec{\Omega}\cdot\vec{n}dAd\Omega \\
&= -\int_{\vec{\Omega}\cdot\vec{n}<0}\oint 2\psi^{+,*}\delta g(\Omega)\vec{\Omega}\cdot\vec{n}dAd\Omega. \qquad (4.98)
\end{aligned}
$$

Next we need to look at the $\langle\psi^{+,*},\mathcal{R}^{+}\rangle$ term, where a second order derivative of $\psi^{+}$ is involved and we want to integrate it by parts (I.B.P.) to bring it down to first

order:

$$
\begin{aligned}
\left\langle \psi^{+,*}, \mathcal{R}^{+} \right\rangle &= \left\langle \psi^{+,*}, Q^{+} + \vec{\Omega}\cdot\vec{\nabla}\frac{1}{\sigma_t}\vec{\Omega}\cdot\vec{\nabla}\psi^{+}_{SP_N\to S_{N'}} - \sigma_t\psi^{+}_{SP_N\to S_{N'}} + \frac{\sigma_s}{4\pi}\phi_{SP_N\to S_{N'}} \right\rangle \\
&\quad \text{Neglecting } 0^{th} \text{ \& } 1^{st} \text{ order terms:} \\
&= \left\langle \psi^{+,*}, \quad \vec{\Omega}\cdot\vec{\nabla}\frac{1}{\sigma_t}\vec{\Omega}\cdot\vec{\nabla}\psi^{+}_{SP_N\to S_{N'}} \right\rangle + \cdots \\
&\quad \text{Integrating by part:} \\
&= \int_{4\pi}\oint \psi^{+,*}\frac{1}{\sigma_t}\vec{\Omega}\vec{\nabla}\psi^{+}_{SP_N\to S_{N'}}\vec{\Omega}\cdot\vec{n}dAd\Omega \\
&\quad - \int_{4\pi}\int \frac{1}{\sigma_t}(\vec{\nabla}\cdot\vec{\Omega}\psi^{+,*})(\vec{\nabla}\cdot\vec{\Omega}\psi^{+}_{SP_N\to S_{N'}})dVd\Omega + \cdots \\
&\quad \text{Using } \psi^{-}_{SP_N\to S_{N'}} \text{ equation and neglecting volumetric integrals} \\
&= \int_{4\pi}\oint \psi^{+,*}(-\psi^{-}_{SP_N\to S_{N'}})\vec{\Omega}\cdot\vec{n}dAd\Omega + \int_{4\pi}\oint \psi^{+,*}\left(\frac{Q^{-}}{\sigma_t}\right)\vec{\Omega}\cdot\vec{n}dAd\Omega \\
&\quad + \cdots \\
&\quad \text{Applying Eq. (4.93) and Eq. (4.94), neglecting the } Q^{-} \text{ term} \\
&= -\int_{\vec{\Omega}\cdot\vec{n}<0}\oint \psi^{+,*}[g_{SP_N\to S_{N'}}(\Omega) - \psi^{+}_{SP_N\to S_{N'}}]\vec{\Omega}\cdot\vec{n}dAd\Omega \\
&\quad - \int_{\vec{\Omega}\cdot\vec{n}>0}\oint \psi^{+,*}[\psi^{+}_{SP_N\to S_{N'}} - g_{SP_N\to S_{N'}}(-\Omega)]\vec{\Omega}\cdot\vec{n}dAd\Omega + \cdots \\
&= -\int_{\vec{\Omega}\cdot\vec{n}<0}\oint 2\psi^{+,*}g_{SP_N\to S_{N'}}(\Omega)\vec{\Omega}\cdot\vec{n}dAd\Omega \\
&\quad + \int_{\vec{\Omega}\cdot\vec{n}<0}\oint 2\psi^{+,*}\psi^{+}_{SP_N\to S_{N'}}\vec{\Omega}\cdot\vec{n}dAd\Omega + \cdots \quad . \qquad (4.99)
\end{aligned}
$$

Substituting Eq. (4.98) and Eq. (4.99) into Eq. (4.91), we can finally compute the error in $QoI$ as:

$$
\begin{aligned}
\delta QoI &= \left\langle \psi^{+,*}, \mathcal{R}^{+} \right\rangle + \Gamma \\
&= -\int_{\vec{\Omega}\cdot\vec{n}<0}\oint 2\psi^{+,*}g(\Omega)\vec{\Omega}\cdot\vec{n}dAd\Omega + \int_{\vec{\Omega}\cdot\vec{n}<0}\oint 2\psi^{+,*}\psi^{+}_{SP_N\to S_{N'}}\vec{\Omega}\cdot\vec{n}dAd\Omega \\
&\quad + \cdots \quad . \qquad (4.100)
\end{aligned}
$$

Note that the boundary residual $\delta g$ does not appear this final form so we do not need to deal with it explicitly.

The neglected terms in Eq. (4.100) includes volumetric integrals and terms involving external sources. None of those terms requires the knowledge of the transport solution $\psi$, nor does any of the boundary integrals as shown in Eq. (4.100). Everything required to compute the response is known after solving the adjoint equation and reconstructing the angular intensity $\psi^{+}_{SP_N \to S_{N'}}$. Therefore, whenever the source condition is changed, we only need to recompute the $\psi^{+}_{SP_N \to S_{N'}}$ and no additional transport solves are required to solve for $\psi^{+,*}$ because the adjoint equation is not affected by the forward source.

#### *4.4.3.2 Interior Flux QoI: General*

Since we were able to recast the interior flux response function into an even-parity form, the adjoint method procedure is exactly the same as for the angle-integrated $QoI$. The only difference is that for this $QoI$, the adjoint source, which is also the response function, is replaced by $\vec{r'}_{S_N} = \vec{\Omega}\vec{\nabla}\cdot\frac{\kappa\vec{\Omega}}{\sigma_t}$. Since the adjoint method does not handle vector $QoI$, the response function has to be broken down to its components along each axis directions. For each direction, a full adjoint procedure needs to be carried out using the component along that direction as the adjoint source, to obtain the error in $QoI$ along that direction. In 3-D calculations, for example, the $x, y, z$ components are:

$$r'_x = \vec{\Omega}\cdot\vec{\nabla}\frac{r_x}{\sigma_t}, \tag{4.101}$$

$$r'_y = \vec{\Omega}\cdot\vec{\nabla}\frac{r_y}{\sigma_t}, \tag{4.102}$$

$$r'_z = \vec{\Omega}\cdot\vec{\nabla}\frac{r_z}{\sigma_t}, \tag{4.103}$$

and three independent error calculations are required to obtain the final model error vector.

Because the adjoint source is a compound expression, meaning that it is not a single given function but rather involves differential operation over a combination of two functions, it may need some extra attention and treatment according to the actual spatial dependency of $r$ and $\sigma_t$, especially when discretized. Taking $r'_x$ as an example, we will discuss how to deal with the adjoint source term in the finite element setting.

Generally we do not want to actually take the gradient of $r_x/\sigma_t$ because that will involve numerical differentiation which will give rise to additional error. Fortunately, in the finite element method, we need to test the source term with the basis functions when we assemble the system right-hand-side (RHS) vector, thus giving us a chance to move the gradient operator from $r_x$ to the basis function by integration-by-parts. Suppose that we are testing the adjoint source with an arbitrary basis function $b_i(\underline{\boldsymbol{x}})$:

$$\int \vec{\Omega} \cdot \vec{\nabla} \frac{r_x}{\sigma_t} b_i = -\int \frac{r_x}{\sigma_t} \vec{\Omega} \cdot \vec{\nabla} b_i dV + \cancelto{0}{\oint \frac{r_x}{\sigma_t} b_i \vec{\Omega} \cdot \vec{n} dV}. \tag{4.104}$$

Because $r_x = 0$ on the boundary, the second term vanishes, leaving only the first term. The first term is a straightforward integration, and $r_x$ and $\sigma_t$ can be arbitrary functions. One extreme is that when we want to evaluate the point-wise net flux at $\underline{\boldsymbol{x}}_0$, the $\kappa$ will be a delta function, and the $r_x$ will become:

$$r_x = \Omega_x \cdot \delta(\underline{\boldsymbol{x}} - \underline{\boldsymbol{x}}_0). \tag{4.105}$$

Substituting into the Eq. (4.104), we obtain:

$$\int \vec{\Omega}\cdot\vec{\nabla}\frac{r_x}{\sigma_t}b_i\,dV = -\int \frac{\Omega_x\cdot\delta(\underline{\boldsymbol{x}}-\underline{\boldsymbol{x}}_0)}{\sigma_t}\vec{\Omega}\cdot\vec{\nabla}b_i\,dV = \frac{\Omega_x}{\sigma_t}\vec{\Omega}\cdot\vec{\nabla}b_i\Big|_{\underline{\boldsymbol{x}}=\underline{\boldsymbol{x}}_0}, \qquad (4.106)$$

which means we only need to evaluate the kernel $\frac{\Omega_x}{\sigma_t}\vec{\Omega}\cdot\vec{\nabla}b_i$ at point $\underline{\boldsymbol{x}}_0$.

#### *4.4.3.3 Interior Flux QoI: Cell-averaged*

Similarly to the general interior flux response case, for the cell-averaged version, we can still use exactly the same procedure presented in the angle-integrated *QoI* case. This time the response function is given by Eq. (4.70) in a component-wise form. As in the previous vector *QoI* case, an independent full adjoint analyses is required to obtain the error along each axis-direction.

#### *4.4.3.4 Boundary Leakage QoI*

The *adjoint* method for boundary leakage response is different from all previous responses in that this *QoI* involves an integral over the surface and half the solid angle (only out-going directions). It is not a conventional inner product, therefore, we cannot use the property of adjoint operators to transfer the inverse-transport operation from $\mathcal{R}^+$ to $r_{S_N}$. Furthermore, the boundary leakage response function resides only on the surface, meaning that previous trick of setting the adjoint boundary condition to zero may not be employed in this situation.

To proceed with the *adjoint* approach, we set the adjoint boundary condition to be equivalent to the response function ($r_{S_N}$). From Eq. (4.37) we know that:

$$r_{S_N} = \kappa(\underline{\boldsymbol{x}})\vartheta(\vec{\Omega}) = \kappa\,\vec{\Omega}\cdot\vec{n}, \qquad \vec{\Omega}\cdot\vec{n}\geq 0, \qquad (4.107)$$

where

$$\kappa(\underline{\boldsymbol{x}}) = \begin{cases} 1 & \text{in area of interest} \subset \partial V, \\ 0 & \text{other area} \subset \partial V. \end{cases} \tag{4.108}$$

To construct a boundary condition that is equivalent to Eq. (4.37), we need to multiply the $r_{S_N}$ by a factor of $\frac{1}{\vec{\Omega}\cdot\vec{n}}$, which is the common measure to convert a boundary source into an equivalent boundary condition. As the result our adjoint boundary condition ($g^*$) will be:

$$g^* = \frac{1}{\vec{\Omega}\cdot\vec{n}}\, r_{S_N} = \kappa, \qquad \vec{\Omega}\cdot\vec{n} \geq 0, \tag{4.109}$$

and as a consequence we need to set the adjoint source (the $r_{S_N}$ itself) to be zero. Applying the above boundary condition to the even-parity adjoint form, we get:

$$\psi^{-,*}(\Omega) = g^*(\Omega) - \psi^{+,*}(\Omega), \qquad \vec{\Omega}\cdot\vec{n} > 0, \tag{4.110}$$

$$-\psi^{-,*}(\Omega) = g^*(-\Omega) - \psi^{+,*}(\Omega), \qquad \vec{\Omega}\cdot\vec{n} < 0. \tag{4.111}$$

After the adjoint calculation, the response is not obtained by taking the inner product between the adjoint solution and residual, i.e. $\langle \psi^{+,*}, \mathcal{R}^+ \rangle$. Rather, the response that we are looking for resides in the boundary correction term ($\Gamma$) because of the particular adjoint boundary condition we have just chosen. So let us revisit the algebra of the adjoint approach that leads us to the boundary correction term.

Reworking Eq. (4.98) and applying the new adjoint boundary condition:

$$
\begin{aligned}
\Gamma &= \left\langle -\vec{\Omega}\cdot\vec{\nabla}\frac{1}{\sigma_t}\vec{\Omega}\cdot\vec{\nabla}\psi^{+,*}, \delta\psi^{+}\right\rangle - \left\langle \psi^{+,*}, -\vec{\Omega}\cdot\vec{\nabla}\frac{1}{\sigma_t}\vec{\Omega}\cdot\vec{\nabla}\delta\psi^{+}\right\rangle \\
&= -\int_{4\pi}\oint \delta\psi^{+}\underbrace{\psi^{-,*}}_{\text{adjoint BC}}\vec{\Omega}\cdot\vec{n}dAd\Omega - \int_{4\pi}\oint \psi^{+,*}\underbrace{\delta\psi^{-}}_{\text{forward BC}}\vec{\Omega}\cdot\vec{n}dAd\Omega \\
&= -\int_{\vec{\Omega}\cdot\vec{n}<0}\oint \delta\psi^{+}\psi^{-,*}\vec{\Omega}\cdot\vec{n}dAd\Omega - \int_{\vec{\Omega}\cdot\vec{n}<0}\oint \psi^{+,*}\delta\psi^{-}\vec{\Omega}\cdot\vec{n}dAd\Omega \\
&\quad -\int_{\vec{\Omega}\cdot\vec{n}>0}\oint \delta\psi^{+}\psi^{-,*}\vec{\Omega}\cdot\vec{n}dAd\Omega - \int_{\vec{\Omega}\cdot\vec{n}>0}\oint \psi^{+,*}\delta\psi^{-}\vec{\Omega}\cdot\vec{n}dAd\Omega \\
&= -\int_{\vec{\Omega}\cdot\vec{n}<0}\oint \delta\psi^{+}[-g^{*}(-\Omega)+\psi^{+,*}]\vec{\Omega}\cdot\vec{n}dAd\Omega \\
&\quad -\int_{\vec{\Omega}\cdot\vec{n}<0}\oint \psi^{+,*}[g(\Omega)-\delta\psi^{+}]\vec{\Omega}\cdot\vec{n}dAd\Omega \\
&\quad -\int_{\vec{\Omega}\cdot\vec{n}>0}\oint \delta\psi^{+}[g^{*}(\Omega)-\psi^{+,*}]\vec{\Omega}\cdot\vec{n}dAd\Omega \\
&\quad -\int_{\vec{\Omega}\cdot\vec{n}>0}\oint \psi^{+,*}[\delta\psi^{+}-\delta g(-\Omega)]\vec{\Omega}\cdot\vec{n}dAd\Omega \\
&= \left[-\int_{\vec{\Omega}\cdot\vec{n}<0}\oint \psi^{+,*}\delta g(\Omega)\vec{\Omega}\cdot\vec{n}dAd\Omega + \int_{\vec{\Omega}\cdot\vec{n}>0}\oint \psi^{+,*}\delta g(-\Omega)\vec{\Omega}\cdot\vec{n}dAd\Omega\right] \\
&\quad +\left[\int_{\vec{\Omega}\cdot\vec{n}<0}\oint \delta\psi^{+}g^{*}(-\Omega)\vec{\Omega}\cdot\vec{n}dAd\Omega - \int_{\vec{\Omega}\cdot\vec{n}>0}\oint \delta\psi^{+}g^{*}(\Omega)\vec{\Omega}\cdot\vec{n}dAd\Omega\right] \\
&= -\int_{\vec{\Omega}\cdot\vec{n}<0}\oint 2\psi^{+,*}\delta g(\Omega)\vec{\Omega}\cdot\vec{n}dAd\Omega - \int_{\vec{\Omega}\cdot\vec{n}>0}\oint 2\delta\psi^{+}g^{*}(\Omega)\vec{\Omega}\cdot\vec{n}dAd\Omega.
\end{aligned}
\tag{4.112}
$$

Substitute in the Eq. (4.109), we have:

$$
\Gamma = -2\int_{\vec{\Omega}\cdot\vec{n}<0}\oint \vec{\Omega}\cdot\vec{n}\psi^{+,*}\delta g(\Omega)dAd\Omega - \underbrace{2\int_{\vec{\Omega}\cdot\vec{n}>0}\oint \kappa\vec{\Omega}\cdot\vec{n}\delta\psi^{+}dAd\Omega}_{\delta QoI}. \tag{4.113}
$$

Now we cannot compute the $\Gamma$ using Eq. (4.113) because the second term involves $\delta\psi^{+}$ for the out-going directions, which we do not know. However, by comparing to Eq. (4.87), we find that term is exactly the quantity of interest we are after, the error

in the boundary leakage response ($\delta QoI$). $\Gamma$, on the other hand, can be evaluated by going back to its definition given in Eq. (4.92), and using the fact that $r_{S_N} = 0$ in the problem interior:

$$\begin{aligned} \Gamma &= \cancelto{0}{\left\langle r_{S_N}, (\mathbf{L}^{+})^{-1}\mathcal{R}^{+}\right\rangle} - \left\langle (\mathbf{L}^{+,*})^{-1} r_{S_N}, \mathcal{R}^{+}\right\rangle \\ &= -\left\langle \psi^{+,*}, \mathcal{R}^{+}\right\rangle \end{aligned} \tag{4.114}$$

Combining Eq. (4.114) and Eq. (4.113) to eliminate $\Gamma$ we get:

$$-\left\langle \psi^{+,*}, \mathcal{R}^{+}\right\rangle = -2\int_{\vec{\Omega}\cdot\vec{n}<0} \oint \vec{\Omega}\cdot\vec{n}\psi^{+,*}\delta g(\Omega) dA d\Omega - \delta QoI \tag{4.115}$$

Substituting in Eq. (4.99), we get the final expression for the error in boundary leakage $QoI$:

$$\begin{aligned} \delta QoI &= -\int_{\vec{\Omega}\cdot\vec{n}<0} \oint 2\psi^{+,*} g(\Omega)\vec{\Omega}\cdot\vec{n} dA d\Omega + \int_{\vec{\Omega}\cdot\vec{n}<0} \oint 2\psi^{+,*}\psi^{+}_{SP_N\to S_{N'}}\vec{\Omega}\cdot\vec{n} dA d\Omega \\ &\quad + \cdots \end{aligned} \tag{4.116}$$

which is exactly the same as Eq. (4.100). The neglected terms includes volumetric integrals and terms involving external sources, which does not involve any unknowns after solving for the adjoint solution and computing the residual from the $SP_N$ solution. Hence we can see that all the four kinds of responses share the final expression.

## 4.5 2D Test Results for Comparing the Three Different Methods

To verify that the three error estimation methods discussed above perform as expected and are indeed equivalent, we implemented all the three methods for all the four classes of $QoI$, and carried out a series of numerical tests in 2D geometry. The codes are based on a continuous Galerkin finite element method for the spatial

discretization and are implemented in C++ with the aid of the deal.II finite element library [2]. The geometry we have chosen is a 10 by 10 square with a constant isotropic source distributed over a 6 by 6 centered square, and equipped with vacuum boundary conditions on all four sides. The layout is shown in Fig. 4.2. The material properties (cross sections) are homogeneous across the whole problem domain.

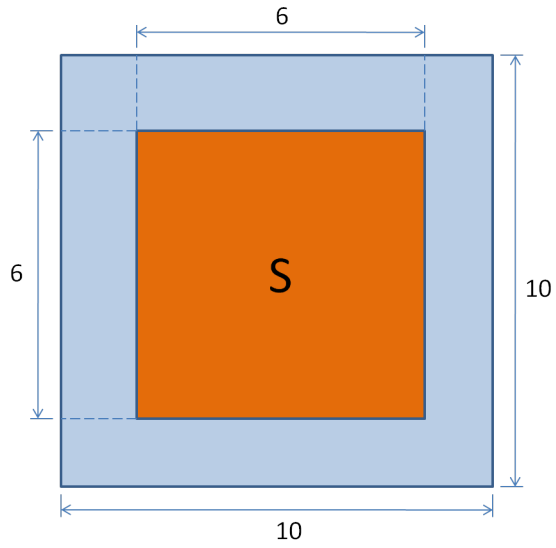


Figure 4.2: 2D test problem layout

For each class fo $QoI$, we ran a sequence of problems approaching the diffusion limit asymptotically, expecting to see the error converge to zero. The problem sequence is generated by first picking a set of $\sigma_{t,0}(= 1)$, scattering ratio $c_0(\equiv \sigma_{s,0}/\sigma_{t,0} = 0.5)$, and source $S_0(= 1)$, then scaling those parameters by $\epsilon$ as commonly done in

neutron transport asymptotic analyses:

$$\sigma_t = \frac{\sigma_{t,0}}{\epsilon} \tag{4.117}$$

$$\sigma_a = \sigma_{a,0}\epsilon \tag{4.118}$$

$$S = S_0\epsilon \tag{4.119}$$

In our experiment we picked $c$ as the control variable and deduce $\epsilon$ from the following relationship:

$$c \equiv \frac{\sigma_s}{\sigma_t} = \frac{\sigma_t - \sigma_a}{\sigma_t} = 1 - (1 - c_0)\epsilon^2 \;\Rightarrow\; \epsilon = \sqrt{\frac{1-c}{1-c_0}} \tag{4.120}$$

A sequence of problems are generated using $c = 0$, 0.5, 0.9, and 0.99. The actual problem parameters are tabulated in Table 4.2:

| $c$ | $\epsilon$ | $\sigma_t$ | $S$ |
|---|---|---|---|
| 0 | 1.414 | 0.707 | 1.414 |
| 0.5 | 1.000 | 1.000 | 1.000 |
| 0.9 | 0.447 | 2.236 | 0.447 |
| 0.99 | 0.141 | 7.071 | 7.071 |

Table 4.2: 2-D test problem parameters

Furthermore, in order to demonstrate the impact of the spatial discretization over the total error, we ran the problems on a sequence of refined meshes, with the number of cells along each side being 10, 20, and 40, respectively.

In our error analyses, in order to use $S_N$ as the high fidelity model we also need to control the angular error by increasing the $S_N$ quadrature order until convergence so that the $S_N$ solution is representative of the true transport solution. $S_N$ saturation

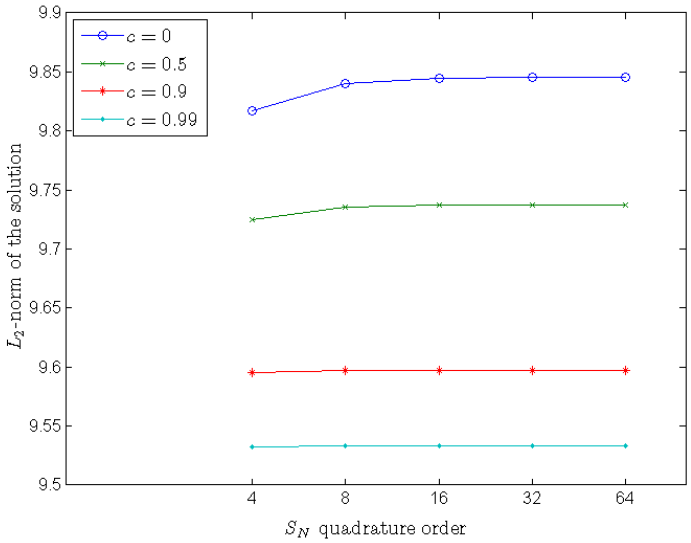


Figure 4.3: $S_N$ saturation test for all scattering ratios of interest

tests were carried out for all 4 scattering ratio scenarios under discussion, with the following $S_N$ orders: $S_4$, $S_8$, $S_{16}$, $S_{32}$, and $S_{64}$. The results are plotted in Fig. 4.3. It shows that the variation in the $L_2$-norm of the solution converges faster as the scattering ratio increases, which is consistent with the fact that a more diffusive medium helps mitigate the ray-effect of the $S_N$ method. At $S_{64}$, the slowest converging $c = 0$ case has saturated to over 99.87%, while the fastest convergeing $c = 0.99$ case has saturated to over 99.99%. Hence for all possible $c$'s, we consider that the angular discretization is virtually saturated at $S_{64}$ and use the $S_{64}$ solution as the high fidelity transport solution. A typical angle-integrated intensity solution for $c = 0.5$ computed with $S_{64}$ quadrature and a $40 \times 40$ mesh is given in Fig. 4.4.

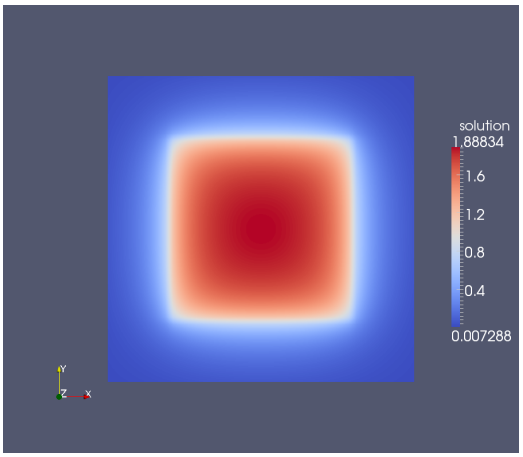


Figure 4.4: Typical angle-integrated intensity solution for $c = 0.5$ and $S_{64}$ on a $40 \times 40$ mesh

### *4.5.1 Angle-integrated QoI*

We chose to evaluate the angle-integrated $QoI$ averaged over a $2 \times 2$ square at the very center of the domain. A typical adjoint solution for $c = 0.5$ computed with $S_{64}$ quadrature and a $40 \times 40$ mesh is given in Fig. 4.5:

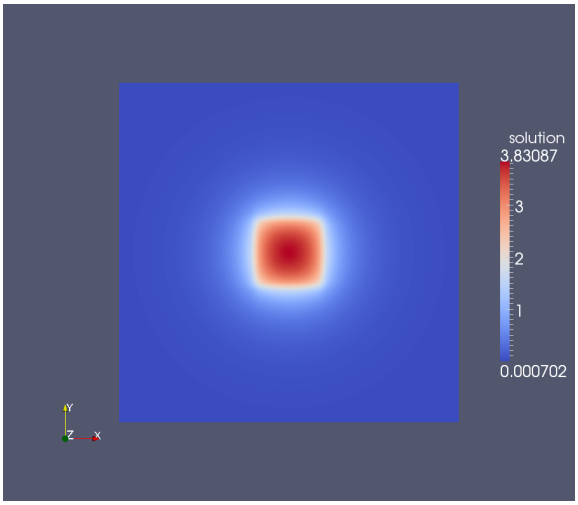


Figure 4.5: Adjoint solution for angle-integrated $QoI$, $c = 0.5$, $S_{64}$, $40 \times 40$ mesh

The relative error computed using the *direct* method ($\delta QoI/QoI$) and the relative difference between the errors computed using the *direct* method and the *adjoint* method ($\delta\delta QoI/\delta QoI$) are tabulated in Table 4.3 to Table 4.5, for various scattering ratios and for the sequence of refined meshes of $10 \times 10$, $20 \times 20$, and $40 \times 40$. Only the comparison between the *direct* method and the *adjoint* method is shown here because the *adjoint* method and the *residual* method are mathematically equivalent. For verification of this equivalence we refer the readers to Appendix D.

| $10 \times 10$ Mesh | $SP_1 - S_{64}$ | | $SP_3 - S_{64}$ | | $SP_7 - S_{64}$ | |
|---|---|---|---|---|---|---|
| | $\frac{\delta QoI}{QoI}\%$ | $\frac{\delta\delta QoI}{\delta QoI}$ | $\frac{\delta QoI}{QoI}\%$ | $\frac{\delta\delta QoI}{\delta QoI}$ | $\frac{\delta QoI}{QoI}\%$ | $\frac{\delta\delta QoI}{\delta QoI}$ |
| $c = 0.0$ | -0.7323 | $-1.45e^{-11}$ | -0.3722 | $5.06e^{-10}$ | 0.0243 | $7.18e^{-09}$ |
| $c = 0.5$ | -0.6803 | $6.25e^{-10}$ | -0.0886 | $5.58e^{-09}$ | 0.0045 | $-4.69e^{-08}$ |
| $c = 0.9$ | -0.2597 | $1.27e^{-10}$ | 0.0030 | $2.20e^{-08}$ | 0.0005 | $3.61e^{-07}$ |
| $c = 0.99$ | -0.0296 | $3.19e^{-09}$ | 0.0002 | $-2.92e^{-07}$ | 0.0002 | $-1.36e^{-06}$ |

Table 4.3: Error in angle-integrated $QoI$ ($10 \times 10$ mesh)
$QoI = QoI_{SP_N}$, $\delta QoI = \delta QoI_{\text{direct}}$, $\delta\delta QoI = \delta QoI_{\text{direct}} - \delta QoI_{\text{adjoint}}$

| $20 \times 20$ Mesh | $SP_1 - S_{64}$ | | $SP_3 - S_{64}$ | | $SP_7 - S_{64}$ | |
|---|---|---|---|---|---|---|
| | $\frac{\delta QoI}{QoI}\%$ | $\frac{\delta\delta QoI}{\delta QoI}$ | $\frac{\delta QoI}{QoI}\%$ | $\frac{\delta\delta QoI}{\delta QoI}$ | $\frac{\delta QoI}{QoI}\%$ | $\frac{\delta\delta QoI}{\delta QoI}$ |
| $c = 0.0$ | -0.6842 | $5.29e^{-10}$ | -0.3578 | $1.40e^{-09}$ | 0.0185 | $-3.71e^{-08}$ |
| $c = 0.5$ | -0.6434 | $-1.41e^{-10}$ | -0.0880 | $-3.65e^{-10}$ | 0.0039 | $-1.33e^{-07}$ |
| $c = 0.9$ | -0.2465 | $9.00e^{-10}$ | 0.0027 | $-1.16e^{-08}$ | 0.0002 | $-1.84e^{-07}$ |
| $c = 0.99$ | -0.0279 | $1.19e^{-08}$ | 0.0002 | $-4.56e^{-07}$ | 0.0001 | $1.05e^{-06}$ |

Table 4.4: Error in angle-integrated $QoI$ ($20 \times 20$ mesh)
$QoI = QoI_{SP_N}$, $\delta QoI = \delta QoI_{\text{direct}}$, $\delta\delta QoI = \delta QoI_{\text{direct}} - \delta QoI_{\text{adjoint}}$

| $40 \times 40$ Mesh | $SP_1 - S_{64}$ | | $SP_3 - S_{64}$ | | $SP_7 - S_{64}$ | |
|---|---|---|---|---|---|---|
| | $\frac{\delta QoI}{QoI}\%$ | $\frac{\delta\delta QoI}{\delta QoI}$ | $\frac{\delta QoI}{QoI}\%$ | $\frac{\delta\delta QoI}{\delta QoI}$ | $\frac{\delta QoI}{QoI}\%$ | $\frac{\delta\delta QoI}{\delta QoI}$ |
| $c = 0.0$ | -0.6738 | $4.98e^{-10}$ | -0.3555 | $6.37e^{-10}$ | 0.0165 | $-6.52e^{-08}$ |
| $c = 0.5$ | -0.6354 | $-1.76e^{-10}$ | -0.0885 | $2.19e^{-09}$ | 0.0032 | $-1.43e^{-07}$ |
| $c = 0.9$ | -0.2437 | $1.22e^{-9}$ | 0.0023 | $-2.23e^{-07}$ | 0.00003 | $1.15e^{-05}$ |
| $c = 0.99$ | -0.0276 | $3.52e^{-09}$ | 0.0002 | $-1.50e^{-06}$ | 0.00004 | $-4.96e^{-06}$ |

Table 4.5: Error in angle-integrated $QoI$ ($40 \times 40$ mesh)
$QoI = QoI_{SP_N}$, $\delta QoI = \delta QoI_{\text{direct}}$, $\delta\delta QoI = \delta QoI_{\text{direct}} - \delta QoI_{\text{adjoint}}$

The results shown in Table 4.3 to Table 4.5 confirmed that the $SP_N$ error decreases as the scattering ratio increases (the problem approaches the diffusion limit) or as the $SP_N$ order increases. The spatial mesh has limited impact on the error calculation, compared to the diffusivity of the problem and the $SP_N$ order. Especially when the $SP_N$ order is lower than 3, the $SP_N$ order model error dominates the spatial discretization error. One important observation is that for all cases the relative difference between the *direct* error and the *adjoint* error is limited by the source iteration and the linear convergence tolerance (both at $1e^{-12}$), which confirms the fact that for angle-integrated responses all the three methods should yield the same error because the angular intensity reconstruction scheme we use is rigorous in the $P_0$-sense and it should preserve the zero-th angular Legendre moment, which is the angle-integrated quantity, of the solution.

### *4.5.2 Interior Flux QoI: General*

For the general interior flux test we chose to evaluate the flux along the positive $x$ direction at the position of (1.9, 4.9). A typical adjoint solution for $c = 0.5$ computed with an $S_{64}$ quadrature and a $40 \times 40$ mesh is given in Fig. 4.5:

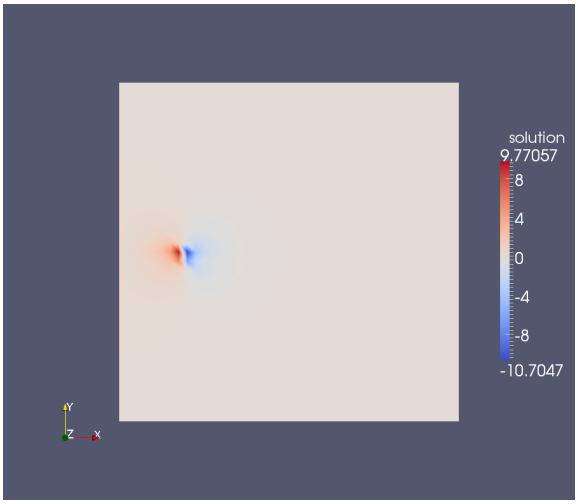


Figure 4.6: Adjoint solution for general interior flux $QoI$, $c = 0.5$, $S_{64}$, $40 \times 40$ mesh

| $10 \times 10$ Mesh | $SP_1 - S_{64}$ | | | $SP_3 - S_{64}$ | | | $SP_7 - S_{64}$ | | |
|---|---|---|---|---|---|---|---|---|---|
| | $\frac{\delta QoI}{QoI}\%$ | $\frac{\delta\delta QoI}{\delta QoI}$ | $\frac{\delta\delta QoI}{\delta QoI}^{\dagger}$ | $\frac{\delta QoI}{QoI}\%$ | $\frac{\delta\delta QoI}{\delta QoI}\%$ | $\frac{\delta\delta QoI}{\delta QoI}^{\dagger}$ | $\frac{\delta QoI}{QoI}\%$ | $\frac{\delta\delta QoI}{\delta QoI}\%$ | $\frac{\delta\delta QoI}{\delta QoI}^{\dagger}$ |
| $c = 0.0$ | -14.779 | $-5.95e^{-12}$ | $2.04e^{-12}$ | -2.389 | -30.162 | $4.64e^{-11}$ | 0.852 | 67.727 | $4.01e^{-11}$ |
| $c = 0.5$ | -8.843 | $-3.74e^{-11}$ | $-2.46e^{-11}$ | -0.847 | -33.361 | $-3.45e^{-10}$ | 0.336 | 55.741 | $-2.08e^{-10}$ |
| $c = 0.9$ | -2.108 | $6.11e^{-11}$ | $1.61e^{-10}$ | 0.056 | 4.095 | $-5.69e^{-09}$ | 0.087 | 5.955 | $-4.97e^{-09}$ |
| $c = 0.99$ | -0.234 | $1.80e^{-09}$ | $1.24e^{-09}$ | 0.021 | -17.645 | $-8.42e^{-09}$ | 0.030 | 12.086 | $-9.26e^{-09}$ |

Table 4.6: Error in general interior flux $QoI$ ($10 \times 10$ mesh)

$QoI = QoI_{SP_N}$, $\delta QoI = \delta QoI_{\text{direct}}$, $\delta\delta QoI = \delta QoI_{\text{direct}} - \delta QoI_{\text{adjoint}}$

| $20 \times 20$ Mesh | $SP_1 - S_{64}$ | | | $SP_3 - S_{64}$ | | | $SP_7 - S_{64}$ | | |
|---|---|---|---|---|---|---|---|---|---|
| | $\frac{\delta QoI}{QoI}\%$ | $\frac{\delta\delta QoI}{\delta QoI}$ | $\frac{\delta\delta QoI}{\delta QoI}^\dagger$ | $\frac{\delta QoI}{QoI}\%$ | $\frac{\delta\delta QoI}{\delta QoI}\%$ | $\frac{\delta\delta QoI}{\delta QoI}^\dagger$ | $\frac{\delta QoI}{QoI}\%$ | $\frac{\delta\delta QoI}{\delta QoI}\%$ | $\frac{\delta\delta QoI}{\delta QoI}^\dagger$ |
| $c = 0.0$ | -15.382 | $1.51e^{-12}$ | $-1.07e^{-11}$ | -3.044 | -4.17 | $1.08e^{-11}$ | -0.484 | 6.25 | $-3.72e^{-10}$ |
| $c = 0.5$ | -9.608 | $4.77e^{-11}$ | $1.14e^{-11}$ | -1.257 | 1.97 | $1.09e^{-10}$ | -0.158 | 60.50 | $-4.28e^{-10}$ |
| $c = 0.9$ | -2.665 | $-1.70e^{-10}$ | $-5.76e^{-11}$ | 0.105 | 37.83 | $-3.21e^{-09}$ | -0.015 | 298.54 | $-4.41e^{-09}$ |
| $c = 0.99$ | -0.334 | $6.13e^{-10}$ | $-2.59e^{-10}$ | 0.007 | 81.89 | $-2.25e^{-08}$ | -0.003 | 181.00 | $-5.29e^{-08}$ |

Table 4.7: Error in general interior flux $QoI$ ($20 \times 20$ mesh)

$QoI = QoI_{SP_N}$, $\delta QoI = \delta QoI_{\text{direct}}$, $\delta\delta QoI = \delta QoI_{\text{direct}} - \delta QoI_{\text{adjoint}}$

| $40 \times 40$ Mesh | $SP_1 - S_{64}$ | | | $SP_3 - S_{64}$ | | | $SP_7 - S_{64}$ | | |
|---|---|---|---|---|---|---|---|---|---|
| | $\frac{\delta QoI}{QoI}\%$ | $\frac{\delta\delta QoI}{\delta QoI}$ | $\frac{\delta\delta QoI}{\delta QoI}^\dagger$ | $\frac{\delta QoI}{QoI}\%$ | $\frac{\delta\delta QoI}{\delta QoI}\%$ | $\frac{\delta\delta QoI}{\delta QoI}^\dagger$ | $\frac{\delta QoI}{QoI}\%$ | $\frac{\delta\delta QoI}{\delta QoI}\%$ | $\frac{\delta\delta QoI}{\delta QoI}^\dagger$ |
| $c = 0.0$ | -15.468 | $-1.31e^{-12}$ | $-1.24e^{-12}$ | -3.678 | 0.4 | $1.47e^{-11}$ | -0.686 | 36.6 | $4.86e^{-11}$ |
| $c = 0.5$ | -9.793 | $1.17e^{-11}$ | $-1.17e^{-11}$ | -1.638 | 6.2 | $-1.45e^{-11}$ | -0.218 | 102.6 | $-5.64e^{-10}$ |
| $c = 0.9$ | -2.825 | $-1.04e^{-10}$ | $-1.26e^{-10}$ | -0.168 | 39.6 | $-1.29e^{-10}$ | -0.008 | 1083.4 | $1.11e^{-08}$ |
| $c = 0.99$ | -0.366 | $7.78e^{-10}$ | $1.84e^{-10}$ | -0.005 | 239.9 | $1.80e^{-08}$ | -0.001 | 1149.1 | $8.07e^{-08}$ |

Table 4.8: Error in general interior flux $QoI$ ($40 \times 40$ mesh)

$QoI = QoI_{SP_N}$, $\delta QoI = \delta QoI_{\text{direct}}$, $\delta\delta QoI = \delta QoI_{\text{direct}} - \delta QoI_{\text{adjoint}}$

The results in Table 4.6 to Table 4.8 also confirm the error trend that we noted in the angle-integrated response case. The major difference from the angle-integrated response is that for the flux response, the *direct* error is no longer the same as the *adjoint* error, because the angular intensity reconstruction scheme we used here (the Hybrid scheme) generally does not preserve the $P_1$ moment of the $SP_N$ solution. The non-trivial $\frac{\delta\delta QoI}{\delta QoI}$ columns represent the relative difference between the errors given

by the *direct* method and by the *adjoint* method. A noteworthy trend is that it actually increases as the $SP_N$ order increases or the problem becomes more diffusive. However, just as discussed earlier in this section, it does not require any significant computational effort to compute a correction for the *adjoint* error. The corrected *adjoint* error is then compared with the *direct* error and the relative difference is given in the $\frac{\delta\delta QoI}{\delta QoI}^{\dagger}$ columns, where all numbers are limited by the source iteration and the linear convergence tolerance used (both at $1e^{-12}$). Therefore, the results manifest that although the *adjoint* method does not give the same error as the *direct* method, a correction can be easily computed to compensate for the difference. One exception, though, is that for $SP_1$ cases, the angular intensity reconstruction is rigorous (see Section 4.3.2), thus the *adjoint* error is essentially the same as the *direct* error even without any correction.

As with the angle-integrated response case, the mesh refinement does not have much impact on the *direct* error. However, the *adjoint* error is much more sensitive to the mesh refinement. That is because the flux response relies on the reconstruction of the $P_1$ moment, which in turn depends on the gradient of $\psi^{+}_{SP_N \to S_{N'}}$.

### *4.5.3 Interior Flux QoI: Cell-averaged*

For the cell-averaged interior flux test we chose to evaluate the flux along the positive $x$ direction averaged within the cell which the spatial point (1.9, 4.9) resides in. A typical adjoint solution for $c = 0.5$ computed with an $S_{64}$ quadrature and a $40 \times 40$ mesh is given in Fig. 4.7:

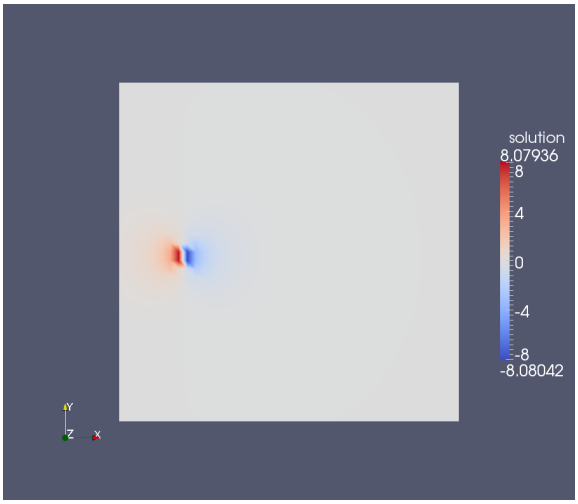


Figure 4.7: Adjoint solution for cell-averaged interior flux $QoI$, $c = 0.5$, $S_{64}$, $40 \times 40$ mesh

| $10 \times 10$ Mesh | $SP_1 - S_{64}$ | | | $SP_3 - S_{64}$ | | | $SP_7 - S_{64}$ | | |
|---|---|---|---|---|---|---|---|---|---|
| | $\frac{\delta QoI}{QoI}\%$ | $\frac{\delta\delta QoI}{\delta QoI}$ | $\frac{\delta\delta QoI}{\delta QoI}^\dagger$ | $\frac{\delta QoI}{QoI}\%$ | $\frac{\delta\delta QoI}{\delta QoI}\%$ | $\frac{\delta\delta QoI}{\delta QoI}^\dagger$ | $\frac{\delta QoI}{QoI}\%$ | $\frac{\delta\delta QoI}{\delta QoI}\%$ | $\frac{\delta\delta QoI}{\delta QoI}^\dagger$ |
| $c = 0.0$ | -14.138 | $4.17e^{-12}$ | $4.17e^{-12}$ | 1.520 | 36.3 | $1.71e^{-10}$ | 0.118 | -833.3 | $-1.84e^{-09}$ |
| $c = 0.5$ | -8.618 | $-3.38e^{-11}$ | $-3.38e^{-11}$ | -0.464 | 102.4 | $-7.82e^{-10}$ | 0.068 | -941.2 | $1.41e^{-09}$ |
| $c = 0.9$ | -2.229 | $-2.78e^{-10}$ | $-2.78e^{-10}$ | -0.017 | 998.2 | $-1.01e^{-08}$ | 0.011 | -1639.6 | $-2.39e^{-09}$ |
| $c = 0.99$ | -0.269 | $-3.86e^{-10}$ | $-3.87e^{-10}$ | -0.010 | 197.0 | $-2.24e^{-08}$ | 0.001 | 1378.2 | $3.14e^{-08}$ |

Table 4.9: Error in cell-averaged interior flux $QoI$ ($10 \times 10$ mesh)

$QoI = QoI_{SP_N}$, $\delta QoI = \delta QoI_{\text{direct}}$, $\delta\delta QoI = \delta QoI_{\text{direct}} - \delta QoI_{\text{adjoint}}$

| $20 \times 20$ Mesh | $SP_1 - S_{64}$ | | | $SP_3 - S_{64}$ | | | $SP_7 - S_{64}$ | | |
|---|---|---|---|---|---|---|---|---|---|
| | $\frac{\delta QoI}{QoI}\%$ | $\frac{\delta\delta QoI}{\delta QoI}$ | $\frac{\delta\delta QoI}{\delta QoI}^\dagger$ | $\frac{\delta QoI}{QoI}\%$ | $\frac{\delta\delta QoI}{\delta QoI}\%$ | $\frac{\delta\delta QoI}{\delta QoI}^\dagger$ | $\frac{\delta QoI}{QoI}\%$ | $\frac{\delta\delta QoI}{\delta QoI}\%$ | $\frac{\delta\delta QoI}{\delta QoI}^\dagger$ |
| $c = 0.0$ | -15.243 | $1.52e^{-12}$ | $1.53e^{-12}$ | -2.868 | 12.6 | $5.56e^{-12}$ | -0.294 | 262.3 | $4.65e^{-10}$ |
| $c = 0.5$ | -9.536 | $-2.40e^{-11}$ | $-2.40e^{-11}$ | -1.161 | 29.8 | $-1.03e^{-10}$ | -0.059 | 886.9 | $-4.95e^{-10}$ |
| $c = 0.9$ | -2.654 | $1.82e^{-10}$ | $1.82e^{-10}$ | -0.087 | 155.1 | $5.90e^{-09}$ | 0.003 | -5691.9 | $-2.16e^{-08}$ |
| $c = 0.99$ | -0.333 | $-5.06e^{-10}$ | $5.06e^{-10}$ | -0.006 | 330.9 | $-3.09e^{-08}$ | -0.001 | 1245.1 | $-1.11e^{-07}$ |

Table 4.10: Error in cell-averaged interior flux $QoI$ ($20 \times 20$ mesh)

$QoI = QoI_{SP_N}$, $\delta QoI = \delta QoI_{\text{direct}}$, $\delta\delta QoI = \delta QoI_{\text{direct}} - \delta QoI_{\text{adjoint}}$

| $40 \times 40$ Mesh | $SP_1 - S_{64}$ | | | $SP_3 - S_{64}$ | | | $SP_7 - S_{64}$ | | |
|---|---|---|---|---|---|---|---|---|---|
| | $\frac{\delta QoI}{QoI}\%$ | $\frac{\delta\delta QoI}{\delta QoI}$ | $\frac{\delta\delta QoI}{\delta QoI}^\dagger$ | $\frac{\delta QoI}{QoI}\%$ | $\frac{\delta\delta QoI}{\delta QoI}\%$ | $\frac{\delta\delta QoI}{\delta QoI}^\dagger$ | $\frac{\delta QoI}{QoI}\%$ | $\frac{\delta\delta QoI}{\delta QoI}\%$ | $\frac{\delta\delta QoI}{\delta QoI}^\dagger$ |
| $c = 0.0$ | -15.448 | $-5.25e^{-12}$ | $-5.25e^{-12}$ | -3.666 | 2.7 | $-1.05e^{-10}$ | -0.673 | 58.6 | $1.27e^{-10}$ |
| $c = 0.5$ | -9.788 | $-1.75e^{-11}$ | $-1.75e^{-11}$ | -1.632 | 9.8 | $-5.17e^{-11}$ | -0.211 | 147.6 | $-8.64e^{-10}$ |
| $c = 0.9$ | -2.825 | $-8.37e^{-11}$ | $-8.36e^{-11}$ | -0.167 | 52.2 | $-6.25e^{-10}$ | -0.007 | 1680.1 | $3.43e^{-08}$ |
| $c = 0.99$ | -0.366 | $2.04e^{-10}$ | $2.04e^{-10}$ | -0.005 | 313.2 | $1.25e^{-08}$ | -0.001 | 1631.2 | $2.43e^{-07}$ |

Table 4.11: Error in cell-averaged interior flux $QoI$ ($40 \times 40$ mesh)

$QoI = QoI_{SP_N}$, $\delta QoI = \delta QoI_{\text{direct}}$, $\delta\delta QoI = \delta QoI_{\text{direct}} - \delta QoI_{\text{adjoint}}$

As can be seen from Table 4.9 to Table 4.11, the error behavior is almost exactly the same as seen in the general interior flux response case.

### *4.5.4 Boundary Leakage QoI*

For the boundary leakage test we chose to evaluate the half-range ($\vec{\Omega} \cdot \vec{n} \geq 0$) leakage through the left boundary ($x = 0$). A typical adjoint solution for $c = 0.5$ computed with an $S_{64}$ quadrature and a $40 \times 40$ mesh is given in Fig. 4.8:

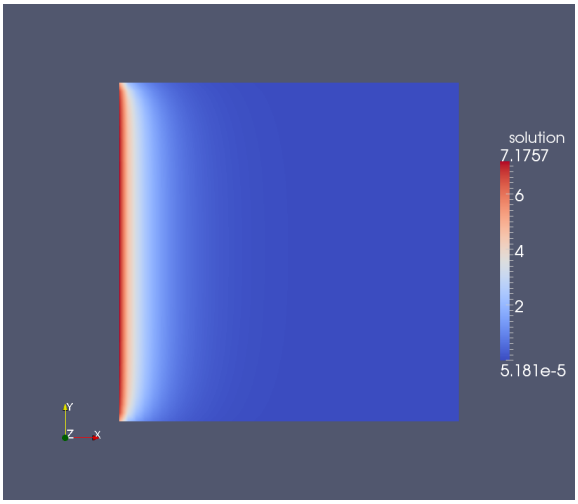


Figure 4.8: Adjoint solution for boundary leakage $QoI$, $c = 0.5$, $S_{64}$, $40 \times 40$ mesh

| $10 \times 10$ | $SP_1 - S_{64}$ | | | $SP_3 - S_{64}$ | | | $SP_7 - S_{64}$ | | |
|---|---|---|---|---|---|---|---|---|---|
| Mesh | $\frac{\delta QoI}{QoI}\%$ | $\frac{\delta\delta QoI}{\delta QoI}$ | $\frac{\delta\delta QoI}{\delta QoI}^{\dagger}$ | $\frac{\delta QoI}{QoI}\%$ | $\frac{\delta\delta QoI}{\delta QoI}\%$ | $\frac{\delta\delta QoI}{\delta QoI}^{\dagger}$ | $\frac{\delta QoI}{QoI}\%$ | $\frac{\delta\delta QoI}{\delta QoI}\%$ | $\frac{\delta\delta QoI}{\delta QoI}^{\dagger}$ |
| $c = 0.0$ | 58.71 | $0.00e^{-00}$ | $8.18e^{-15}$ | 12.507 | 45.56 | $0.00e^{-00}$ | 1.424 | 17.4 | $2.60e^{-11}$ |
| $c = 0.5$ | 41.631 | $5.42e^{-12}$ | $5.42e^{-12}$ | 6.444 | 63.889 | $2.11e^{-11}$ | 0.756 | -1.082 | $-2.55e^{-10}$ |
| $c = 0.9$ | 20.882 | $-2.81e^{-11}$ | $-2.81e^{-11}$ | 3.180 | 38.638 | $-3.08e^{-10}$ | 0.732 | -16.518 | $-1.03e^{-09}$ |
| $c = 0.99$ | 14.925 | $-1.14e^{-10}$ | $-1.14e^{-10}$ | 3.756 | 5.499 | $-3.63e^{-10}$ | 0.992 | -3.774 | $-1.43e^{-09}$ |

Table 4.12: Error in boundary leakage $QoI$ ($10 \times 10$ mesh)

$QoI = QoI_{SP_N}$, $\delta QoI = \delta QoI_{\text{direct}}$, $\delta\delta QoI = \delta QoI_{\text{direct}} - \delta QoI_{\text{adjoint}}$

| $20 \times 20$ Mesh | $SP_1 - S_{64}$ | | | $SP_3 - S_{64}$ | | | $SP_7 - S_{64}$ | | |
|---|---|---|---|---|---|---|---|---|---|
| | $\frac{\delta QoI}{QoI}\%$ | $\frac{\delta\delta QoI}{\delta QoI}$ | $\frac{\delta\delta QoI}{\delta QoI}^\dagger$ | $\frac{\delta QoI}{QoI}\%$ | $\frac{\delta\delta QoI}{\delta QoI}\%$ | $\frac{\delta\delta QoI}{\delta QoI}^\dagger$ | $\frac{\delta QoI}{QoI}\%$ | $\frac{\delta\delta QoI}{\delta QoI}\%$ | $\frac{\delta\delta QoI}{\delta QoI}^\dagger$ |
| $c = 0.0$ | 45.857 | $1.25e^{-16}$ | $5.24e^{-15}$ | 9.756 | 57.414 | $-1.59e^{-11}$ | 2.285 | 40.442 | $5.69e^{-11}$ |
| $c = 0.5$ | 32.415 | $-3.08e^{-12}$ | $-3.08e^{-12}$ | 5.343 | 78.629 | $-2.58e^{-15}$ | 1.591 | 43.070 | $1.68e^{-11}$ |
| $c = 0.9$ | 17.165 | $1.51e^{-11}$ | $1.52e^{-11}$ | 3.657 | 57.772 | $-3.77e^{-11}$ | 1.016 | 41.729 | $-1.62e^{-11}$ |
| $c = 0.99$ | 14.313 | $-4.03e^{-11}$ | $-4.03e^{-11}$ | 3.916 | 27.928 | $-1.22e^{-10}$ | 1.030 | 16.905 | $-5.46e^{-10}$ |

Table 4.13: Error in boundary leakage $QoI$ ($20 \times 20$ mesh)

$QoI = QoI_{SP_N}$, $\delta QoI = \delta QoI_{\text{direct}}$, $\delta\delta QoI = \delta QoI_{\text{direct}} - \delta QoI_{\text{adjoint}}$

| $40 \times 40$ Mesh | $SP_1 - S_{64}$ | | | $SP_3 - S_{64}$ | | | $SP_7 - S_{64}$ | | |
|---|---|---|---|---|---|---|---|---|---|
| | $\frac{\delta QoI}{QoI}\%$ | $\frac{\delta\delta QoI}{\delta QoI}$ | $\frac{\delta\delta QoI}{\delta QoI}^\dagger$ | $\frac{\delta QoI}{QoI}\%$ | $\frac{\delta\delta QoI}{\delta QoI}\%$ | $\frac{\delta\delta QoI}{\delta QoI}^\dagger$ | $\frac{\delta QoI}{QoI}\%$ | $\frac{\delta\delta QoI}{\delta QoI}\%$ | $\frac{\delta\delta QoI}{\delta QoI}^\dagger$ |
| $c = 0.0$ | 44.062 | $-2.53e^{-16}$ | $2.03e^{-15}$ | 9.358 | 59.472 | $2.23e^{-11}$ | 2.350 | 46.925 | $-1.34e^{-11}$ |
| $c = 0.5$ | 41.631 | $5.42e^{-12}$ | $5.42e^{-12}$ | 6.444 | 63.889 | $2.11e^{-11}$ | 0.756 | -1.082 | $-2.55e^{-10}$ |
| $c = 0.9$ | 16.609 | $-5.10e^{-12}$ | $-5.09e^{-12}$ | 3.661 | 61.280 | $-4.12e^{-11}$ | 1.072 | 50.950 | $2.64e^{-10}$ |
| $c = 0.99$ | 14.118 | $-1.92e^{-11}$ | $-1.92e^{-11}$ | 3.980 | 36.633 | $-8.37e^{-11}$ | 1.051 | 29.170 | $-2.81e^{-10}$ |

Table 4.14: Error in boundary leakage $QoI$ ($40 \times 40$ mesh)

$QoI = QoI_{SP_N}$, $\delta QoI = \delta QoI_{\text{direct}}$, $\delta\delta QoI = \delta QoI_{\text{direct}} - \delta QoI_{\text{adjoint}}$

The results in Table 4.12 to Table 4.14 show the general trend of the relative error in the $QoI$: it decreases as the problem becomes more diffusive or the $SP_N$ order increases (but one should not expect the $SP_N$ solution to converge to the true transport solution generally). Another trend that is different from the flux response case is that when the mesh is sufficiently refined, the relative difference between the *direct* error and the *adjoint* error decreases as the $SP_N$ order goes up or as the problem

gets more and more diffusive. That is because the reconstruction reference direction $\vec{k}$ is aligned with the boundary normal $\vec{n}$, the angular intensity reconstruction at the boundary is rigorous. The relative difference we are seeing here is the numerical angular integration error due to the inadequate angular quadrature order. The $S_{64}$ solution already has a very high $S_N$ quadrature order, so the $S_N$ response is relatively accurate. As the $SP_N$ order increases, the $SP_N$ angular integration becomes more accurate, thus reducing the difference between these two. The explanation on the diffusivity's impact on the relative difference is that as the scattering gets more prominent, the angular intensity on the boundary will become more isotropic, thus lowering the required quadrature order to obtain a relatively accurate angular integration involved in computing the $QoI$.

### *4.5.5 Summary*

The numerical experiment results presented above verified that all the three model error estimation methods produce the same results. According to the specific type of quantity of interest that is being evaluated, an easily computable error correction may be needed (for interior flux and boundary leakage QoI's). The results also confirmed that the hybrid reconstruction scheme for the angular intensity preserves the $P_0$ moment but not any higher moments. Results using a hierarchy of meshes showed that the spatial mesh refinement has a limited impact on the error estimates, meaning that the model error dominates the numerical error resulting from the spatial discretization.

# 5. APPLYING THE METHODOLOGIES TO THE PECOS PROBLEM

One of the goals of this research was to quantify the model error between $SP_N$ and $S_N$ in evaluating the photon energy flux into the ablator surface, which in turn contributes to the ablation rate of the heatshield material. In this section, we apply the methodologies that we developed in the previous sections to the PECOS problem, using given material properties and a grey (energy-integrated) radiation model, to obtain model error estimates that are relevant to the vehicle re-entry problem.

## 5.1 Problem Statement and Numerical Treatment of the Input Nodal Data

The geometry and the mesh are given by our partners at the PECOS center at University of Texas - Austin. The geometry models a bowl shaped air region above which sits the ablator (the ablator itself is not represented but the contour of the ablator forms the hot boundary surface of the air region). Away from the ablator interface is a shock layer and a rarefied air region. The mesh is a structured one and extremely refined at the ablator interface and moderately refined at the shock layer. A cutaway view of the mesh is given in Fig. 5.1.

The absorption cross section and material temperature profiles are also given together with the mesh, from a hydrodynamic calculation performed without radiation. There is no scattering in this problem and the cross section is energy-averaged. The material properties are defined on mesh vertices. Our transport codes allow for spatially varying material properties, thus in forming the system matrices in the Finite Element method we linearly interpolate these data at spatial quadrature points within each cell. A black-body incident flux boundary condition is derived from the nodal temperature data and applied at the ablator-to-air interface, while vacuum boundary conditions are employed everywhere else. Zoom-in plots of ab-

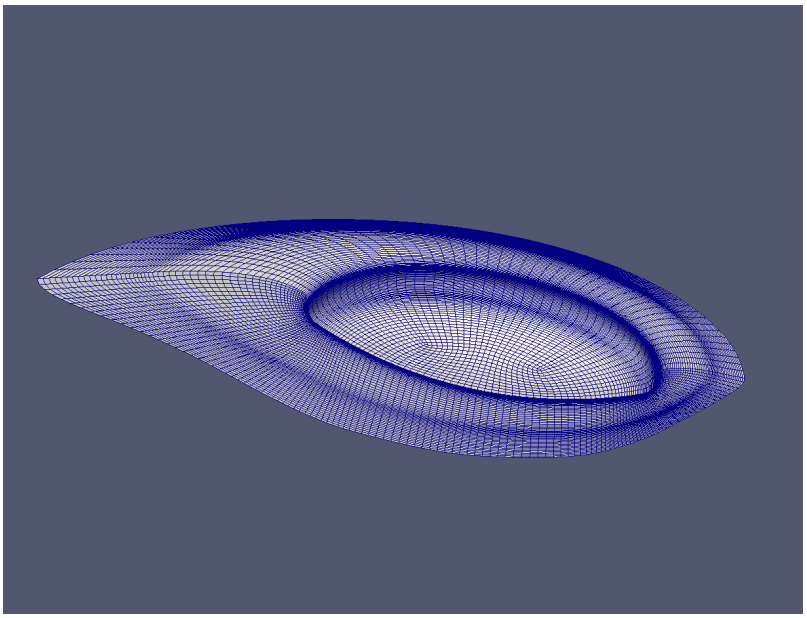

Figure 5.1: Cutaway view of the PECOS mesh

sorption cross section and temperature profiles are given in Fig. 5.2 and Fig. 5.3 respectively. It can be seen that the cross section peaks in the blow-off region right next to the ablator interface. This region is only 2 millimeters thick and consists of mainly heatshield material that has much a higher opacity than the surrounding air. The temperature peaks at the shock layer, as expected. The region between the blow-off region and the shock layer has both moderate cross section and temperature and is thus referred to as the intermediate region. The rarefied air region, which is below the shock layer, is almost vacuum.

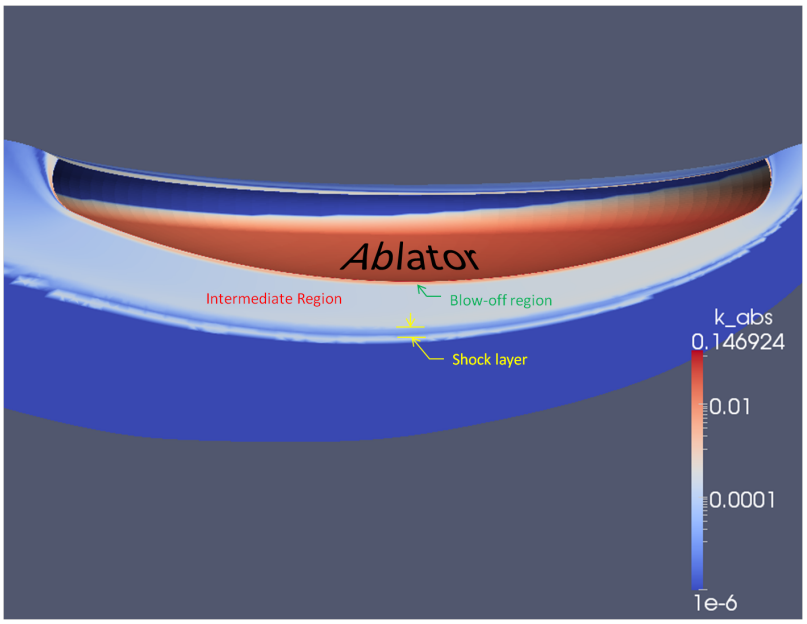


Figure 5.2: Absorption cross section profile ($m^{-1}$), zoomed in.

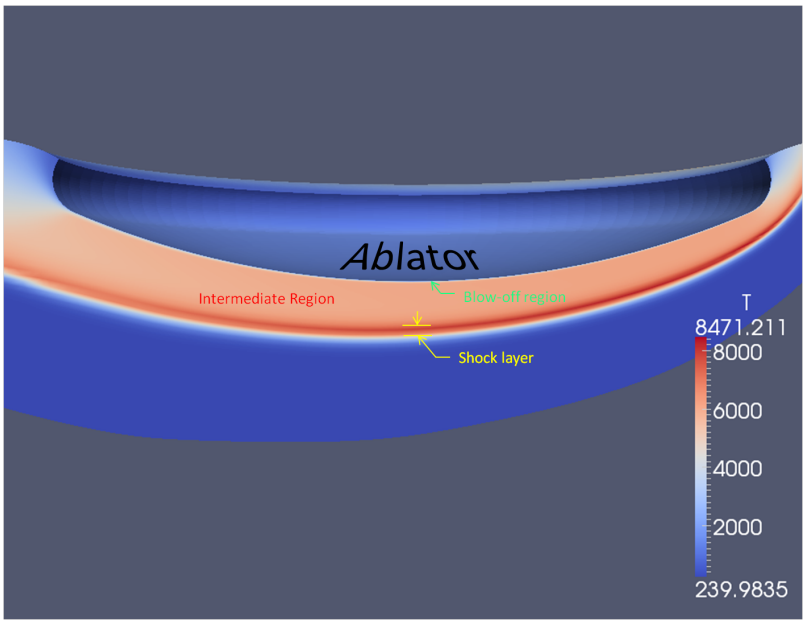


Figure 5.3: Material temperature profile ($K$), zoomed in.

Combining the absorption cross section data and the temperature data, the effective energy- and angle-integrated black-body source can be computed as $S = \sigma_a acT^4$. The effective source is plotted in Fig. 5.4. Note that the effective source also peaks in the blow-off region as the cross section does. In comparison, the source within the shock layer is much less significant.

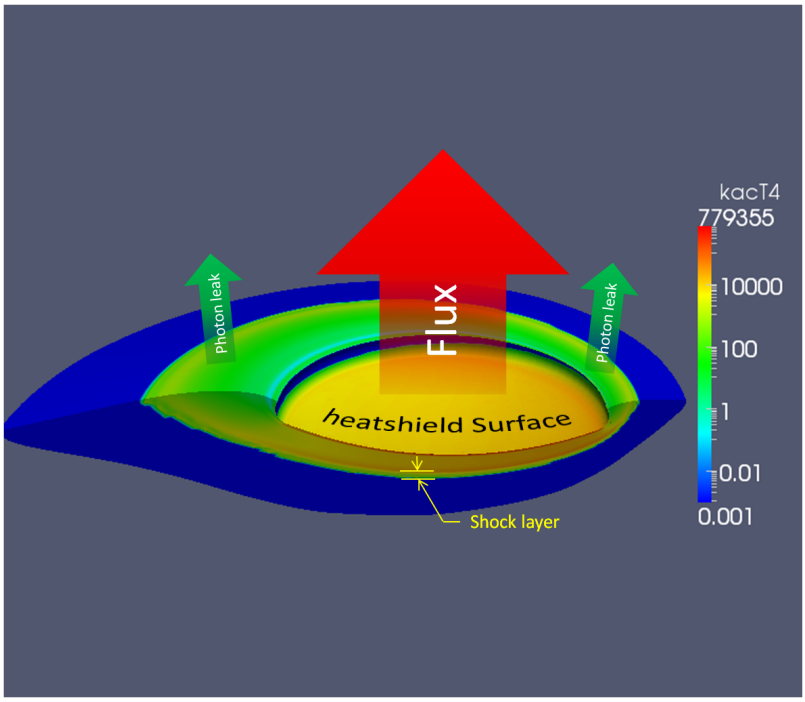


Figure 5.4: Effective black-body source profile ($W/m^3$)

An important approximation that we made during the calculation is the use of pseudo cross section, $\sigma_{a,\min}$. As can be seen from Fig. 5.2, the original PECOS cross section is extremely small. The $\sigma_a$ is on the order of $10^{-6}m^{-1}$ in the rarefied air region, and is only about $10^{-4}m^{-1}$ even in the shock layer. The diameter of the heatshield is 5 meters. Therefore the whole problem is significantly less than 1/1000 mean-free-path (m.f.p.) thick. Due to the presence of the $1/\sigma_a$ in the streaming

terms of both the canonical $SP_N$ and Even-parity $S_N$ forms, their Finite Element system matrices will become extremely ill-conditioned when the original $\sigma_a$ is used. To circumvent this difficulty, we used a pseudo cross section (in the streaming term only), $\sigma_{a,\min}$, which is defined to be much larger than the original cross section, but still small enough to have negligible impact on the solution. The justification for the effectiveness of the pseudo cross section is that the whole system is optically very thin, a perturbation around the 1/1000 m.f.p.'s thickness should not change the fact that most photons will leak out the system without being absorbed.

## 5.2 Results for Boundary Leakage $QoI$

For a sample calculation, we choose the $\sigma_{a,\min} = 0.001m^{-1}$, and we choose to compare $SP_3$ against $S_8$. Higher $S_N$ order is possible but the computation is very expensive and is not really worth it since the angular discretization is already converged to 15% (see Section 5.3) at $S_4$ in the sense of the primary quantity of interest, the half-range flux into the heat-shield. The angle-integrated solution for the canonical $SP_3$, the even-parity $S_8$, and the adjoint even-parity $S_8$ is given in Fig. 5.5, Fig. 5.6, and Fig. 5.7, respectively. Notice how flat the $SP_N$ solution is and how different it is from the $S_N$ solution. That is because the $SP_N$ solution tends to diffuse along any direction and the small cross section will exaggerate the unphysical diffusion even more, spreading out the solution all over the problem domain. Also be aware that pseudo-color scales through out the figures are not the same.

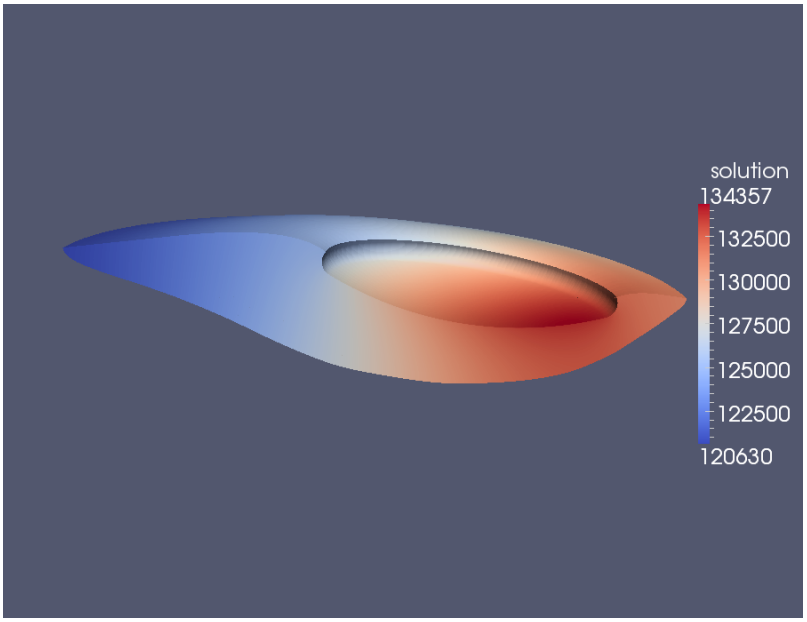


Figure 5.5: Angle-integrated intensity computed with $SP_3$ $(W/m^2)$

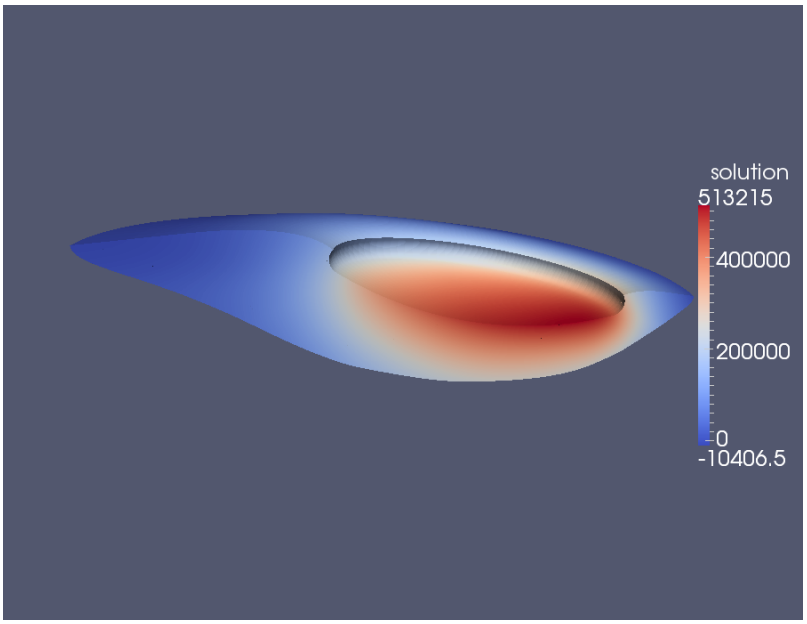


Figure 5.6: Angle-integrated intensity computed with Even-parity $S_8$ $(W/m^2)$

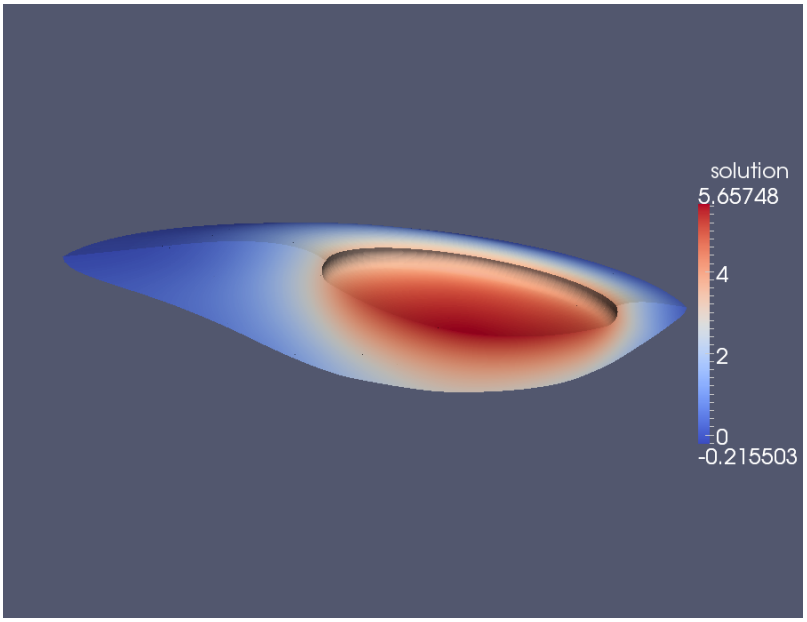


Figure 5.7: Angle-integrated intensity computed with adjoint Even-parity $S_8$ $(W/m^2)$

The $QoI$ is the surface-integrated half-range radiation energy flux into the ablator. It falls in the category of boundary leakage $QoI$ that discussed in Section 4.2.4. Applying the model error estimation we developed in Section 4, we obtain the error values listed in Table 5.1:

| | |
|---|---|
| $SP_3$ half-range flux (direct computation): | $-4.032 \times 10^6\ W$ |
| $S_8$ half-range flux (direct computation): | $-6.276 \times 10^5\ W$ |
| $SP_3$ vs. $S_8$ error computed using the *residual* method: | $3.429 \times 10^6\ W$ |
| $SP_3$ vs. $S_8$ error computed using the *adjoint* method: | $3.429 \times 10^6\ W$ |
| $SP_3 \rightarrow S_8$ reconstruction error : | $-2.408 \times 10^4\ W$ |

Table 5.1: $SP_3$ vs. $S_8$ PECOS calculation : half-range flux into the heat-shield

It can be seen that the *residual* method and the *adjoint* method yield exactly the same error estimate for the $QoI$ of half-range flux. After accounting for the reconstruction error, the total error estimation is exactly the same as the difference between the $SP_N$ solution and the $S_N$ solution, as computed directly. One important observation, however, is that both the canonical $SP_N$ and Even-parity $S_N$ $QoI$ results are unphysical. The numbers are computed as negative but physically they should be non-negative. This indicates that the canonical $SP_N$ and Even-parity $S_N$ may not be suitable for such an optically thin problem. In Section 5.3 convergence tests are carried out for both methods and the results are compared with the Least-squares $S_N$ method, which is compatible with voids.

## 5.3 Convergence Issue with Canonical $SP_N$ and Even-parity $S_N$

Three types of convergence tests, namely, angular convergence test, $p$ convergence test, and $\sigma_{a,\min}$ convergence test are carried out for the three different transport approximates: the canonical $SP_N$, the Even-parity $S_N$, and the Least-squares $S_N$.

### *5.3.1 Convergence Tests for Canonical $SP_N$*

#### *5.3.1.1 Angular Convergence Test*

The purpose of the angular convergence test is to see how the angular discretization affects the solution. For $SP_N$ the angular resolution is indicated by the $SP_N$ order. For this test, the $SP_3$ solution is compared with the $SP_7$ solution. The results given in Fig. 5.8 and Table 5.2 show that the angular discretization converged down to less than 1.3% at $SP_3$, in the sense of the total flux into the heat-shield. Therefore latter calculations are performed with $SP_3$ to save computational time without loosing much angular resolution.

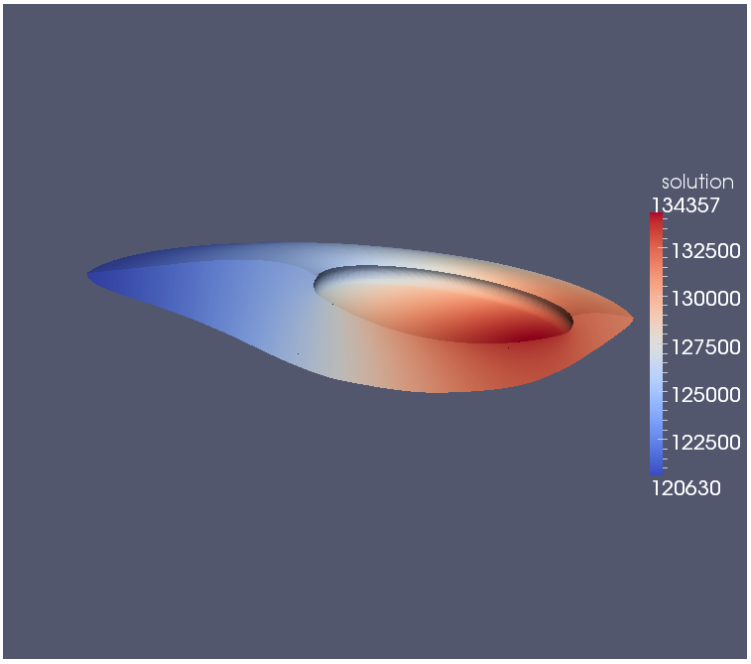


(a) Angle-integrated intensity ($W/m^2$), $SP_3$ Q1, $\sigma_{a,\min} = 0.001m^{-1}$

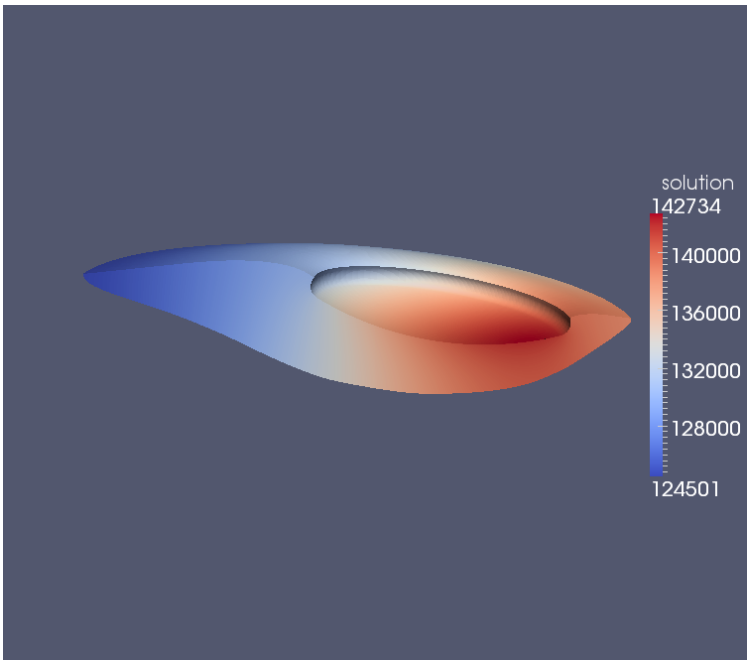


(b) Angle-integrated intensity ($W/m^2$), $SP_7$ Q1, $\sigma_{a,\min} = 0.001m^{-1}$

Figure 5.8: $SP_N$ angular convergence test

| | |
|---|---|
| $SP_3$ Q1 half-range flux: | $-4.032 \times 10^6\ W$ |
| $SP_7$ Q1 half-range flux: | $-3.981 \times 10^5\ W$ |

Table 5.2: $SP_N$ angular convergence : half-range flux into the heat-shield

#### *5.3.1.2 p- Convergence Test*

The $p$ convergence test varies the polynomial order employed in the Finite Element method, to see how the solution changes correspondingly. Due to the same computational cost concern, only Q1 (tri-linear) and Q2 (quadratic) finite element polynomials are tested. The results given in Fig. 5.9 and Table 5.3 show that the angle integrated intensity is converged to 1.4% at Q1, which is expected for such a highly refined mesh.

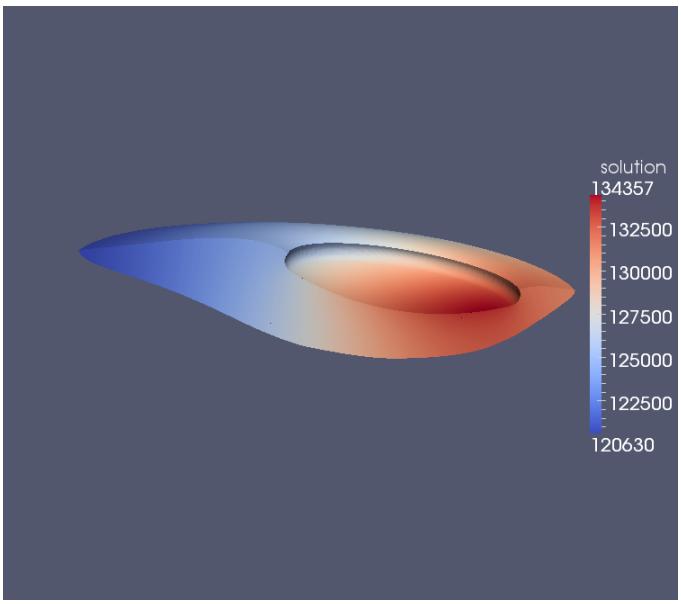


(a) [Angle-integrated intensity ($W/m^2$), $SP_3$ Q1, $\sigma_{a,\min} = 0.001m^{-1}$

Figure 5.9: $SP_N$ $p$- convergence test

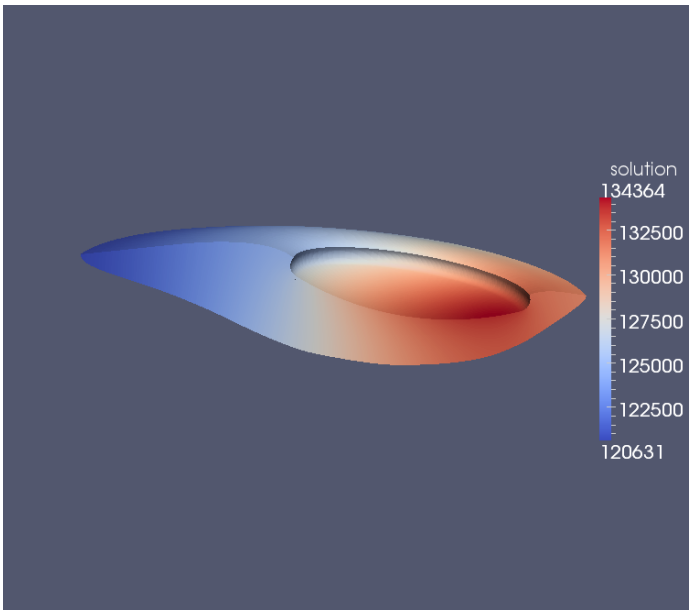


(b) Angle-integrated intensity ($W/m^2$), $SP_3$ Q2, $\sigma_{a,\min} = 0.001m^{-1}$

Figure 5.9: Continued

| | |
|---|---|
| $SP_3$ Q1 half-range flux: | $-4.032 \times 10^6\ W$ |
| $SP_3$ Q2 half-range flux: | $-4.090 \times 10^5\ W$ |

Table 5.3: $SP_N$ $p$- convergence : half-range flux into heat-shield

#### *5.3.1.3 $\sigma_{a,min}$ Convergence Test*

The $\sigma_{a,\min}$ convergence test demonstrates the solution's sensitivity to the choice of $\sigma_{a,\min}$. In the case of the $SP_N$, we tested it for $\sigma_{a,\min} = 0.01m^{-1}$, $0.001m^{-1}$, $0.0001m^{-1}$ and $0.00001m^{-1}$. The results are given in Fig. 5.10 and Table 5.4. Although the results exhibit some sensitivity to the $\sigma_{a,\min}$ when $\sigma_{a,\min} > 0.01m^{-1}$, the

half-range flux is reasonably converged as the $\sigma_{a,\min}$ is further reduced. The convergence is expected for pseudo cross section method. It indicates that the convergence behavior is acceptable for the $SP_N$ method for such a void dominant problem. However, because the $SP_N$ method is diffusing the solution along every direction, it can not produce a meaningful solution for this particular problem and leads to a unphysical negative half-range flux. The verdict is that the $SP_N$ method shows physical insensitivity to the small $\sigma_{a,\min}$, but its solution is wrong.

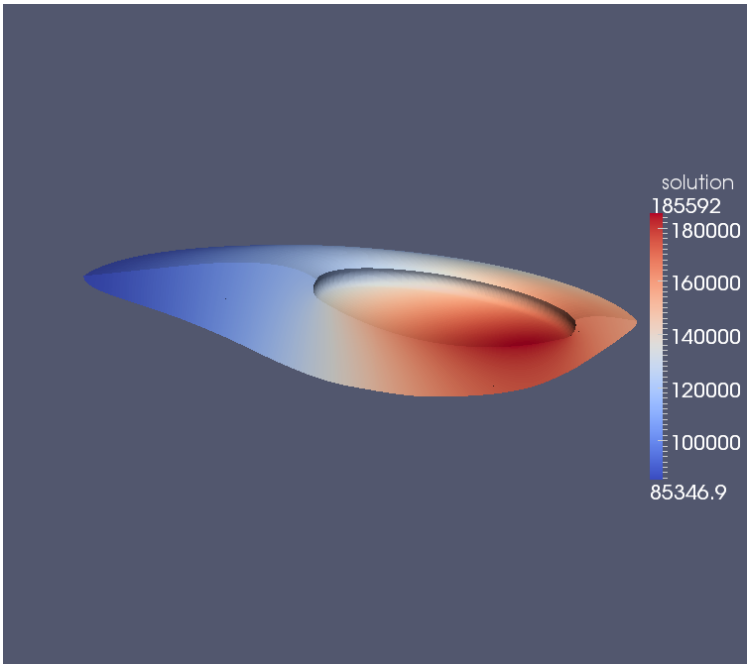


(a) Angle-integrated intensity ($W/m^2$), $SP_3$ Q1,

$\sigma_{a,\min} = 0.01m^{-1}$

Figure 5.10: $SP_N$ $\sigma_{a,\min}$ convergence test

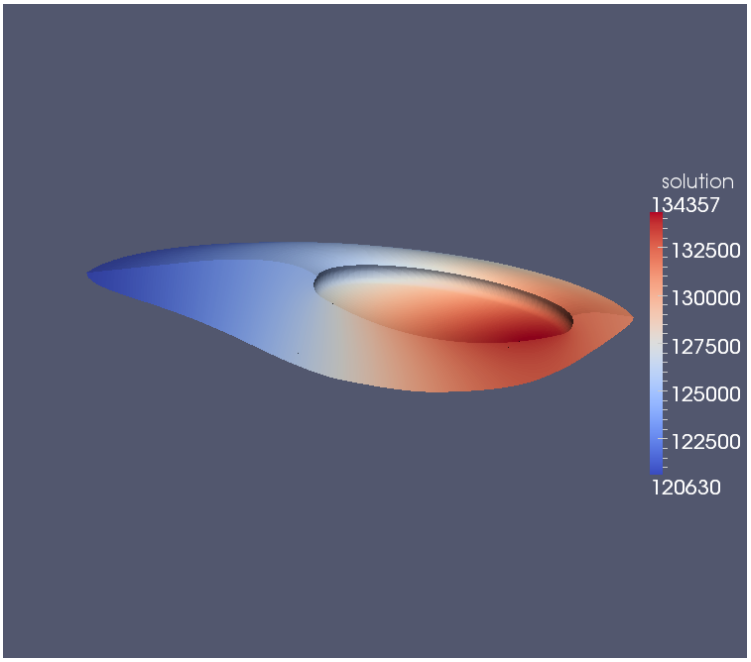


(b) Angle-integrated intensity ($W/m^2$), $SP_3$ Q1,

$\sigma_{a,\min} = 0.001m^{-1}$

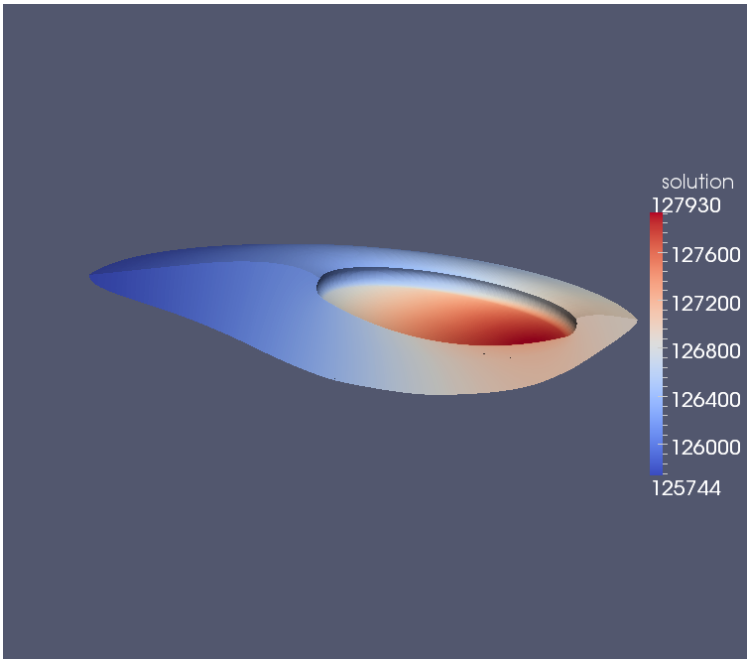


(c) Angle-integrated intensity ($W/m^2$), $SP_3$ Q1,

$\sigma_{a,\min} = 0.0001m^{-1}$

Figure 5.10: Continued

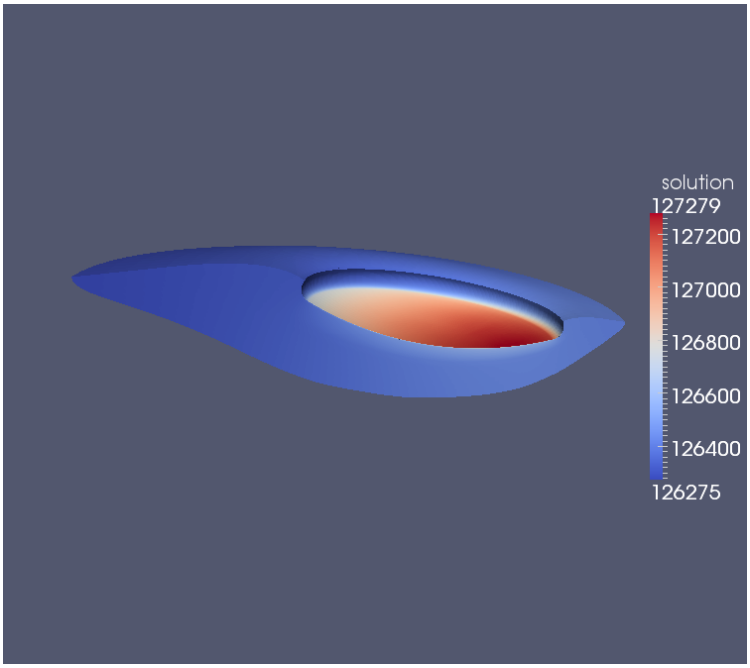


(d) Angle-integrated intensity ($W/m^2$), $SP_3$ Q1,

$\sigma_{a,\min} = 0.00001m^{-1}$

Figure 5.10: Continued

| | | | |
|---|---|---|---|
| $SP_3$ Q1, | $\sigma_{a,\min} = 0.01m^{-1}$, | half-range flux: | $-3.741 \times 10^6\ W$ |
| $SP_3$ Q1, | $\sigma_{a,\min} = 0.001m^{-1}$, | half-range flux: | $-4.032 \times 10^6\ W$ |
| $SP_3$ Q1, | $\sigma_{a,\min} = 0.0001m^{-1}$, | half-range flux: | $-4.066 \times 10^6\ W$ |
| $SP_3$ Q1, | $\sigma_{a,\min} = 0.00001m^{-1}$, | half-range flux: | $-4.070 \times 10^5\ W$ |

Table 5.4: $SP_N$ $\sigma_{a,\min}$ convergence : half-range flux into the heat-shield

### *5.3.2 Convergence Tests for Even-parity $S_N$*

#### *5.3.2.1 Angular Convergence Test*

The $S_4$ solution is compared with the $S_8$ solution. Similarly to the $SP_N$ case, the results given in Fig. 5.11 and Table 5.5 show that the angular discretization converged down to 15% at $S_4$, in the sense of the half-range flux into the heatshield.

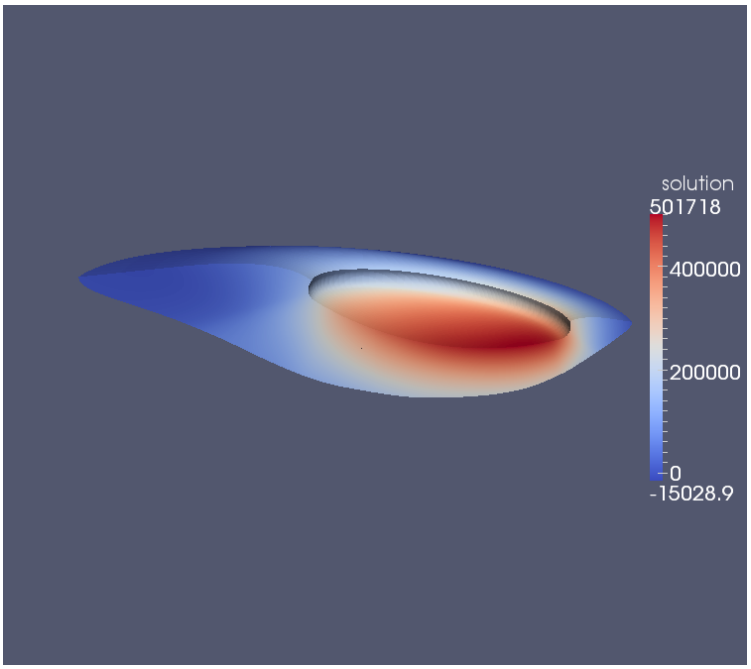


(a) Angle-integrated intensity ($W/m^2$), $S_4$ Q1, $\sigma_{a,\min} = 0.001 m^{-1}$

Figure 5.11: Even-parity $S_N$ angular convergence test

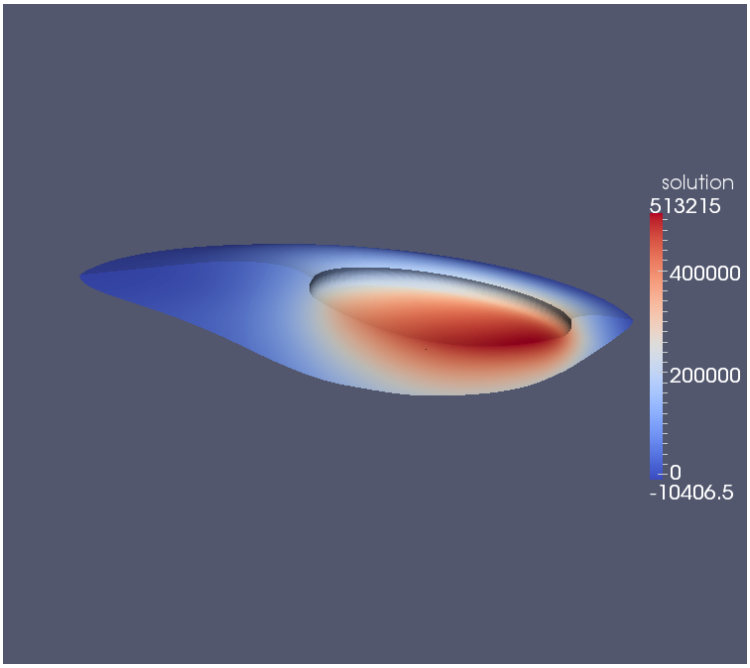


(b) Angle-integrated intensity ($W/m^2$), $S_8$ Q1,

$\sigma_{a,\min} = 0.001 m^{-1}$

Figure 5.11: Continued

| | |
|---|---|
| $S_4$ Q1 half-range flux: | $-7.210 \times 10^5\ W$ |
| $S_8$ Q1 half-range flux: | $-6.276 \times 10^5\ W$ |

Table 5.5: Even-parity $S_N$ angular convergence : half-range flux into the heat-shield

#### *5.3.2.2 p- Convergence Test*

As before, only Q1 and Q2 finite element polynomials are tested. However, the results given in Fig. 5.12 and Table 5.6 show that the negativity in Q2 solution is

reduced by 85% compared to Q1. It indicates that the Even-parity $S_N$ method is far from convergence at the Q1 level. Such a slow $p$ convergence is generally not expected over such a refined mesh.

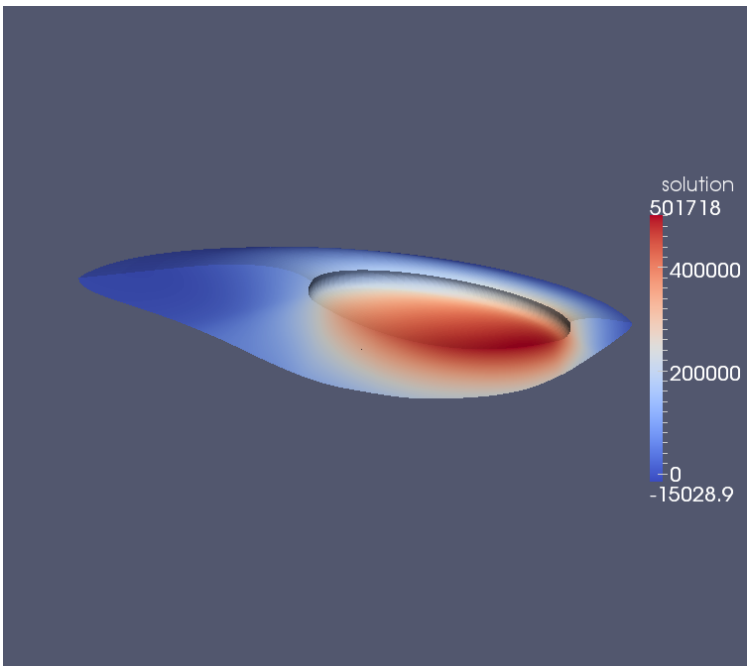


(a) Angle-integrated intensity ($W/m^2$), $S_4$ Q1,

$\sigma_{a,\min} = 0.001 m^{-1}$

Figure 5.12: Even-parity $S_N$ $p$- convergence test

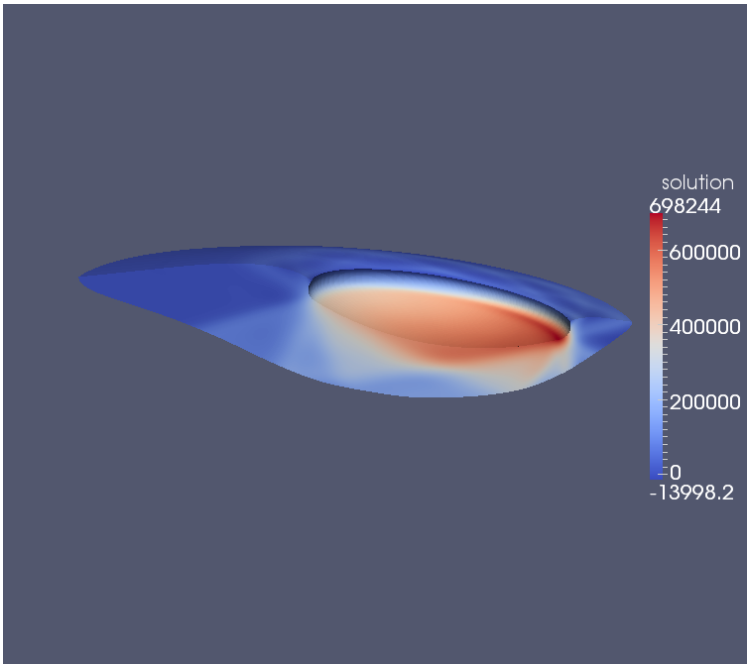


(b) Angle-integrated intensity ($W/m^2$), $S_4$ Q2,

$\sigma_{a,\min} = 0.001 m^{-1}$

Figure 5.12: Continued

| | |
|---|---|
| $S_4$ Q1 half-range flux: | $-7.210 \times 10^5\ W$ |
| $S_4$ Q2 half-range flux: | $-1.107 \times 10^5\ W$ |

Table 5.6: Even-parity $S_N$ $p$- convergence : half-range flux into the heat-shield

### 5.3.2.3 $\sigma_{a,min}$ Convergence Test

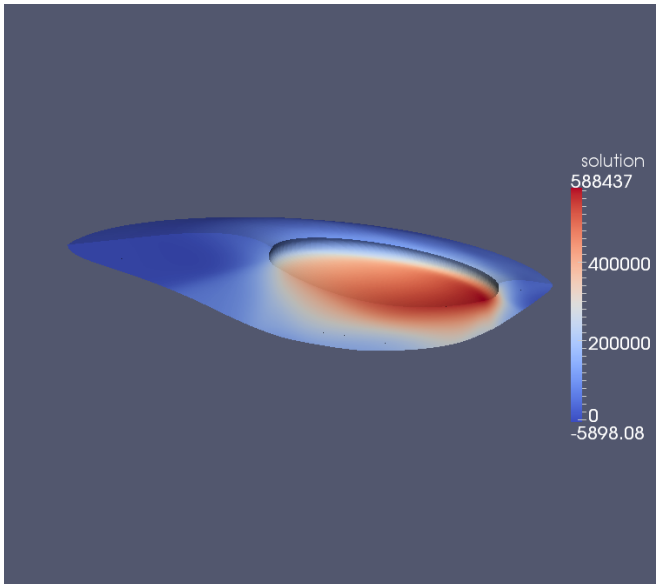


(a) Angle-integrated intensity ($W/m^2$), $S_4$ Q1, $\sigma_{a,\min} = 0.01m^{-1}$

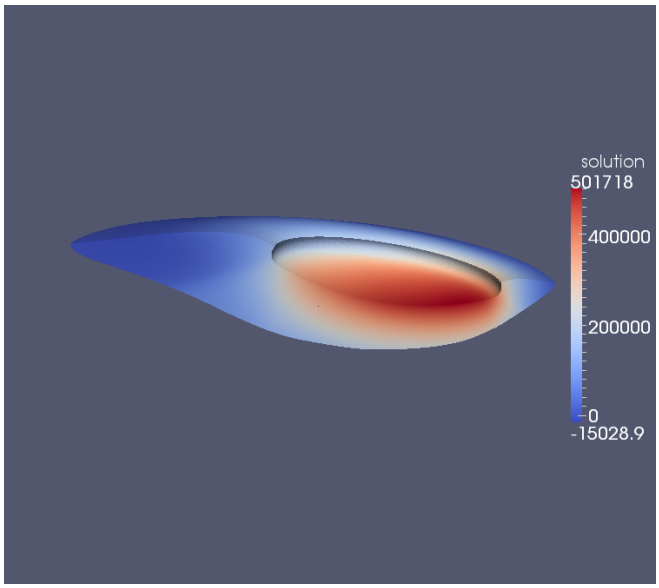


(b) Angle-integrated intensity ($W/m^2$), $S_4$ Q1, $\sigma_{a,\min} = 0.001m^{-1}$

Figure 5.13: Even-parity $S_N$ $\sigma_{a,\min}$ convergence test

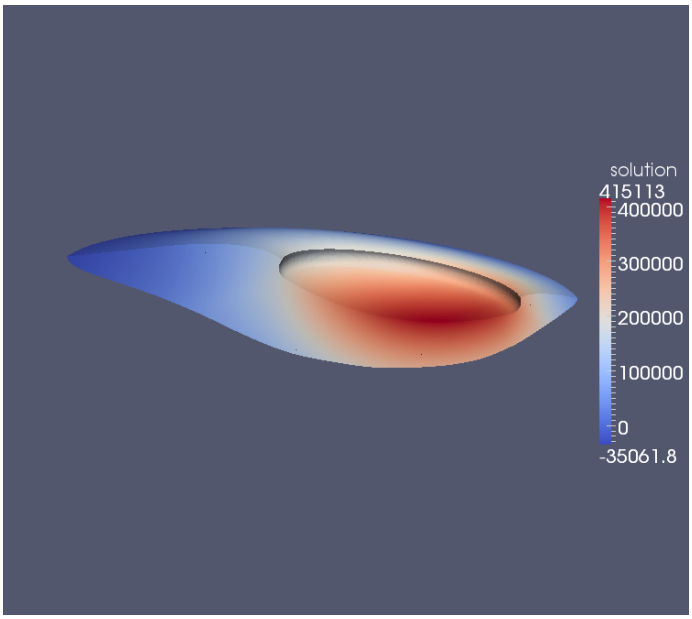


(c) Angle-integrated intensity ($W/m^2$), $S_4$ Q1,

$\sigma_{a,\min} = 0.0001m^{-1}$

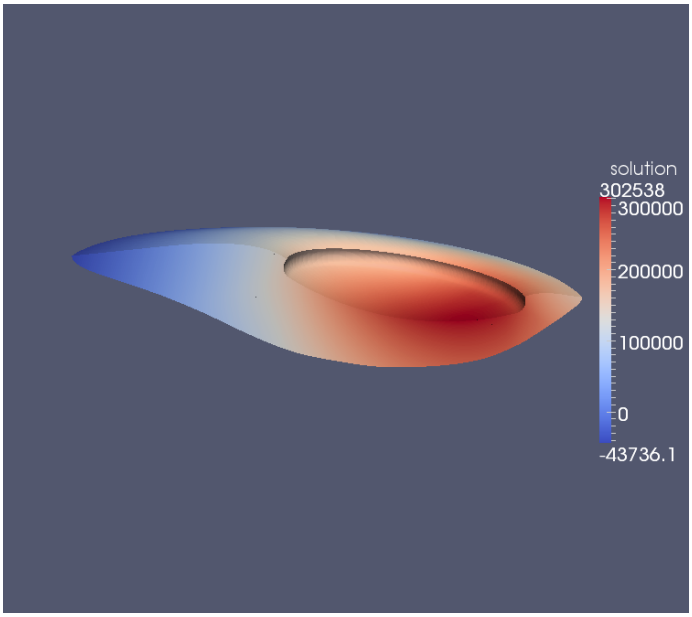


(d) Angle-integrated intensity ($W/m^2$), $S_4$ Q1,

$\sigma_{a,\min} = 0.00001m^{-1}$

Figure 5.13: Continued

| | | | |
|---|---|---|---|
| $S_4$ Q1, | $\sigma_{a,\min} = 0.01m^{-1}$, | half-range flux: | $-3.012 \times 10^5\ W$ |
| $S_4$ Q1, | $\sigma_{a,\min} = 0.001m^{-1}$, | half-range flux: | $-7.210 \times 10^5\ W$ |
| $S_4$ Q1, | $\sigma_{a,\min} = 0.0001m^{-1}$, | half-range flux: | $-1.426 \times 10^6\ W$ |
| $S_4$ Q1, | $\sigma_{a,\min} = 0.00001m^{-1}$, | half-range flux: | $-3.738 \times 10^6\ W$ |

Table 5.7: Even-parity $S_N$ $\sigma_{a,\min}$ convergence : half-range flux into the heat-shield

As before, we carried out tests with $\sigma_{a,\min} = 0.01m^{-1}$, $0.001m^{-1}$, $0.0001m^{-1}$ and $0.00001m^{-1}$. The results are given in Fig. 5.13 and Table 5.7. Much worse than the $SP_N$ case, the Even-parity $S_N$ results almost show no trend of convergence at all as the $\sigma_{a,\min}$ decreases. Both $p$ convergence and $\sigma_{a,\min}$ convergence tests show that the Even-parity $S_N$ method has serious convergence issues for near void problems and its solution cannot be trusted. The strong sensitivity to $\sigma_{a,\min}$ is non-physical.

### *5.3.3 Convergence Tests for Least-squares $S_N$*

#### *5.3.3.1 Angular Convergence Test*

Similar as before, the $S_4$ solution is compared with the $S_8$ solution. The results given in Fig. 5.14 and Table 5.8 show that the angular discretization converged to 4.3% at $S_4$.

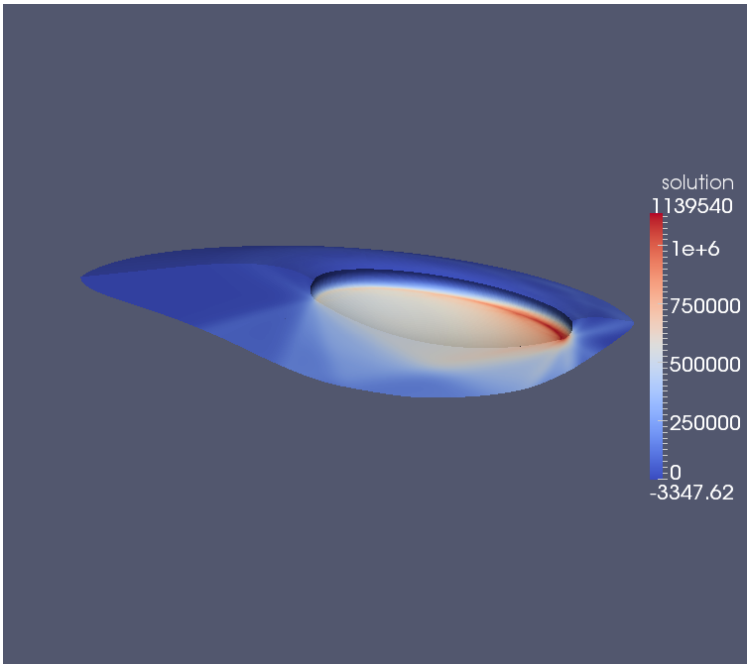


(e) Angle-integrated intensity ($W/m^2$), $S_4$ Q1,

$\sigma_{a,\min} = 0.001m^{-1}$

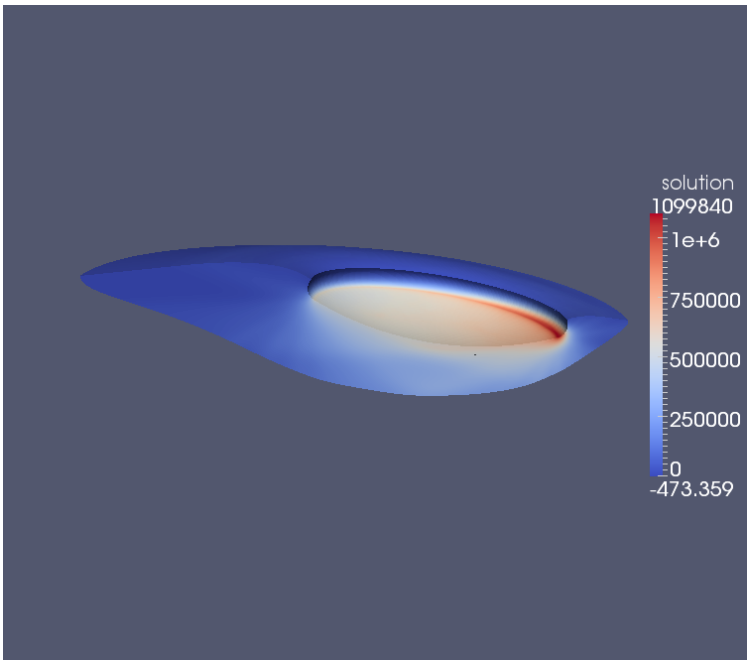


(f) Angle-integrated intensity ($W/m^2$), $S_8$ Q1,

$\sigma_{a,\min} = 0.001m^{-1}$

Figure 5.14: Least-squares $S_N$ angular convergence Test

| | |
|---|---|
| $S_4$ Q1 half-range flux: | $3.141 \times 10^5\ W$ |
| $S_8$ Q1 half-range flux: | $3.013 \times 10^5\ W$ |

Table 5.8: Least-squares $S_N$ angular convergence : half-range flux into the heat-shield

#### *5.3.3.2 p- Convergence Test*

Again, Q1 and Q2 finite element polynomials are tested. The results given in Fig. 5.15 and Table 5.9 show that the half-rang flux converged to around 16% at Q1. It is a significant improvement over the Even-parity $S_N$ results in that the half-range flux is positive and the change in the half-range flux is reasonable.

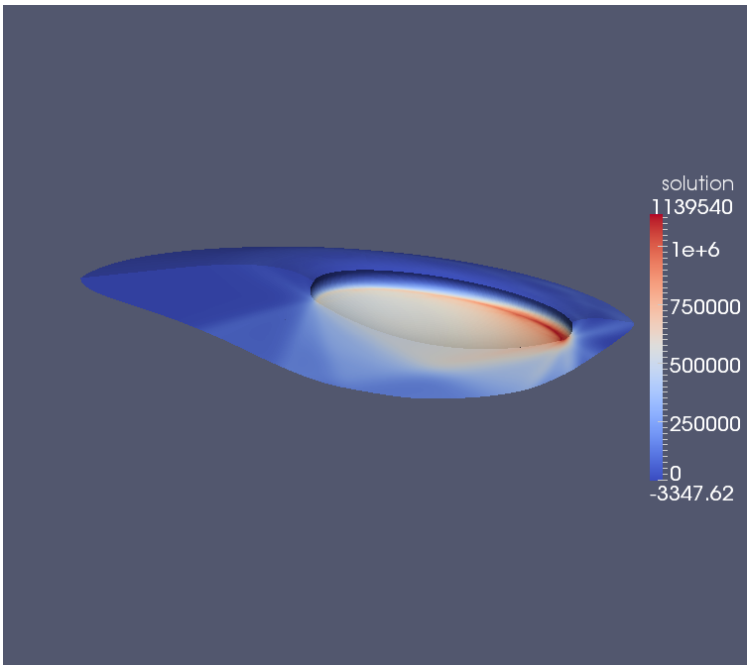


(a) Angle-integrated intensity ($W/m^2$), $S_4$ Q1,

$\sigma_{a,\min} = 0.001 m^{-1}$

Figure 5.15: Least-squares $S_N$ $p$- convergence test

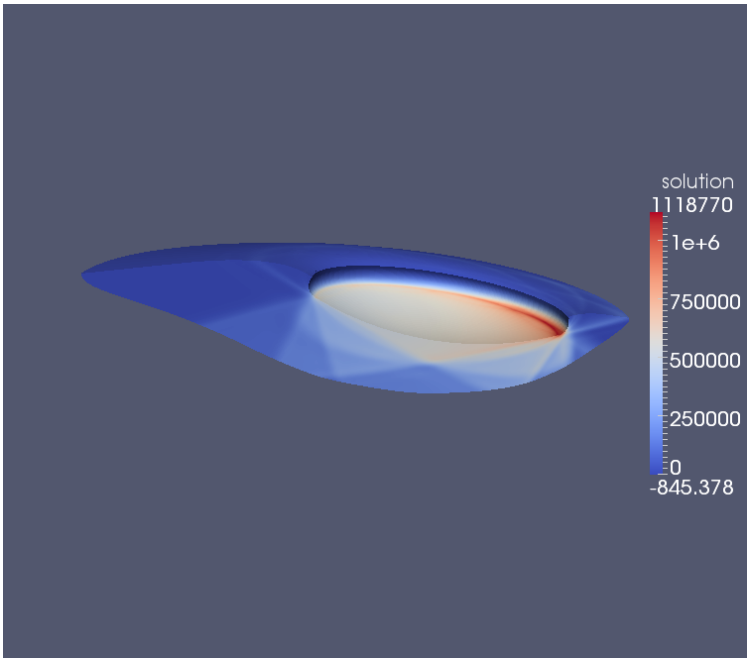


(b) Angle-integrated intensity ($W/m^2$), $S_4$ Q2,

$\sigma_{a,\min} = 0.001m^{-1}$

Figure 5.15: Continued

| | |
|---|---|
| $S_4$ Q1 half-range flux: | $3.141 \times 10^5\ W$ |
| $S_4$ Q2 half-range flux: | $2.702 \times 10^5\ W$ |

Table 5.9: Least-squares $S_N$ $p$- convergence : half-range flux into the heat-shield

#### *5.3.3.3 $\sigma_{a,min}$ Convergence Test*

For the Least-squares $S_N$ method, we use the $\sigma_{a,\min}$ for only the absorption terms in the operator $\mathbf{L}$ and $\mathbf{L}^*$, defined in Eq. (2.36) and Eq. (2.37) respectively. Thanks to

the absence of the $1/\sigma_a$ in the streaming term, we can employ the true PECOS cross section in our calculation because this does not result in an ill-conditioned system matrix. Therefore, for the case of smallest $\sigma_{a,\min}$ we choose to set the $\sigma_a$ to be the original PECOS cross section, which is equal to set the $\sigma_{a,\min}$ to $0m^{-1}$.

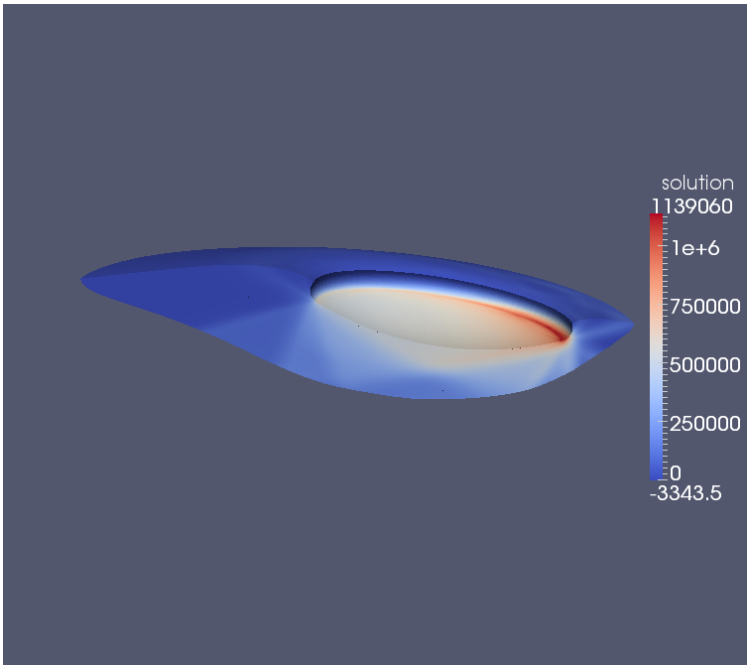


(a) Angle-integrated intensity ($W/m^2$), $S_4$ Q1,
$\sigma_{a,\min} = 0.01m^{-1}$

Figure 5.16: Least-squares $S_N$ $\sigma_{a,\min}$ convergence test

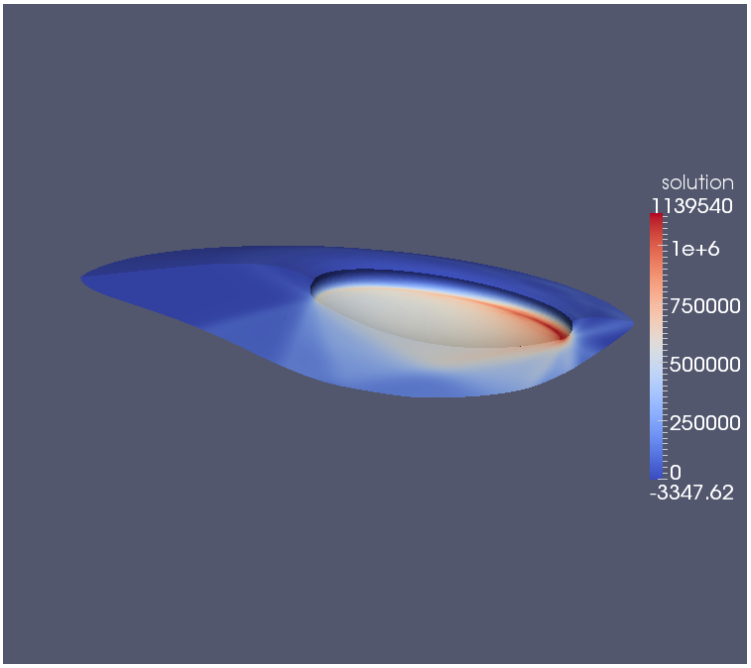


(b) Angle-integrated intensity ($W/m^2$), $S_4$ Q1,

$\sigma_{a,\min} = 0.001m^{-1}$

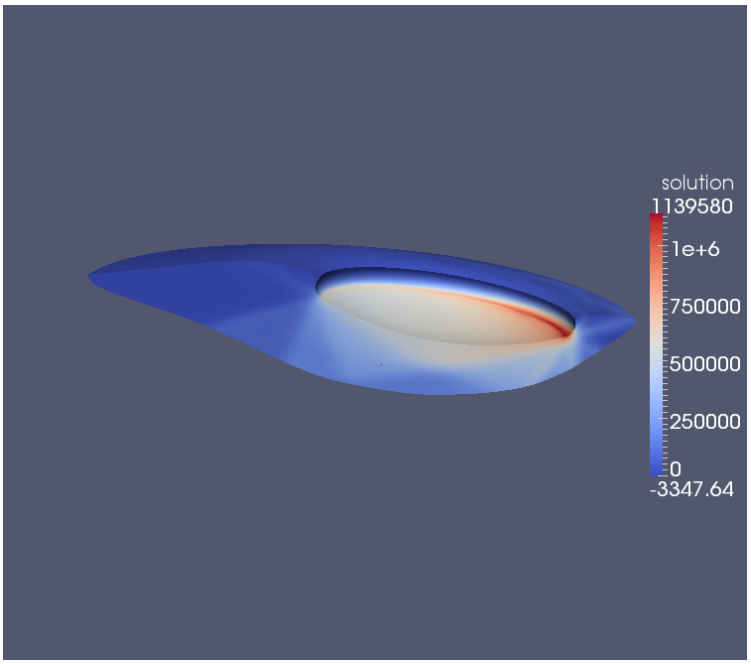


(c) Angle-integrated intensity ($W/m^2$), $S_4$ Q1,

$\sigma_{a,\min} = 0.0001m^{-1}$

Figure 5.16: Continued

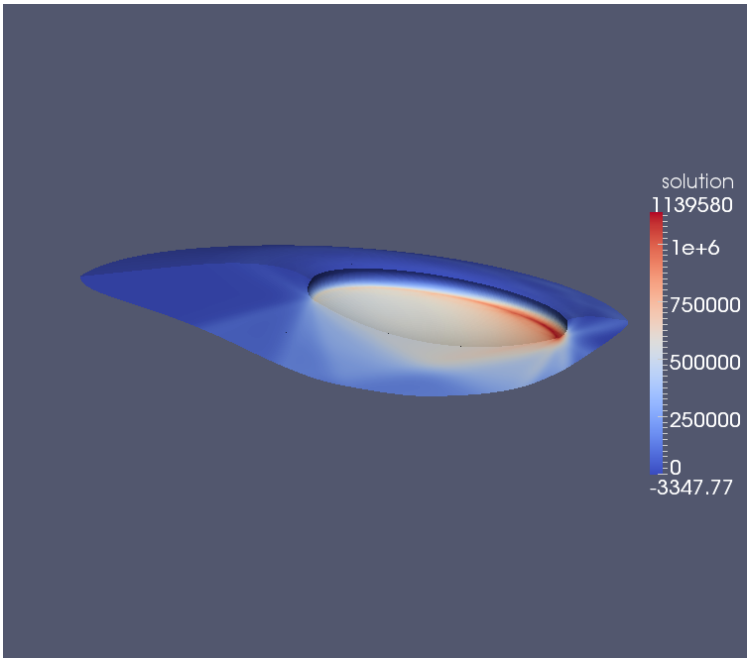


(d) Angle-integrated intensity ($W/m^2$), $S_4$ Q1, original $\sigma_a$

Figure 5.16: Continued

| | | | |
|---|---|---|---|
| $S_4$ Q1, | $\sigma_{a,\min} = 0.01m^{-1}$, | half-range flux: | $3.125 \times 10^5$ $W$ |
| $S_4$ Q1, | $\sigma_{a,\min} = 0.001m^{-1}$, | half-range flux: | $3.140 \times 10^5$ $W$ |
| $S_4$ Q1, | $\sigma_{a,\min} = 0.0001m^{-1}$, | half-range flux: | $3.141 \times 10^6$ $W$ |
| $S_4$ Q1, | $\sigma_{a,\min} = 0\ m^{-1}$, | half-range flux: | $3.141 \times 10^6$ $W$ |

Table 5.10: Least-squares $S_N$ $\sigma_{a,\min}$ convergence : half-range flux into the heat-shield

The results presented in Fig. 5.16 and Table 5.10 show excellent consistency across the a wide range of $\sigma_{a,\min}$ choice. There is almost no variation in either the half-range

flux or the spatial profile of the solution for $\phi$, as the $\sigma_{a,\min}$ varies from $0.01m^{-1}$ to $0m^{-1}$. This is the physical convergence behavior we expect out of the $\sigma_{a,\min}$ method. It indicates that the Least-squares $S_N$ method does not suffer from the convergence issues that plague the Even-parity $S_N$ method. Also notice that all the half-range fluxes produced by this method are positive. We will further verify those quantities of interest in the next section by comparing them with preliminary locally 1-D $S_N$ calculations.

## 5.4 Energy Flow at Heat-shield and Results Verification

Finally, some sample energy flow results over the heat-shield surface computed with least-squares $S_4$ are given below. Table 5.11 and Table 5.12 show the results computed with Q1 and Q2 Finite Element, respectively. The data shows the half-range flux into the ablator converged to within 16% at Q1 and the net-leakage converged to wihtin 1%.

| | |
|---|---|
| Averaged half-range flux into ablator: | $3.141 \times 10^5\ W$ |
| Averaged half-range flux towards shock: | $5.758 \times 10^6\ W$ |
| Averaged net-leakage (towards shock): | $5.444 \times 10^6\ W$ |
| Peak net-leakage : | $4.551 \times 10^5\ W/m^2$ |

Table 5.11: Energy flow through the heat-shield surface (Least-squares $S_4$ Q1 calculation)

| | |
|---|---|
| Averaged half-range flux into ablator: | $2.702 \times 10^5\ W$ |
| Averaged half-range flux towards shock: | $5.759 \times 10^6\ W$ |
| Averaged net-leakage (towards shock): | $5.488 \times 10^6\ W$ |
| Peak net-leakage : | $4.644 \times 10^5\ W/m^2$ |

Table 5.12: Energy flow through the heat-shield surface (Least-squares $S_4$ Q2 calculation)

To verify the 3-D Least-squares $S_N$ calculation, we compared our results with the preliminary locally 1-D $S_N$ calculation done by our partner at UT. The geometry is still a full 3-D model, but the $S_N$ calculations are only done in 1-D along normal directions indicated in Fig. 5.17 and no transverse leakage is accounted for.

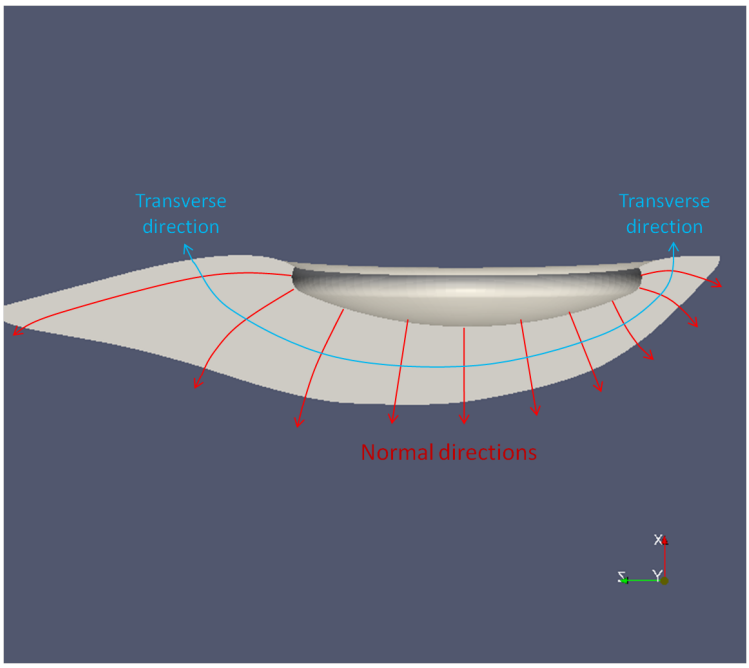


Figure 5.17: Normal and transverse directions

Their 1-D solution for net-leakage into the ablator is shown in Fig. 5.18. Note that all the numbers on the scale are negative, hence the pseudo color scale is inverted (blue meaning maximum absolute value, red meaning minimum absolute value). The negative solution indicates that the net-leakage is not into the ablator, rather, it is towards the shock, which is in alignment with our computation results. Comparing the peak value (peak leakage towards the shock), our result is about 33% lower than the 1-D calculation. We speculate that the difference is mainly due to the fact that in 3-D calculation the transverse leakage is accounted for, thus the peak value is lower.

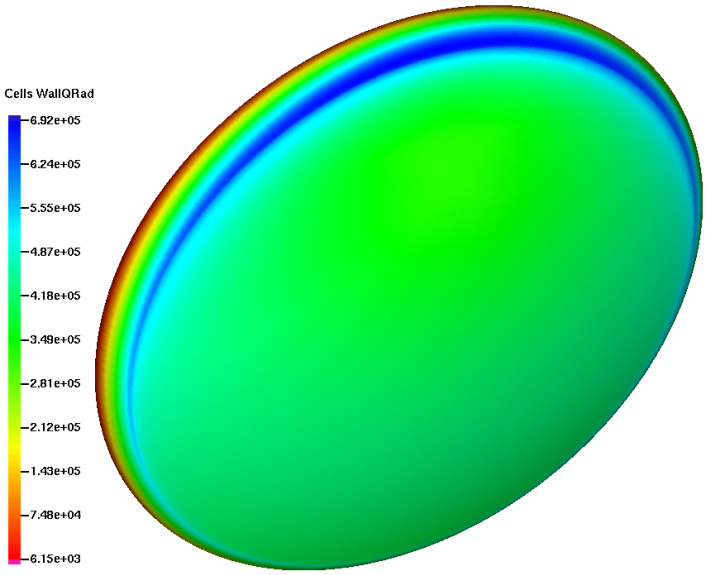


Figure 5.18: 1-D $S_N$ calculation along normal directions [Andre Maurente]

Also, in order to obtain an approximate solution by an analytic method, we carried out a mock up test problem, where the curved air region is approximated by a regular-shaped cylinder with the radius (R) being the radius of the heatshield and

depth (D) being the distance between the heatshield and back of the air region along the center line. The front face is set to mimic the back of the cold rarefied air region and the back face is set to mimic the hot heatshield surface. A radially invariant and axially varying temperature and cross section profiles are assumed and the axial dependencies of these two profiles are taken from the data along the center line of the original PECOS heatshield. The temperature profile and cross section profile are plotted in Fig. 5.19 and Fig. 5.20 respectively, and the mock up problem geometry is shown in Fig. 5.21.

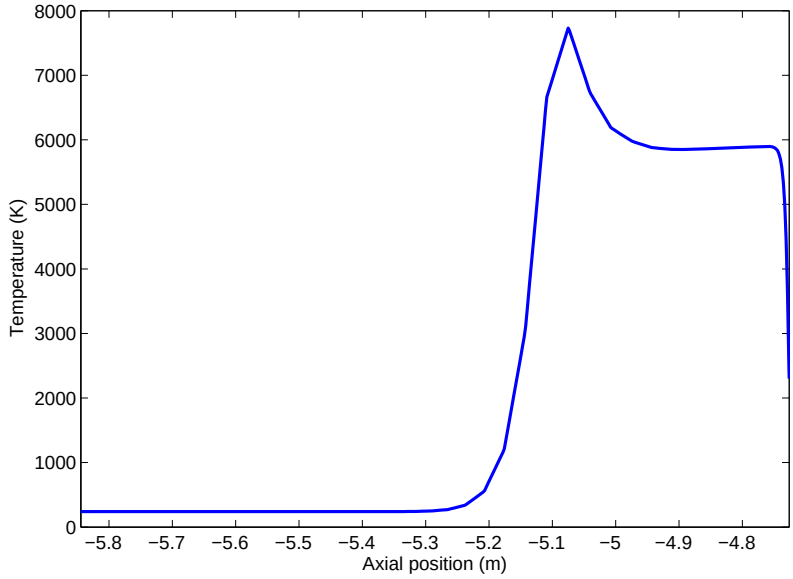


Figure 5.19: Centerline temperature profile

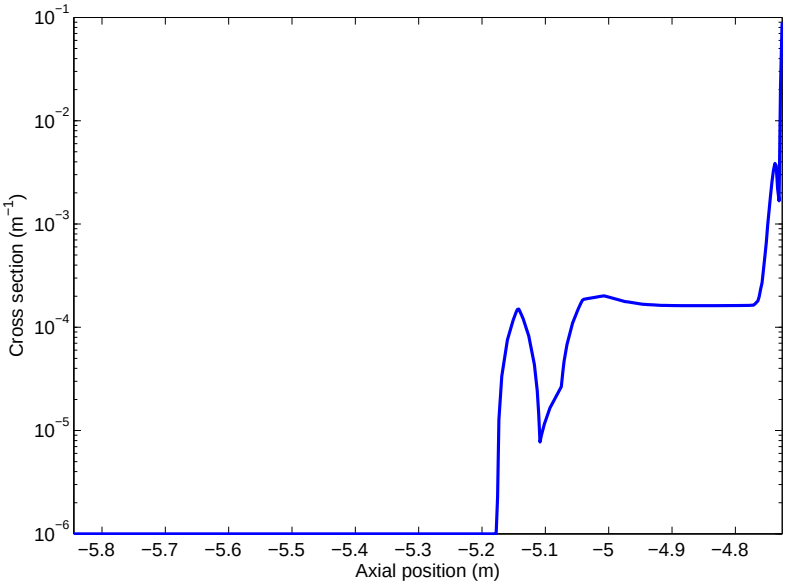


Figure 5.20: Centerline cross section profile

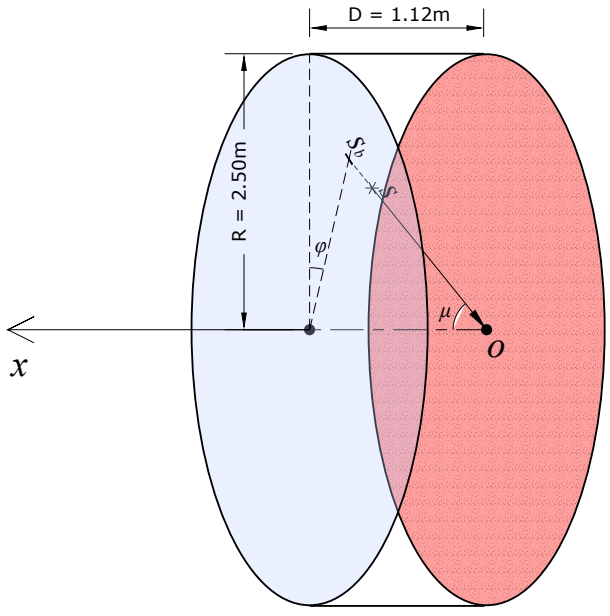


Figure 5.21: Cylinder mock-up problem

The photon energy flux into the heatshield at the center (denoted by $o$) can be computed analytically using the integral form of the transport equation given in Eq. (5.1):

$$QoI = \int_{2\pi}\int_0^1\int_0^{s_b} \mu \frac{\sigma_a(s) a c_0 T^4(s)}{4\pi} \exp\left[-\int_0^s \sigma_a(s')ds'\right] ds d\mu d\varphi, \qquad (5.1)$$

where $s$ is the distance between the source position and the point of interest ($o$) and $s_b$ is the maximum distance from $o$ along a certain direction within the problem domain. The $T$ and $\sigma_a$ are given as functions of $s$ in Eq. (5.1), but because the temperature and cross section profiles only vary along $x$, the $s$ dependence can be converted to $x$ dependence by projecting $s$ onto axial direction. The outgoing half-range flux at the center point is then compared with the half-range flux averaged over the heatshield surface computed by the Least-squares $S_N$ method. The difference is found to be 19%, which shows that the Least-squares $S_N$ method is in reasonable agreement with the analytic method.

| | |
|---|---|
| Averaged flux for PECOS computed by the Least-square $S_N$: | $1.197 \times 10^4\ W$ |
| Center-line flux for Mock-up computed by analytic transport: | $1.479 \times 10^4\ W$ |
| Relative difference : | 19.1% |

Table 5.13: Half-range fluxes averaged over the heat-shield surface

## 5.5 Summary on PECOS Results

In this section we compared the performance of the $SP_N$, Even-parity $S_N$, and Least-squares $S_N$ when applied to the vehicle re-entry problem. The results show that the Canonical $SP_N$ is extremely inaccurate, while Even-parity $S_N$ is better, it still has

severe convergence difficulties, in regard to the order of finite element polynomial and the value of $\sigma_{a,\min}$ used in the model. Both of these two methods yield negative half-range flux, which is not physical. The Least-squares $S_N$ method does not suffer from any of difficulties that plague the previous two methods and produces meaningful half-range flux. A comparison with an locally 1-D $S_N$ calculation indicates that the half-range flux produced by the Least-squares $S_N$ is in acceptable agreement with the 1-D result. An analytic calculation done on a cylinder mock up problem further verified the credibility of the Least-squares $S_N$ method. Lastly, the energy flow analyses over the heat-shield surface indicates that the thermal radiation is not a major contributor to the heating of the heat-shield and the heat-shield is actually loosing energy by radiation back more energy into the shock than what it receives from the shock. Thus the radiative heating does not seem to play an important role in determining the ablation rate of the heat-shield.

# 6. CONCLUSIONS

In the first part of this dissertation, two forms of the $S_N$ equations are reviewed. One is the conventional even-parity form, the other is a least-squares form that was recently proposed by Hansen and Morel and is designed to be compatible with void. Then, three mathematically equivalent forms of $SP_N$ equations, namely the Standard form, the Composite form, and the Canonical form, are reviewed. The iterative performance is analyzed for each form together with its appropriate iterative solution scheme and acceleration technique: Standard form with Gauss-Seidel iteration, Composite form with Gauss-Seidel and EXPLICIT iterations, Canonical form with Source iteration accelerated with $P_1$ Synthetic Acceleration ($P_1$SA) or Angular Multi-grid acceleration (AnMG) technique. Both Fourier analyses and 1-D numerical results show that the Canonical form solved using Source iteration with $P_1$SA acceleration is the most efficient method for most scenario. The Canonical form with AnMG should be preferred when the $SP_N$ order is high and the scattering is highly anisotropic. For low $SP_N$ orders, the composite form solved using the EXPLICIT method can be more advantageous for highly scattering and highly anisotropic problems.

In the second part of this dissertation, we tried to quantify the model error associated with the $SP_N$ method by comparing the Canonical $SP_N$ with the Even-parity $S_N$. The $S_N$ method converges to the true transport solution as $N$ increases, therefore it is used as the reference with very high $S_N$ order ($S_{64}$ are used for demonstration purpose). Three different model error analyses approaches are proposed and investigated, which include the *direct* method, the *residual* method, and the *adjoint* method. As a prerequisite for the *residual* and the *adjoint* methods, two reconstruction schemes for reconstructing $S_N$ angular intensity from $SP_N$ solution are

proposed, namely, a Legendre expansion scheme and a hybrid scheme. Both schemes are rigorous in the $P_0$ sense, with the Legendre expansion scheme being accurate up to $P_1$. However the hybrid scheme was chosen because it is more compatible with the $S_N$ method and simplifies the compensation for the extra error caused by the inaccurate reconstruction. Four kinds of quantities of interest ($QoI$) are considered and used as indicators of the model error, they are angle-integrated intensity, generic interior flux, cell-averaged interior flux, and boundary leakage. Numerical experiments carried out in a 2-D square geometry, spatially discretized with continuous Finite Element method, verified that all the three model error estimation methods are equivalent up to an easily computable error compensation. Out of the three methods, the *adjoint* method is recommended for real-world application because for various source conditions, only one (adjoint) $S_N$ calculation is needed to compute the model error associated with the $SP_N$ method. $SP_N$ calculation is still needed whenever the source condition changes, but it is much less expensive compared to the $S_N$ calculation.

Finally, the error estimation methods are applied to the PECOS vehicle re-entry problem and the error in the photon energy flux across the ablator surface is quantified. All the three methods still yield the same error, but the Even-parity $S_N$ solution itself is far off. Convergence tests show that both the canonical $SP_N$ is extremely inaccurate while the Even-parity $S_N$ has serious convergence difficulty, both due to the very small optical thickness of the problem. In contrast, the Least-squares $S_N$ behaves well in the void problem, and the net photon energy leakage computed with this method is in reasonable agreement with both the preliminary 1-D $S_N$ calculation result and a mock up analytic solution.

# REFERENCES


[1] Marvin L. Adams and Edward W. Larsen. Fast iterative methods for discrete-ordinates particle transport calculations. *Progress in Nuclear Energy*, 40(1):3–159, 2002.

[2] Wolfgang Bangerth, Ralf Hartmann, and Guido Kanschat. deal.II — a general purpose object oriented finite element library. *ACM Trans. Math. Softw.*, 33(4):1–24, 2007.

[3] Patrick S. Brantley and Edward W. Larsen. The simplified $P_3$ approximation. *Nuclear Science and Engineering*, 134:1–21, 2000.

[4] Ely M. Gelbard. Applications of spherical harmonics method to reactor problems. Technical Report WAPD-BT-20, Bettis Atomic Power Laboratory, 1960.

[5] Ely M. Gelbard. Simplified spherical harmonics equations and their use in shielding problems. Technical Report WAPD-T-1182, Bettis Atomic Power Laboratory, 1961.

[6] Ely M. Gelbard. Applications of simplified spherical harmonics equations in spherical geometry. Technical Report WAPD-TM-294, Bettis Atomic Power Laboratory, 1962.

[7] Ely M. Gelbard, J. Davis, and J. Pearson. Iterative solutions to the $P_l$ and double-$P_l$ equations. *Nuclear Science and Engineering*, 5:36–44, 1959.

[8] Jon B. Hansen and Jim E. Morel. A new least-squares transport equation compatible with voids. In *Proceedings of the International Conference on Mathematics and Computational Methods Applied to Nuclear Science & Engineering (M&C 2013)*, Sun Valley, Idaho, USA, 2013. American Nuclear Society.

[9] Alexander D. Klose and Edward W. Larsen. Light transport in biological tissue based on the simplified spherical harmonics equations. *Journal of Computational Physics*, 220(1):441–470, 2006.

[10] Edward W. Larsen, Jim E. Morel, and John M. McGhee. Asymptotic derivation of the multigroup $P_1$ and simplified $P_N$ equations with anisotropic scattering. *Nuclear Science and Engineering*, 123:328–342, 1996.

[11] K. D. Lathrop. Anisotropic scattering approximations in the mono-energetic boltzmann equation. *Nuclear Science and Engineering*, 21:498–508, 1963.

[12] Jean J. Lautard, D. Schneider, and Anne M. Baudron. Mixed-dual methods for neutronic reactor core calculations in the cronos system. In *International Conference Mathematics and Computation, Reactor Physics and Environmental Analysis of Nuclear Systems*, Madrid, Spain, 1999. American Nuclear Society.

[13] Jim E. Morel. A hybrid collocation-galerkin-$S_N$ method for solving the boltzmann transport equation. *Nuclear Science and Engineering*, 101:72–87, 1989.

[14] Jim E. Morel, B. Todd Adams, Taewan Noh, John M. McGhee, Thomas M. Evans, and Todd J. Urbatsh. Spatial discretizations for self-adjoint forms of the radiative transfer equations. *Journal of Computational Physics*, 214:12–40, 2006.

[15] Jim E. Morel and Thomas E. Manteuffel. An angular multigrid acceleration technique for $S_N$ equations with highly forward-peaked scattering. *Nuclear Science and Engineering*, 107:300–342, 1991.

[16] Jim E. Morel and John M. McGhee. A three-dimensional time-dependent tetrahedral-mesh $SP_N$ method. *Nuclear Science and Engineering*, 123:319–327, 1996.

[17] Gerald C. Pomraning. Asymptotic and variational derivations of the simplified $P_N$ equations. *Annals of Nuclear Energy*, 20:623–637, 1996.

[18] Chris Simmons. Introduction to project-based software engineering tools and guidelines employed by the pecos center. ICES (The Institute for Computational Engineering and Sciences) Forum, 2010.

[19] B. Turcksin, Jean C. Ragusa, and Jim E. Morel. Angular multigrid preconditioner for krylov-based solution techniques applied to the $S_N$ equations with highly forward-peaked scattering. *Transport Theory and Statistical Physics*, 41:1–22, 2012.

[20] Bruno Turcksin, Jean C. Ragusa, and Wolfgang Bangerth. Goal-oriented h-adaptivity for the multigroup $SP_N$ equations. *Nuclear Science and Engineering*, 165(3):305–319, 2010.

[21] Wallace F Walters. Use of the chebyshev-legendre quadrature set in discrete-ordinate codes. Technical report, Los Alamos National Lab., NM (USA), 1987.

# APPENDIX A

## REBALANCED LEAST-SQUARES $S_N$ METHOD

To verify the effectiveness of the renormalization scheme, we ran a series of 3-D finite element test problems. The geometry is $[-1,1]^3$ cube. Spatially varying cross-section is defined to be:

$$\sigma(x,y,z) = cos\left(\frac{\pi}{2}x\right) cos\left(\frac{\pi}{2}y\right) cos\left(\frac{\pi}{2}z\right), \tag{A.1}$$

and with modified cross-section being:

$$\sigma^* = 0.001\sigma. \tag{A.2}$$

The source is determined by the manufactured solution method to force an isotropic angular intensity of

$$\psi(x,y,z,\Omega) = 1.0 + \frac{1}{4\pi} cos\left(\frac{\pi}{2}x\right) cos\left(\frac{\pi}{2}y\right) cos\left(\frac{\pi}{2}z\right). \tag{A.3}$$

Notice that a homogeneous solution of 1.0 is added to the heterogeneous solution, in order to bound the volume integrated total source away from zero, which would lead to an arbitrarily large renormalization factor. The justification for such a shifted source is that, in reality, it will not be interesting to compute a trivial problem with zero source. we compared the energy balance before and after the renormalization, the results are tabulated in Table A.1

| number of cells | 5 | 10 | 20 | 40 |
|---|---|---|---|---|
| original $\sigma$ | $3.405e^{-3}$ | $7.902e^{-4}$ | $1.949e^{-4}$ | $6.925e^{-4}$ |
| original $\sigma$ renormalized | $6.67e^{-15}$ | $2.64e^{-14}$ | $5.69e^{-14}$ | $5.19e^{-14}$ |
| $\sigma^* = 0.0001\sigma$ | $6.580e^{-3}$ | $1.574e^{-3}$ | $3.897e^{-4}$ | $9.734e^{-5}$ |
| $\sigma^* = 0.0001\sigma$ renormalized | $1.17e^{-14}$ | $1.07e^{-14}$ | $2.79e^{-14}$ | $2.71e^{-13}$ |

Table A.1: Balance before and after renormalization

To see whether or not the error in the solution is reduced after the renormalization, we show the $L_2$-norms of the error in solution for various cross-section settings and various mesh size in Table A.2, and plot them in Fig. A.1.

| number of cells | 5 | 10 | 20 | 40 |
|---|---|---|---|---|
| Least-squares $S_N$ | $4.402e^{-2}$ | $1.096e^{-2}$ | $2.758e^{-3}$ | $6.925e^{-4}$ |
| Least-squares $S_N$ renormalized | $3.576e^{-2}$ | $9.167e^{-3}$ | $2.333e^{-3}$ | $5.887e^{-4}$ |
| Least-squares $S_N$ ($\sigma^*$) | $6.498e^{-2}$ | $1.743e^{-2}$ | $4.481e^{-3}$ | $1.131e^{-3}$ |
| Least-squares $S_N$ ($\sigma^*$) renormalized | $4.519e^{-2}$ | $1.300e^{-2}$ | $3.438e^{-3}$ | $8.778e^{-4}$ |

Table A.2: $L_2$-norm of the error in solution

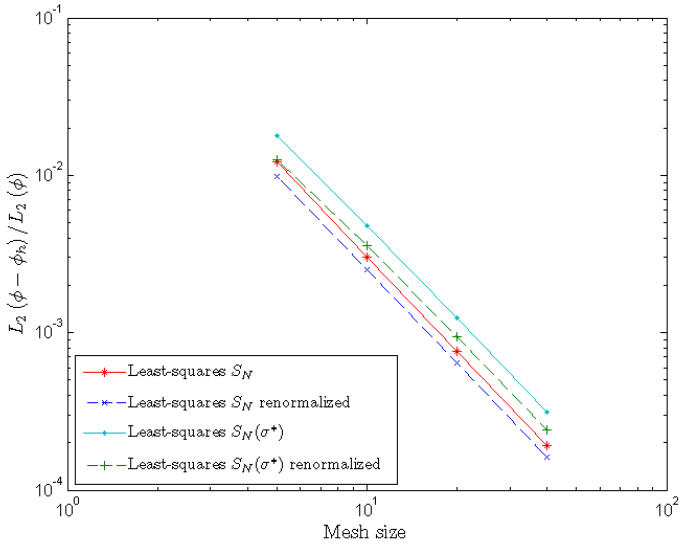


Figure A.1: $L_2$-norm of the error in solution

It can be seen from Fig. A.1 that the $L_2$-error does decreases after the renormalization for both cross-section settings. And it is easy to verify that the problems exhibit second order $h$-convergence on the $L_2$-error, which is the correct convergence rate for this second order method.

# APPENDIX B

# FOURIER ANALYSES

The iterative schemes can be written as:

$$\mathcal{A}\mathcal{U}^{(\ell+1)} = \mathcal{B}\mathcal{U}^{(\ell)} + \mathcal{Q}. \tag{B.1}$$

Here, $\mathcal{U}^{(\ell+1)}$ represents the unknown at iteration $\ell+1$, be it either the even intensity moments of the standard form, the composite intensities of the composite form, or the angular intensities of the canonical form. $\mathcal{Q}$ is the fixed external source. The true solution $\mathcal{U}$ satisfies

$$\mathcal{A}\mathcal{U} = \mathcal{B}\mathcal{U} + \mathcal{Q}. \tag{B.2}$$

Therefore, the error equation, obtained by subtracting the two previous expressions, is

$$\mathcal{A}\mathcal{E}^{(\ell+1)} = \mathcal{B}\mathcal{E}^{(\ell)}. \tag{B.3}$$

The error is expanded as a Fourier integral

$$\mathcal{E}^{(\ell+1)} = \int_{-\infty}^{\infty} d\lambda_x \int_{-\infty}^{\infty} d\lambda_y \int_{-\infty}^{\infty} d\lambda_z \mathcal{E}_{\vec{\Lambda}}^{(\ell+1)} \exp(i\vec{\Lambda}\cdot\vec{r}), \tag{B.4}$$

where $\vec{\Lambda} = [\lambda_x, \lambda_y, \lambda_z]^T$. One can take this expression and insert it in the error equation, but because of the linear independence of the Fourier modes $\exp(i\vec{\Lambda}\cdot\vec{r})$, one can analyze the error for a single generic mode. The resulting error equation, which was previously given in Eq. (3.75), is

$$\mathcal{A}(\vec{\Lambda})\mathcal{E}_{\vec{\Lambda}}^{(\ell+1)} = \mathcal{B}(\vec{\Lambda})\mathcal{E}_{\vec{\Lambda}}^{(\ell)}. \tag{B.5}$$

where the definitions of the iteration matrices for the various $SP_N$ forms analyzed here were given previously in Table 3.1. The properties of an iterative scheme can be determined by studying the eigenvalues of $\mathcal{A}(\vec{\Lambda})^{-1}\mathcal{B}(\vec{\Lambda})$. If the spectral radius (i.e., largest eigenvalue in magnitude) of $\mathcal{A}(\vec{\Lambda})^{-1}\mathcal{B}(\vec{\Lambda})$ is strictly less than unity (for any value of $\vec{\Lambda} = [\lambda_x, \lambda_y, \lambda_z]^T$), the iteration scheme will converge (the closer to zero the spectral radius, the faster the convergence).

The standard and composite forms contain explicitly Laplacian operators. Therefore, the term $-\vec{\nabla}\cdot\vec{\nabla}\mathcal{E}^{(\ell+1)}$ present in the error equation becomes

$$(\lambda_x^2 + \lambda_y^2 + \lambda_z^2)\mathcal{E}_{\vec{\Lambda}}^{(\ell+1)} = \|\vec{\Lambda}\|^2\mathcal{E}_{\vec{\Lambda}}^{(\ell+1)}. \tag{B.6}$$

Letting $\lambda = \|\vec{\Lambda}\|$, we note that it suffices to analyze the spectral radius of $\mathcal{A}(\vec{\Lambda})^{-1}\mathcal{B}(\vec{\Lambda})$ for $0 \leq \lambda < \infty$. That is to say that the convergence properties of the standard and composite forms of the $SP_N$ equations will hold, regardless of the spatial dimension (1, 2, or 3). To demonstrate that the same is true for the canonical form, some additional algebra, given next, is required.

Recall that the Source Iteration (SI) process for the canonical was given in Eq. (3.61). The associated error equation is

$$\begin{bmatrix} \lambda^2 K^{can} + \sigma_t & 0 \\ i\vec{\Lambda}\frac{W}{\sigma_t} & I \end{bmatrix} \begin{bmatrix} \mathcal{E}_{\vec{\Lambda}}^{+} \\ \mathcal{E}_{\vec{\Lambda}}^{-} \end{bmatrix}^{(\ell+1)} = \begin{bmatrix} H^{+} & -i\vec{\Lambda}W\frac{H^{-}}{\sigma_t} \\ 0 & \frac{H^{-}}{\sigma_t} \end{bmatrix} \begin{bmatrix} \mathcal{E}_{\vec{\Lambda}}^{+} \\ \mathcal{E}_{\vec{\Lambda}}^{-} \end{bmatrix}^{(\ell)}. \tag{B.7}$$

First, we apply the inverse of the matrix appearing on the left-hand-side and obtain

$$\begin{bmatrix} \mathcal{E}_{\vec{\Lambda}}^{+} \\ \mathcal{E}_{\vec{\Lambda}}^{-} \end{bmatrix}^{(\ell+1)} = \begin{bmatrix} (\lambda^2 K^{can} + \sigma_t)^{-1}H^{+} & -i\vec{\Lambda}\frac{W}{\sigma_t}(\lambda^2 K^{can} + \sigma_t)^{-1}H^{-} \\ -i\vec{\Lambda}\frac{W}{\sigma_t}(\lambda^2 K^{can} + \sigma_t)^{-1}H^{+} & (\lambda^2 K^{can} + \sigma_t)^{-1}H^{-} \end{bmatrix} \begin{bmatrix} \mathcal{E}_{\vec{\Lambda}}^{+} \\ \mathcal{E}_{\vec{\Lambda}}^{-} \end{bmatrix}^{(\ell)}. \tag{B.8}$$

From here, it is obvious to note that the characteristic polynomial associated with the matrix appearing in Eq. (B.8) will only depend upon $\lambda^2 = \|\vec{\Lambda}\|^2$ and, therefore, it will suffice to analyze the eigenvalues of the iteration matrix for $0 \leq \lambda < \infty$ to draw conclusions on the iterative performance of the scheme for any spatial dimension.

# APPENDIX C

## CONVERGENCE TESTS

To verify that the Canonical $SP_N$, Even-parity $S_N$, and Least-squares $S_N$ methods were implemented correctly, convergence tests are carried out for all the three codes. The test problem is a $[-1,1]^3$ cube with spatially varying cross-section defined to be:

$$\sigma(x,y,z) = \left[2 + sin\left(\frac{\pi}{2}x\right)\right]\left[2 + sin\left(\frac{\pi}{2}y\right)\right]\left[2 + sin\left(\frac{\pi}{2}z\right)\right]. \tag{C.1}$$

The source is determined by the manufactured solution method to force an isotropic angular intensity of

$$\psi(x,y,z,\Omega) = \frac{1}{4\pi} cos\left(\frac{\pi}{2}x\right) cos\left(\frac{\pi}{2}y\right) cos\left(\frac{\pi}{2}z\right). \tag{C.2}$$

A sample angle-integrated intensity solution for the Even-parity $S_N$ method with a $10 \times 10$ mesh is given in Fig. C.1. Notice that in order to verify the codes' behavior on general non-orthogonal meshes, we distorted the mesh by perturbing the inner grid points by 10% randomly around its otherwise orthogonal position.

For such a smooth solution the $L_2$-norm of the error in the numerical solution should exhibit a second order convergence as we refine the mesh. The results are given the Table C.1

Notice that for both Even-parity $S_N$ and Least-squares $S_N$, we ran a second test with a modified opacity $\sigma^*$ that is $1/1000^{th}$ of the original $\sigma$, in order to see how the optical thickness affects the convergence of those two particular methods. For convenience, the convergence rate plots for various methods are shown in Fig. C.2

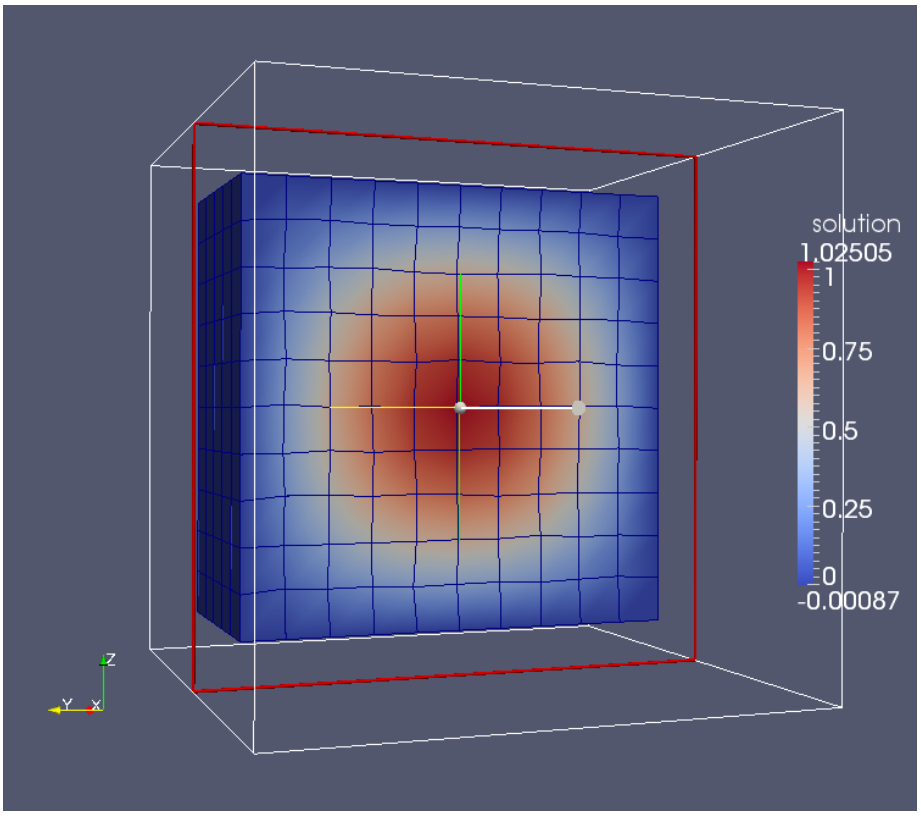


Figure C.1: Angle-integrated Intensity by the Even-parity $S_N$ on A $10 \times 10$ Perturbed Mesh

| number of cells | 5 | 10 | 20 | 40 | 80 |
|---|---|---|---|---|---|
| Canonical $SP_N$ | $1.595e^{-2}$ | $3.956e^{-3}$ | $9.855e^{-4}$ | $2.461e^{-4}$ | $6.150e^{-5}$ |
| Even-parity $S_N$ | $6.701e^{-3}$ | $1.124e^{-3}$ | $2.283e^{-4}$ | $5.317e^{-5}$ | $1.303e^{-5}$ |
| Even-parity $S_N$ ($\sigma^* = 0.001\sigma$) | $6.242e^{-1}$ | $3.824e^{-1}$ | $1.642e^{-1}$ | $5.530e^{-2}$ | $1.619e^{-2}$ |
| Least-squares $S_N$ | $2.651e^{-2}$ | $6.459e^{-3}$ | $1.604e^{-3}$ | $4.002e^{-4}$ | - |
| Least-squares $S_N$ ($\sigma^* = 0.001\sigma$) | $6.465e^{-2}$ | $1.732e^{-2}$ | $4.453e^{-3}$ | $1.124e^{-3}$ | - |

Table C.1: Convergence rate tests results for $L_2$-norm of error

The results shows in most of the cases, the convergence rate is exact $2^{nd}$ order starting from the very coarse grid, with the exception that, for the Even-parity $S_N$

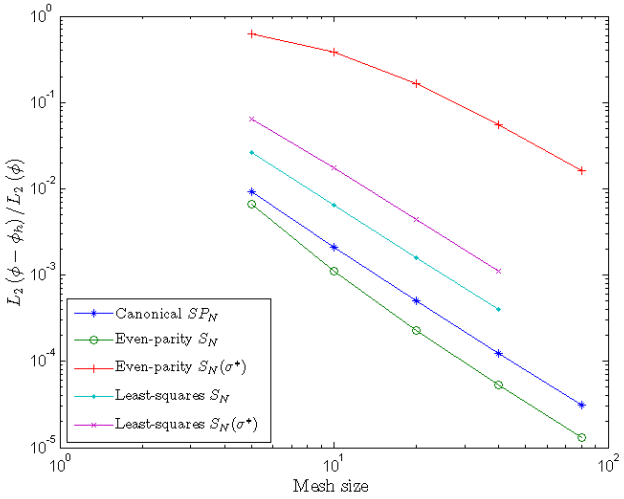


Figure C.2: Convergence rates of various transport models

with normal $\sigma$, the convergence rate approaches $2^{nd}$ order from above, while for the Even-parity $S_N$ with small $\sigma^*$, the convergence rate approaches $2^{nd}$ order from below, and the $L_2$-error is orders of magnitude higher than the former. These results further confirmed that the Even-parity $S_N$ method has convergence difficulty in near-void problems, while the Least-squares $S_N$ method does not suffer from the same defect.